Transpiration Electrokinetic Power Generation and Zinc Ion Battery for Autonomous Leak Detection

Dylan Damen Edmundson

A dissertation

Submitted in partial fulfillment of the

requirements for the degree of

Doctor of Philosophy

University of Washington

2024

Reading Committee:

Anthony Dichiara, Chair

Renata Bura

Rick Gustafson

Program Authorized to Offer Degree:

School of Environmental and Forest Sciences

University of Washington

Abstract

Transpiration Electrokinetic Power Generation and Zinc Ion Battery for Autonomous Leak Detection

Dylan Damen Edmundson

Chair of the Supervisory Committee:

Anthony Dichiara

School of Environmental and Forst Sciences

Every year $6 billion worth of water is lost in residential homes caused by undetected leaks creating nearly $20 billion in property damage annually in the U.S alone. These leaks also raise environmental concerns due to energy consumption in water treatment plants and declining freshwater sources. Additionally, water leaks can create extremely dangerous situations, having been the cause of data center fires, by undetected leaks traveling into battery rooms creating short circuits and extremely dangerous lithium battery fires. Because of these concerns researchers have developed many types of leak detection systems that have become commercially available for years by employing acoustic detection principles. While these detectors have shown success

deployed in oil pipelines, they often suffer from low signal to noise ratios and poor sensitivity in water pipelines.

Recently conductive carbon nanotube paper developed by Goodman et al. was applied as a leak detector with the ability to sense leaks as small as 45 μL by monitoring changes in the resistance of the paper as it gets wet. While this system is highly sensitive and uses low power it requires constant or intermittent monitoring and continuous power consumption needing a power line connection or battery that will often require replacement. While this application is great for industrial applications where wired connection and continuous power consumption are not a problem, it is not ideal for situations involving hidden pipelines where regular access is not possible, and the device needs to last for a very long time. To solve this problem the concept of a fully autonomous leak detection system was envisioned and the research presented here aims to develop leak activated power devices to operate wireless sensing applications.

In this study two mechanisms of leak triggered power generation were developed for leak detection: an electrochemically enhanced transpiration driven electrokinetic power generator (TEPG) and a wick activated zinc air battery. Carbon nanotube paper was implemented as a TEPG using an active zinc anode to harness energy from moisture wicking and electrochemical processes, achieving a maximum theoretical power output of 1.4 mW. A single device could then be used to activate a latching circuit allowing a battery to operate an internet of things (IOT) device for WI-FI signaled leak detection. To reach higher power outputs a zinc air battery was developed using recyclable paper-based materials to create a fibrous zinc anode and a wicking battery separator. The zinc anode was developed by embedding zinc microspheres into a carbon nanotube/paper-based 3D structure that was also evaluated for the improvement of zinc ion batteries. A comparison of a typical zinc foil to the engineered anode showed an increase in battery capacity retention from

55% to 60% respectively. Lastly, a wick was developed to optimize the porosity of a bleached softwood paper to increase wicking speed, reaching a wick capable of transporting water 4 cm vertically in ~25 seconds. This wick was then combined with the developed zinc anode and smart paper to create a zinc air battery capable of wicking water to activate the battery in the event of a leak. By the developments presented in this dissertation two novel leak detection mechanisms were developed, capable of eliminating the need for continuous monitoring and thus external power sources, increasing the reliability and longevity of leak sensors.

Table of Content

List of Figures

List of Tables

List of Equations

Nomenclature

Table 1.1 List of Common abbreviations and acronyms

TEPG	Transpiration Driven Electrokinetic Power Generation
ZIB	Zinc Ion Battery
SEM	Scanning Electron Microscopy
XRD	X-ray Diffraction Spectroscopy
LA-MS	Laser Ablation Mass Spectroscopy
GCD	Galvanostatic Charge/Discharge
CV	Cyclic Voltammetry
EIS	Electrochemical Impedance Spectroscopy
BSE	Bioresource Science and Engineering
CAGR	Constant Annual Growth Rate
CCTV	Closed Circuit Television
CNT	Carbon Nanotube
MEG	Moist Electric Generator
EDL	Electric Double Layer
ZAB	Zinc Air Battery
ORR	Oxygen Reduction Reaction
OER	Oxygen Evolution Reaction
TAPPI	Technical Assossiation of the Pulp and Paper Industry
DI	Deionized
SCC	Short Circuit Current
OCV	Open Circuit Voltage
MTP	Maximum Theoretical Power
CNC	Computer Numerical Control
LSV	Linear Sweep Voltammetry
SW	Softwood
MWCNT-OH	Hydroxyl Functionalized Multiwalled Carbon Nanotube
UV-Vis	Ultraviolet-Visible Spectroscopy
EDS	Energy Dispersive X-ray Spectroscopy
PCB	Printed Circuit Board
DMM	Digital Multimeter
SMU	Source Measurement Unit
SPICE	Simulation Program with Integrated Circuit Emphasis
FWHM	Full Width at Half Maximum
LED	Light Emitting Diode
ANOVA	Analysis of Variance
IOT	Internet of Things
RF	Radio Frequency
BJT	Bipolar Junction Transistor
MOSFET	Metal Oxide Semiconductor Field Effect Transistor

Instrumentation

Table 1.2 List of instruments used in this study

Category	**Instrument**
Materials Synthesis	• Pilot scale paper machine • Pilot scale refiner • Handsheet making • Lab scale PFI refining • Sonic horn • Chemical vapor deposition • Vacuum oven • CNC Machining • 3D printing • Wet chemistry synthesis and characterization
Structural Characterization	• Leica ACE600 SEM sample coater • ThermoFisher apreo variable pressure SEM • Oxford Instruments EDS – dualbeam FIB-SEM • Bruker D8 discover with IμS 2-D XRD • FTIR • Dynamic Light Scattering • Electrophoretic Light Scattering • Optical Microscopy
Paper Testing	• Tensile testing • Burst testing • Tear testing • Gurly method • Smoothness testing • Optical testing • Z-direction tensile testing • Compression testing

Electrical and Electrochemical Characterization	• Keithley source measurement unit
	• Digital multimeter
	• Potentiostat
	  ○ Cyclic Voltammetry
	  ○ Electrochemical Impedance Spectroscopy
	  ○ Galvanostatic Charge/Discharge
	  ○ Chronoamperometry/voltammetry
	  ○ Linear Sweep Voltammetry
	• Rotating disk electrode
	  ○ Tafel analysis
	  ○ Butler-Volmer kinetics

Software/Firmware	• Fusion 360 • LTSpice • Aftermath • ImageJ • Keithley TSP scripting

	• Originlab • C++ • Java • Arduino • Inkscape • Cura

Associated Publications

Table 1.3 list of associated manuscripts and their state in publication

Title	**Journal/Intended Journal**	**Status**
Electrochemically Enhanced Transpiration Driven Electrokinetic Power Generator	Advanced Energy Materials	In preparation (anticipated publication February 2025)
Paper Based Zinc Anode for Zinc Ion Battery Advancement	Energy Storage Materials	In preparation (anticipated publication March 2025)
Energy-as-Data Device for Autonomous Leak Detection	ACS Sensors	In preparation (anticipated publication April 2025)

Research Dissemination

Table 1.4 List of conferences attended during graduate studies

Organization	**Title**	**Year**	**Type**
American Chemical Society	Sonochemical synthesis of lignin nanoparticles and their applications in poly(vinyl) alcohol composites	2022	Oral
International Conference on Flow Dynamics	Electrolyte Applications for the Enhancement of Transpiration Driven Electrokinetic Generators	2023	Oral
Materials Research Society	Sonochemical synthesis of lignin nanoparticles and their applications in poly(vinyl) alcohol composites	2024	Oral
Materials Research Society	Moisture activated zinc ion battery for leak detection signaling.	2024	Poster
GDR MultiPODE	A Fibrous Zinc Anode for Zinc Ion Batteries	2024	Oral

Acknowledgements

Thank you:

The University of Washington Molecular Analysis Facility for access, training, and advising for SEM and XRD characterizations. Jakub Sliwinski and the TraceLab at the University of Washington School of Oceanography for LA-MS characterizations. Xiaoxiao Jia and the Guozhong Cao Research Lab at the University of Washington Material Science and Engineering Department for GCD, CV, and EIS characterization training and analysis.

Dr. Shiela Goodman and Dr. Heather Niles for your mentorship during my undergraduate program and early years of graduate school. Undergraduate researchers Kira Stewart and Katelyn Schaures for your help with running zinc anode and wicking experiments. BSE Graduate students Anna Fall and Lexi Maerz, for your help with SEM during my trip abroad. My Friends in the BSE program for your friendships over the years. My committee members Professors Rick Gustafson, Renata Bura, Guozhong Cao, and Hidemasa Takana for your guidance with my research projects, and mentorship over the years. Special thanks to Professor Anthony Dichiara my Principal Investigator and committee chair for his mentorship and guidance. You were a great teacher during my undergraduate degree and have been a wonderful mentor on my journey through graduate school, offering me many extraordinary opportunities along the way.

My parents Dean, Cheryl, and Shana Edmundson and my in-laws Franscisco and Laura Ruiz-Velasco for all of your support and help over the years while I have been pursuing 10 years of education. Lastly, I'd like to thank my wife Laura Edmundson for all her support through the long days of experiments and weekends spent working towards a doctorate. Your love and support mean everything to me, and I am lucky to have you.

1 Introduction

1.1 The Cost of Water Leaks

Every renter and homeowner in the world have experienced the simple annoyance of a leaking faucet leading to incessant dripping noises and sleepless nights. It is often easy to ignore a small leak like this and think of it as a minuscule waste of water that will barely affect one's finances or day-to-day life. While this simple annoyance may seem trivial, the larger aspect of water leaks in residential and industrial water supplies can have expensive, dangerous, and environmental consequences.

The cost of a leak to the residential customer can be quantified by reported supplier losses as these costs will lead to increased prices for the consumer. For example every year an estimated one trillion gallons of water never reaches its intended consumer because of small household leaks in the US [1]. With an average cost of roughly 0.6 cents per gallon in 2019 [2] homeowners are losing nearly $6 billion a year in addition to an estimated $20 billion in repair costs to fix mold and water damage [3]. When factoring in the nation's population reported to be approximately 328 million by the US census bureau in 2019 [4] the average cost per US resident equates to approximately $80/year. While this cost may not seem to be much at first glance, by taking into account the average individual US consumer use of 69.3 gallons/day [5] $80/year equates to ~50% of a typical US consumers bill for indoor water use. Although the monetary cost of a water leak can be substantial there are many more important factors to consider, such as dangerous situations that leaks can cause.

One such danger, especially relevant to modern technology, is data center fires. Many data centers utilize water cooling systems which can lead to catastrophic failures with several events

occurring in French datacenters. In 2023 google experienced outages in Europe caused by a fire in Global Switch's data center located in Paris; the result of a water leak in their cooling system which leaked into their battery room [6]. Earlier in March of 2021 a similar fire at the OVHcloud's data center in Strasbourg France was suspected to have been caused by similar circumstances, resulting in the destruction of 30,000 servers [7]. As more companies continue moving to cloud based systems, remote/hybrid jobs, and web-based services data centers will continue to grow. For example by the end of 2024 the number of public data centers will reach 5709 worldwide (not including 5186 colocation sites and 523 hyperscale sites) and are expected to increase to 8,378 data centers by 2030 [8]. As the number of data centers continue to increase, so will the need for leak detection and deterrent systems to prevent dangerous fires as well as data loss. And while the dangers of leaks certainly add to the cost of a leak, there is still environmental consideration to account for.

With the ever-increasing threat of climate change, reducing water waste (among many things) is more important than ever before. Water loss caused by pipe leaks in the EU were reported to reach an average loss of 2696 m^3/km of piping equating to 25% of total potable water sent by water companies in 2021 [9]. To make matters worse one report made in 2008 projected 3.9 billion people (40% of the population) to be residing in areas with limited drinking water by the year 2050 [10], [11]. And while a more recent 2021 study has shown a slightly improved outlook, projections still expect between 1.7 and 2.4 billion people as well as 20 megacities in 2050 to be affected by potable water shortages [12]. These staggering statics show an even greater cost of a water leak to the near future and without intervention these statistics will likely hold true.

These reports and studies present both financial and moral incentives for the development of improved leak detection systems. While there is already a market for leak detectors, they are

often expensive and difficult to implement, leaving not only room for improvement but an expanding market. For example in a 2023 market analysis report the data center water leak detection market was estimated to be worth $181 million, with constant annual growth rate (CAGR) of 4.2% projected to reach $242 million by the year 2030 [13]. Additionally the global general water leak detector market was reported to be $4.6 billion in 2022 and expected to reach $7.2 billion by 2030 [14]. This growth coupled with many other factors leaves plenty of room for new leak detection inventions to enter the growing market as shown in figure 1.1.1. Currently the most commonly available leak detectors include acoustic, thermal, and optical leak detectors which have several pitfalls that will be discussed in the following section.

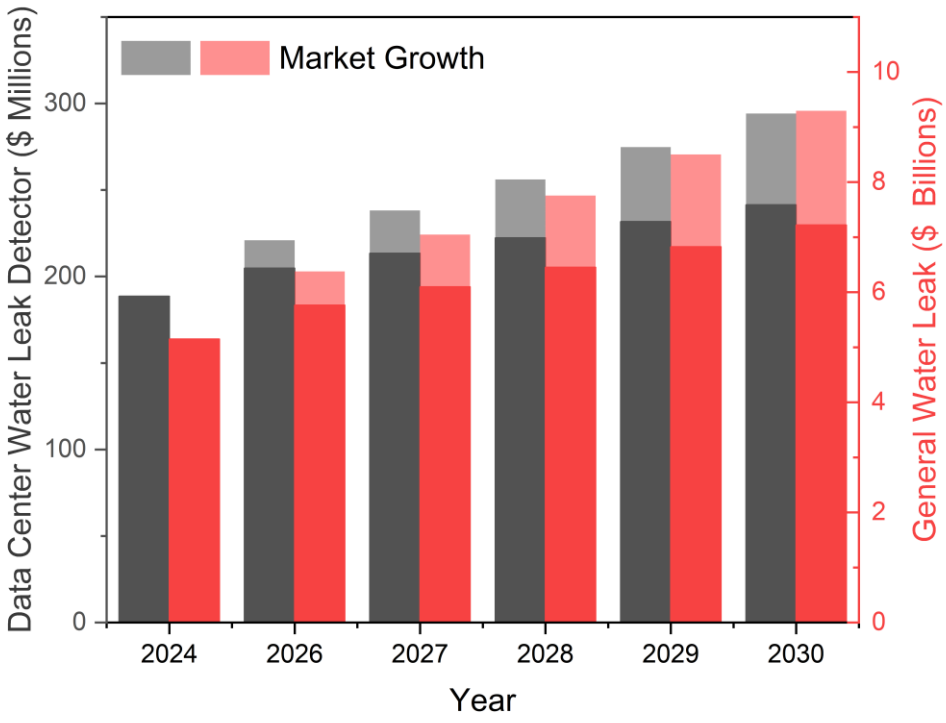

Figure 1.1.1 Leak detector project market growth from 2024 to 2030 [13], [14].

1.2 Current Commercial Solutions for Finding and Detecting Water Leaks

Leak sensors can generally be separated into two main categories, real time and non-real time leak detection [15]. Real time systems can acquire data continuously and monitor leaks as they occur, while non-real time systems do not continuously monitor and are employed either on a maintenance schedule or after a leak has become evident. Non-real time systems include closed circuit television (CCTV) and infrared imaging techniques which require a trained technician to operate and are usually used to find a leak after damage is noticed [16], [17], [18], [19]. CCTV systems are operated by a technician inserting a camera into a pipeline and finding a leak visually [16] and while this method is common and effective the requirement of an access point for insertion of the camera leads to long repair times and dangerous working condition. Thermal imaging on the other hand works by receiving infrared radiation identifying thermal gradients caused by conduction and convection which can be evidence of a leak [17], [18], [19]. This method has an advantage over CCTV camera monitoring since it does not require an access point, however inaccuracies due to other potential culprits for cold spots such as poor insulation can lead to false leak identification [17], [18], [19]. While these methods may be suitable for finding leaks after they occur, they do not help with the issue of fast sensing requirements for industrial scale operations which can quickly lose vast amounts of water in a matter of seconds.

Real-time monitoring devices are of much more interest since they can quickly identify a leak when it occurs and signal an alarm. The most common real-time leak detectors in industry are acoustic monitoring systems shown in figure 1.2.1. These devices monitor the acoustic pressure waves in a pipe usually transmitted to transducers mounted near or on a pipe [20], [21], [22], [23], [24], [25]. By converting observed acoustic waveforms to a frequency domain a spike in frequency

relative to the background acoustic waves can be detected when a leak occurs [21], [26]. While these systems have shown to be quite accurate and have good sensitivity they often suffer from signal attenuation in the pipes especially when pipes are buried or nonmetallic [15], [21], [26]. To mitigate this limitation Khulief et al. employed an in-pipe hydrophone monitoring pressure waves from the water source as opposed to vibrations transferred through the pipe [21]. Although this method reduced signal attenuation the hydrophone was only effective when it was placed downstream of the port of the leak. Although advancements in acoustic techniques continue to grow and improve sensing systems, scientists have begun to investigate alternative mechanisms for leak detectors. Many of these new mechanisms have been realized due to developments in materials research in the fields of nanomaterials, polymers, and biopolymers. In the following section several publications and their novel materials/sensing mechanisms are reviewed.

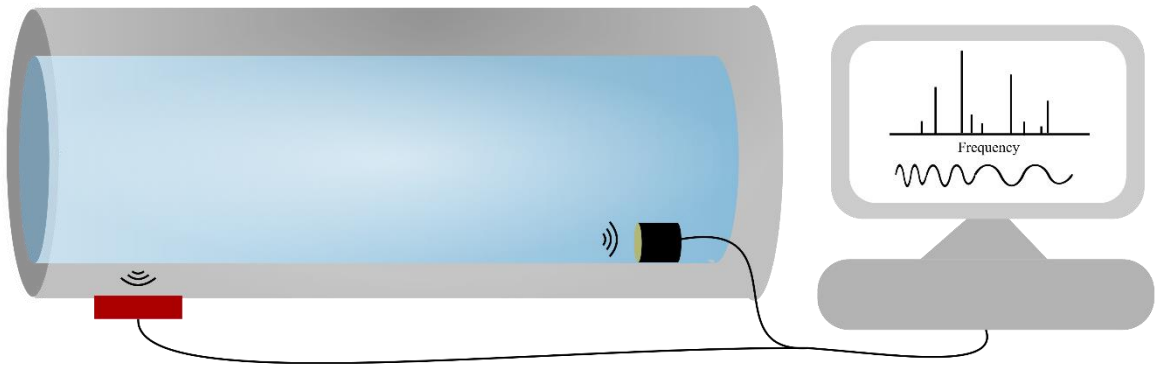

Figure 1.2.1 Acoustic Leak Detection Mechanism.

1.3 Novel Advancements in Leak Sensing Mechanisms

Several advancements have been made in recent years to improve upon liquid sensing and have even extended to sensing condensation and vapors. Some techniques in the literature include conductometric sensing [27], gate activation in field effect transistors [28], and many other

mechanisms [29], [30], [31]. A popular method of sensing that has gained a lot of interest involves resistive sensing technologies based on carbon/polymer composites where fiber swelling causes reduced conductivity by separation of conductive filler as shown in figure 1.3.1. Work conducted by Villmow et al. used a smart polymer/carbon nanotube (CNT) composite to sense liquids by monitoring resistance changes in presence of vapor [32]. In this study a conductive polymer network capable of swelling in the presence of organic vapors was used as the matrix material with a CNT filler. As the matrix material absorbed vapor, swelling occurred and the resistance of the material changed. Similarly Bouvree et al developed a chitosan-carbon nanoparticle resistive sensor capable of detecting polar vapors [33]. Goodman et al took this concept to another level reaching highly sensitive and scalable results through the manufacturing of a paper based sensor for applications in leak detection [34], [35], [36], [37], [38]. In this study Goodman employed bleached softwood pulp as the polymer matrix and OH functionalized multiwalled CNT (MWCNT-OH) as the filler. With a sensitivity of 12,000% [35], compared to 120% reported by Bouvree et al [33], and 800% for expensive cutting edge fiber optic detection systems [15], smart paper has incredible capability for leak detection, being able to detect leaks as small as 0.25 μL. Due to its scalability it has also been tested with favorable results as a sensor for detecting leaks in server cooling systems at the CERN particle accelerator.

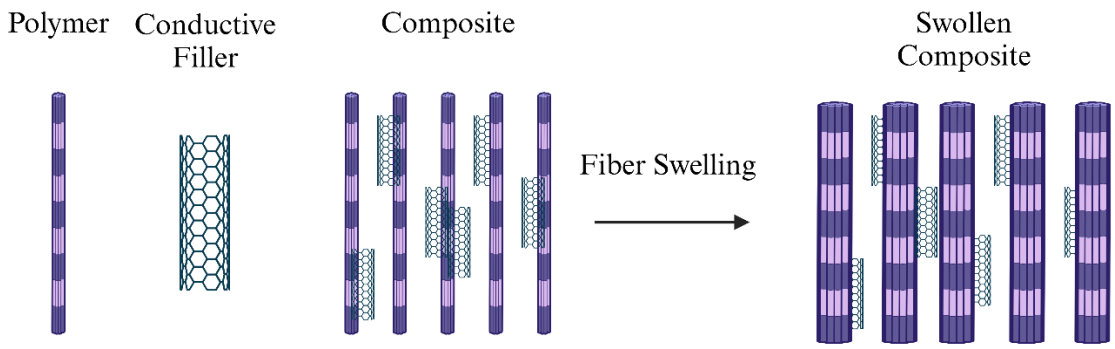

Figure 1.3.1 Resistive swelling mechanism. Illustration made with Biorender.com

The success of smart paper has led to interest from companies, such as A.O. smith, known for their water heating systems used for residential properties. These water heaters have an average lifespan between 8 and 20 years [39] after which the bottom pan rusts through and water spills out onto the floor. This of course can lead to costly water damage repairs and detection could remove this problem, however continuous resistance monitoring may not be suitable due to power requirements. In this dissertation a solution to this problem is pursued through the development of autonomous leak detecting systems where the presence of moisture activates a power source triggering a response system.

1.4 Self-Powered Leak Detection

In the pursuit of self-powered leak detection novel leak sensing mechanisms had to be investigated, moving away from the common resistive sensing technique. Here two sensing mechanisms were developed utilizing advancements in moist electric generation (MEG) and aqueous zinc-based batteries.

1.4.1 Moist Electric Generation (MEG)

Moist electric power generation is a new branch of research that focuses on developing materials to harvest energy from water transport through a conductive material. While the mode of energy generation is still not entirely understood several mechanisms have been proposed with the most commonly referenced being streaming current, pseudo-streaming current, and ion gradient diffusion (mechanism visual aids are shown in figure 1.4.1) [40], [41], [42], [43], [44], [45], [46], [47], [48], [49], [50], [51], [52], [53].

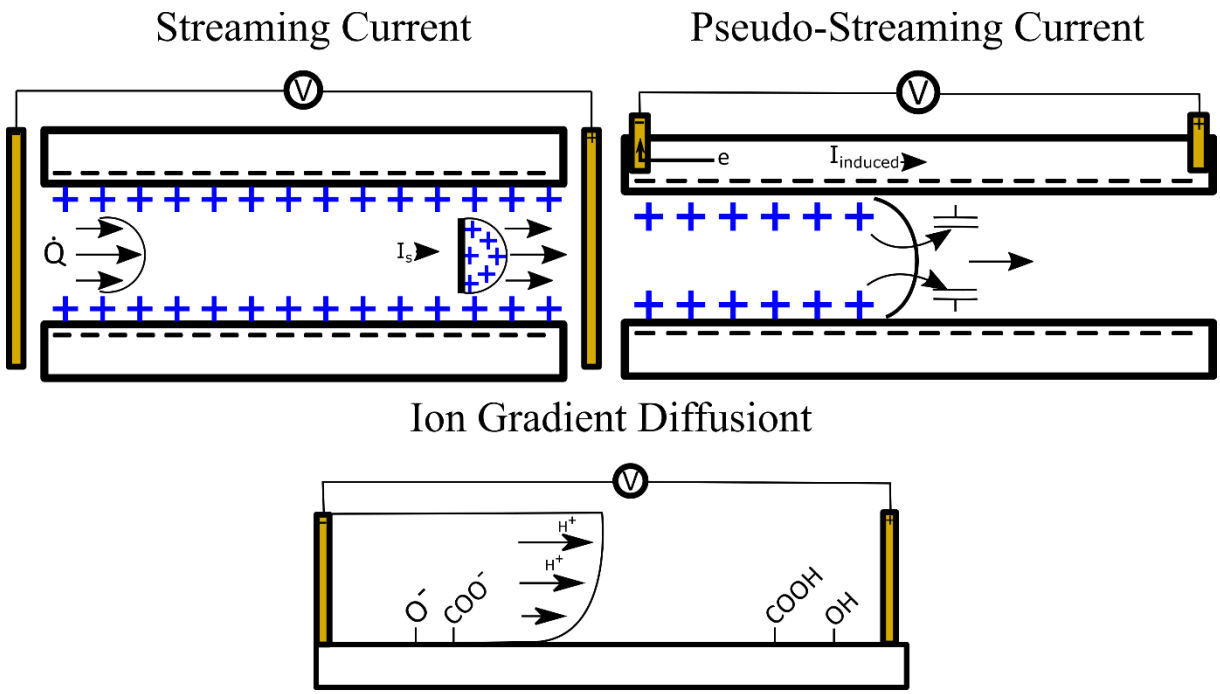

Figure 1.4.1 Commonly proposed mechanisms of moist electric generation.

In a porous conductive material with micro/nano capillaries water ionizes and forms an electric double layer (EDL) at the solid liquid interface. When capillaries have a sufficiently small diameter ranging on the same order of magnitude as the Debye length of the solution the EDL formed in the capillary will overlap resulting in a channel filled with counter ions [44]. As pressure gradients in the fluid cause water transport through the capillaries, shear forces in the fluid create

a net ionic flux in the diffusive layer resulting in charge separation and a streaming current [48], [49], [50]. The power in this system can be harnessed by appropriate electrodes collecting energy from non-faradaic currents resulting in power generation. These effects have been shown to be increased by using nanochannels which increase EDL overlap and thus counterion concentration [44], but this is countered by an increase in fluid friction reducing fluid speed and leading to a maximum theoretic electrokinetic power conversion of 12% in silica based materials [54]. To further improve upon this issue newer developments in CNTs have given rise to better performance due to low water friction interfaces caused by hydrophobic interactions reaching a new theoretical maximum of 30% [55], [56]. Even with material improvements and better performance, streaming current based systems run into issues of continuous operation. Although the power harvesting of these devices are incredibly small they require a constant pressure gradient to be applied, otherwise once a stable charge separation is achieved ions in the diffuse layer begin to repel and stop current flow [44]. To prevent this problem researchers have looked to devices operated based on moisture gradients harnessing energy from humid air, however power outputs are very low ranging from nano to microwatts of power. [57], [58]. To overcome these issues more recent studies have begun to investigate asymmetric wetting to cause pseudo-streaming currents and ion gradient diffusion mechanisms leading to higher energy outputs.

In the Pseudo-streaming current mechanism similar principles to streaming current are reported with the key distinguishing factor being the presence of a wet/dry interface. This interface leads to the continuous transport of water and protons caused by transpiration forces creating a continuous flux of charge inducing current flow in the conductive material [43], [45], [46], [47]. These pseudo-streaming current devices are often referred to as transpiration driven electrokinetic power generators (TEPG) and consist of a material made of cellulosic polymer matrices and embedded

conductive carbon fillers [43], [46], [47], [59]. The last mechanism commonly discussed utilizes the advantages of ion gradients created by ionization of functional groups present in many polymers. This mechanism is proposed to operate by the deprotonation of polar functional groups such as hydroxyl and carboxyl groups donating protons and creating a higher negative charge to the surface allowing the combined increase of power output via improvements to streaming current and charge gradient [40], [45]. In practice these devices are often wetted by dropping water onto one side of the device and allowing wicking/transpiration forces to drive the power generation, often only requiring 100 – 200 μL of polar liquid to operate. With low fluid volumes and improved power generation these devices are good candidates for leak detection.

1.4.2 Zinc-based batteries

Batteries at their most basic function consist of a cathode, anode, and electrolyte that, in modern batteries, is typically housed in a battery separator [60]. While research in batteries has heavily focused on lithium ion batteries, new research has begun a shift to safer and more environmentally friendly aqueous zinc based batteries [61], [62], [63], [64], [65], [66], [67], [68], [69], [70], [71], [72].

One common type of aqueous zinc based battery is the zinc ion battery (ZIB) which is a type of mobile ion battery consisting of a zinc anode and metal oxide cathode [73], [74]. Mobile ion batteries are a type of secondary battery where an ion (in this case Zn^{2+}) is reversibly oxidized and reduced at both the anode and cathode allowing the battery to be both discharged and recharged. The most common and best performing cathodes include VOH and MnO_2 based cathodes which are chosen for their highly porous structures and ability to form zinc metal oxide complexes through reversible reactions [62], [70], [73]. These batteries often employ electrolytes

such as ZnCl, $ZnSO_4$, and trifluoromethanesulfonate $Zn(CF_3SO_3)_2$ which have been developed to improve performance by decreasing zinc/water coordination [62], [75], [76].

Zinc air batteries (ZAB) are another common type of battery that operate based on the oxygen reduction reaction (ORR) at the cathode and oxidation of zinc at the anode allowing lightweight/high capacity batteries [71]. More recently these batteries have been developed to form a rechargeable zinc air battery through the development of bifunctional catalysts allowing both ORR's and oxygen evolution reactions (OER) creating a reversible system [72], [77], [78], [79], [80]. Many studies have been performed investigating ZIB's and ZAB's intending to improve on the battery performance and cycling stability by engineering improved cathodes, separators, and electrodes [61], [62], [63], [64], [65], [66], [67], [68], [69], [70], [81], [82], [83].

Since these batteries work in aqueous electrolytes, they are perfect candidates to investigate for electrochemical leak detection. A schematic showing the theorized sensing mechanism is displayed in figure 1.4.2 where a wick is used as a battery separator. When no water is present the battery is off since no electrolyte is available to allow conduction of active redox ions to and from each electrode, however when a leak happens water can wick up the separator and complete the battery allowing for high powered electrochemical detection.

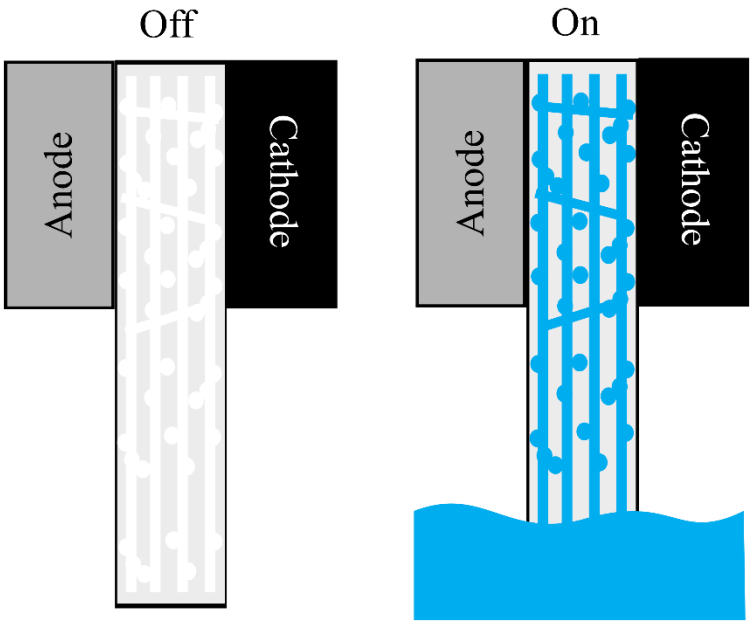

Figure 1.4.2 Electrochemical based sensing mechanism concept drawing

1.5 Research Overview

The primary objective of this research was to create a fully autonomous leak detector capable of powering an ESP8266 (3.3V and 170 mA [84]) for wireless signaling. This was done by investigating transpiration driven electrokinetic power generators which were enhanced using active electrodes and redox reactions. While the TEPG output was improved far enough to produce enough power to light an LED by using 9 devices (3 in parallel, and 3 in series) the energy output was still insufficient for the powering objective. Since electrochemistry was shown to be effective for leak detection, a battery-based device was then proposed as discussed in section 1.4.2. The theorized device was based on a single use application and to lower the environmental footprint it was designed to be recyclable. It was realized that the smart paper developed by Goodman et al. [34] could be used as a cathode for a ZAB since carbon based catalysts are commonly used for ORR [85], [85], [86], however the device still needed a cathode that could be recycled. To achieve this goal the device was designed to be fully paper based, and a paper-based anode was developed

and investigated. In the design of the paper-based zinc anode a study using ZIB technology was conducted to characterize the anode performance through a collaborative effort as well as enhance multidisciplinary research with a threefold goal in designing the anode:

1. Improved zinc ion battery cycling lifespan
2. Recyclable anode using paper making technology
3. Anode application for self-powered wireless leak detection.

After developing the zinc anode, a wick was designed, and the anode was applied in a zinc air battery that was triggered by a leak. Unfortunately, this format was still not sufficient to produce enough power thus the project was modified in pursuit of an "energy-as-data" approach. Using this idea a device was developed that was able to detect a leak by powering up a solid-state latching circuit and connecting a commercial battery to the wireless device allowing a text message alert to be sent. In this way a fully autonomous leak detector capable of wireless notification was developed and the following sections discuss the methodology and results observed in this study.

2 Methodology

2.1 Electrochemically Enhanced Transpiration Driven Electrokinetic Power Generation

2.1.1 Materials

Bleached Kraft softwood (SW, 50% Hemlock, 50% Douglas fir) and hardwood (HW, 50% cottonwood, 50% sawdust) pulps were kindly supplied in a dried mat form after chipping, screening, washing, digesting, and bleaching by WestRock and Boise Cascade companies, respectively. Chemical vapor deposition-synthesized multiwall carbon nanotubes (CNTs) with mean length, diameter, and hydroxyl content of 15 μm, 50 nm, and 0.7 %, respectively, were

purchased from Cheap Tubes Inc. after purification by acid oxidation. Silver conductive adhesive paste was supplied by Electron Microscopy Sciences. Hydrochloric acid (HCl, 1 M) and aluminum sulfate ($Al_2(SO_4)_3$, alum, 1 mM) were purchased from Fisher Scientific. High-purity copper, aluminum, and zinc foils with a thickness of 0.1 mm were supplied by Kolamoon. Ultrapure water was obtained from a Milli-Q water filtration station (18.2 MΩ·cm at 20 °C) and rainwater was collected from the run-off of Bloedel Hall and filtered through an Eaton-Dikeman grade 615 filter paper.

2.1.2 Fabrication of Electrically Conductive Paper

Electrically conductive papers with a grammage of 80 g•m^2 were produced based on our previously reported dynamic sheet forming process [35]. Briefly, a 3:1 blend of softwood and hardwood pulp was co-refined to a Canadian Standard Freeness level of 250 mL prior to being fed at a 0.35 % consistency to a Noble&Wood pilot-scale 12-inch Fourdrinier former operated at a speed of 3.2 m•min^{-1}. The CNT content was adjusted using a peristaltic pump by modulating the injection flow rate of a 5 wt.% aqueous CNT dispersion. The moisture content of the resulting papers was brought down to at least 3.5 wt% by successive gravity drainage, vacuum dewatering, pressing in a single 50-Psi roll nip, and drying over four 16 inch-diameter electric rolls operated at 80 °C. The resulting papers were wrapped around a 10-cm diameter roll, which was conditioned at 23 °C and 50 % relative humidity for at least 48 hours before being unwound and cut into sheets of 80 cm × 25 cm using an automated sheet slicer (Kunshan Dapeng Precision Machinery Co., Ltd., DP-360CQ) operated at 7 m•min^{-1}.

2.1.3 Characterization of As-Prepared Conductive Paper

The morphology of as-prepared papers was characterized by scanning electron microscopy (SEM) using a ThermoFisher Scientific Variable Pressure Apreo SEM operated at 2 kV, 13 pA mounted on conductive carbon tape. The paper thickness was measured in accordance with the T-551 TAPPI standard procedure using a micrometer [87]. A Thwing-Albert Vantage™-10 uniaxial tensile tester was employed to assess the paper strength properties along both machine- and cross-directions according to the TAPPI T-494 standard procedure [88]. Sheet resistivity was measured using a Keithly 2450 source measurement unit equipped with a four-point apparatus [89].

2.1.4 TEPG Device Preparation and Characterization

Two different TEPG configurations, namely linear and circular (Figure 2.1.1), were considered to assess the electrokinetic power generation performance of as-prepared electrically conductive paper painted with inert silver electrodes for Ohmic contact. The circular configuration comprised a 35-mm diameter paper cutout, prepared using a hole puncher, and two concentric circular electrodes painted on its surface. The center electrode had a diameter of 10 mm and the outer electrode had dimensions of 28 mm inner-diameter and 35 mm outer-diameter. The linear configuration was designed to have the same surface areas as the circular configuration for each part of the device. The linear paper strips consisted of a 64 x 15 mm^2 sheet with a 23 x 15 mm^2 and 5 x 15 mm^2 electrode on either side. The generators were then operated by using a micropipette to drop a given volume of different aqueous electrolyte solutions (*i.e.* 1 mM $Al_2(SO_4)_3$ (alum) in 1 M HCl, 1 M HCl, and deionized (DI) water) onto the smaller electrode for the linear configuration or onto the center electrode in the case of the circular device. The TEPG performance was characterized by the short circuit current (SCC), open circuit voltage (OCV), and linear sweep voltammetry, measured using a Keithley 2450 source measurement unit.

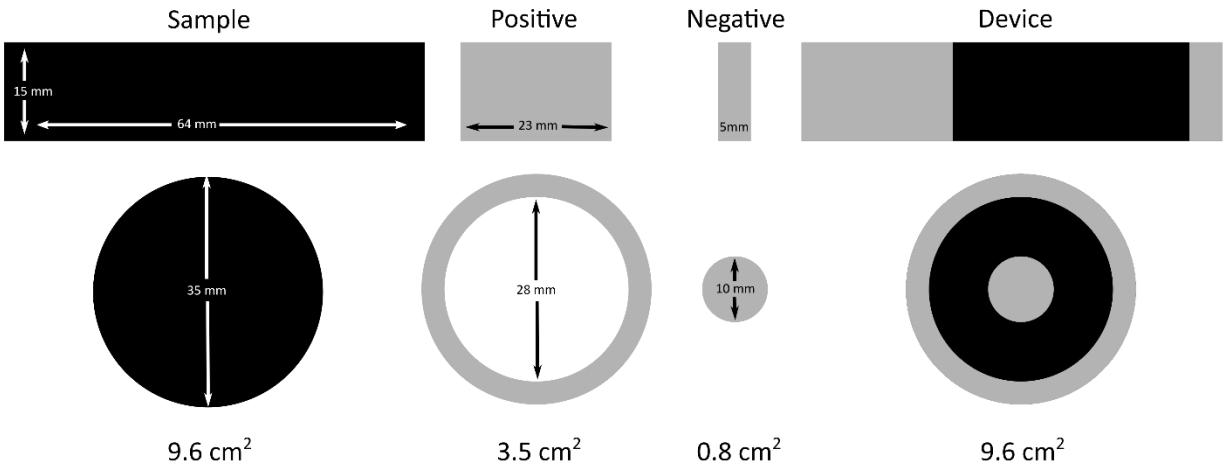

Figure 2.1.1 Linear and circular configuration device dimensions for (left to right) conductive paper, positive electrode, negative electrode, and TEPG device for both linear (top) and circular (bottom) configurations. Dimensions were chosen to achieve uniform surface area between linear and circular configurations.

2.1.5 Electrochemically (EC) Enhanced TEPG

Further optimization of the system was done by comparing inactive with increasingly active electrode materials where the electrodes were made from 0.1 mm thick copper, aluminum, and zinc foils. These devices were made using a circular configuration with copper as a current collector for the outer electrode. The electrodes were attached to the sample using a thermoplastic adhesive by hot and cold pressing onto plastic sheeting. Advanced geometric electrodes with varying numbers of 60^{o} tip angles and equivalent surface area to the 10-mm circular anodes were carved from both copper and zinc foils using a CNC (Snapmaker 2.0) equipped with an ER11 collet, 3.175-mm carving V-bit, 300 mm/min work speed, and 300 mm/min plunge speed (see table 2.1 for geometries). Geometry was calculated to ensure uniform surface area between samples by creating equilateral polygons, with side length (a), and triangles with height (h). EC enhanced devices were characterized by linear sweep voltammetry (LSV) and galvanostatic discharge using a Keithley 2450 source measurement unit.

Table 2.1 Schematic of advanced geometric electrodes with the design (top) and equations used to find length a (middle) and height h (bottom) for design in Inkscape SVG software. Note that equations were derived by summing geometric areas of polygon and triangles and equating this sum to the area of a 10 mm diameter (D) circle to ensure uniform surface area between geometries.

	3 Point	4 Point	5 Point	6 Point
Design	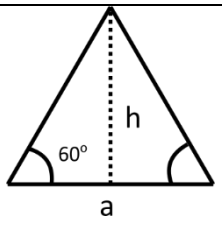	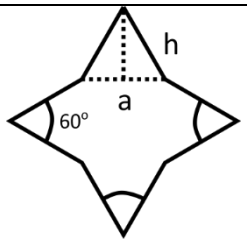	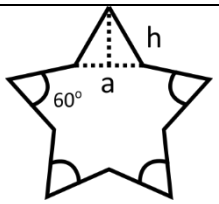	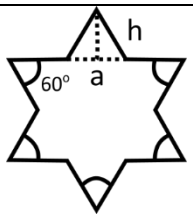
a	$\frac{D\pi^{\frac{1}{2}}}{3^{\frac{1}{4}}}$	$\sqrt{\frac{2\pi \tan(30°)\, D^2}{12}}$	$\sqrt{\frac{\pi D^2}{\sqrt{25+10\sqrt{5}}+\frac{5}{\tan(30°)}}}$	$\sqrt{\frac{\pi D^2}{6\sqrt{3}+\frac{6}{\tan(30°)}}}$
h	$a\cos(30°)$	$\frac{a}{2\tan(30°)}$	$\frac{a}{2\tan(30°)}$	$\frac{a}{2\tan(30°)}$

2.1.6 End-of-life strategies for spent EC-TEPG

Spent devices were either disposed of by incineration or recycled into new devices following a similar papermaking process as described above. For incineration, the devices were first stripped from their metallic and plastic parts, then the paper component was exposed to a butane flame for 5 s and the combustion was recorded using a video camera. In the case of recycling, several spent devices were blended in DI water. After gravimetric separation of the metallic and plastic components, the resulting mixture was redispersed in DI water by double acoustic irradiation combining both bath and probe sonication's, as reported previously [36]. The aqueous dispersion was then filtered to form the recycled conductive paper according to standard

TAPPI handsheet procedure [90]. To recover lost conductivity caused by CNT losses during recycling makeup CNT was added at varying concentrations to achieve original conductivity.

2.2 Paper Based Zinc Anode for Zinc Ion Battery Advancement

2.2.1 Materials

Bleached Kraft softwood (SW, 50% Hemlock, 50% Douglas fir) pulps were kindly supplied in a dried mat form after chipping, screening, washing, digesting, and bleaching by WestRock company. Chemical vapor deposition-synthesized hydroxyl functionalized multiwall carbon nanotubes (MWCNT-OH) with 95% purity, 50 nm diameter, 10-20 μm in length, 60 m^2/g specific surface area, and 10^2 S/cm conductivity were purchased from Cheap Tubes Inc. STA-LOK® 410 cationic potato starch was kindly donated by the Washington Pulp and Paper Foundation member Solenis. Zinc powder (100-mesh sifted) was purchased from bean town chemical with 99.9% purity.

2.2.2 Fibrous Zinc Anode Synthesis

The fibrous zinc anode was synthesized using a simple paper making process using a pre-flocculation method to aid with additive retention [91], [92], [93]. First an aqueous starch solution was prepared by dissolving STA-LOK® 410 Cationic Potato Starch in deionized water at 60 ºC to make a 0.1 wt% solution. The starch was then cooked under continuous stirring at 60 ºC for 1 hour to ensure complete dissolution of the granular structure. West Rock Softwood market pulp was prepared by disintegration according to TAPPI Standard T-205 [90] followed by dewatering and then refining. Refining was done in a Testing Machines Inc. Laboratory PFI Pulp Refiner according to TAPPI Standard T-248 [94] to achieve a final freeness Canadian Standard Freeness of 250 mL (TAPPI-227 [95]) to aid in material densification and mechanical entrapment of

additives. After refining, the pulp was redispersed in water to create a 0.3 wt% pulp slurry. Next a solution of the 100-mesh zinc powder and MWCNT-OH, was prepared with a mass ratio of 8:1 zinc to MWCNT-OH and 10 wt% concentration (g solids/g solution). The desired aliquots were added to deionized water under vigorous stirring by first dispersing the zinc followed by the carbon nanotubes. The solution was stirred for ~10 min and then ultrasonicated using a sonic probe for 2 min (Sonics & Materials inc., VCX750, 750 Watts, 20 kHz, equipped with a solid tip 630-0208-A probe). The solution then was used for anode preparation immediately after synthesis and a small sample was set aside for characterization.

Fibrous zinc anodes were prepared to have a constant mass of 0.6 g cellulose to create a fibrous mat sufficient for retention of additives. To modulate cellulose concentration the volume of zinc/MWCNT-OH solution was increased/decreased to achieve desired mass ratios (10, 20 and 30 wt% cellulose). Before synthesis the zinc/MWCNT-OH solution was pre-flocculated to aid with retention of nanoparticles by addition of cationic starch with a loading of 0.1 wt% (g starch/g solids) and stirred vigorously for 1 minute. The flocculated solution was then added to the pulp and the solution was stirred for 1 minute. The resulting slurry was then filtered to prepare the fibrous zinc anode, wet pressed, and dried in a humidity controlled atmosphere overnight according to TAPPI Standard T-205 [90]. Sample calendaring was done using a paper machine calendar by carefully feeding dried fibrous anodes to a calendar stack at 0, 2000, and 4000 PSI.

2.2.3 Zinc Anode Material Characterization

To assess the effectiveness of zinc microspheres to disperse the MWCNT-OH UV-vis spectroscopy, optical microscopy, and scanning electron microscopy (SEM) were conducted. For comparison MWCNT-OH and zinc microsphere controls were prepared in DI water at 1.11 wt% and 8.89 wt% respectively to match the 10 wt% synthesized solution with 8:1 zinc to MWCNT-

OH ratio. Sampling was done both before and after sonication and all samples (including controls) were 100x diluted. UV-vis measurements were conducted using a Perkin Elmer Lambda 750 UV-vis spectrometer equipped with integrating spere. Data was acquired at 350 nm, similar to methods reported by goodman et al. [36], using deionized water as the blank and collecting 5 replicates per measurement. To prevent particles from settling the cuvettes were covered and inverted several times before each measurement. For optical microscopy 100x diluted samples were drop-cast onto VWR 25x75x1 mm microslides and covered with VWR 24x40 mm micro glass cover. Prepared slides were imaged before drying with a Zeiss Axiolab-E-re optical microscope equipped with Zeiss Axiocam-ERc-Ss camera. Finally, SEM samples were prepared by drop casting onto conductive carbon tape attached to SEM mounts and air dried at room temperature. The resulting samples were imaged using a ThermoFisher Scientific Apreo-S Variable Pressure SEM with a working distance of 2.9 mm and electron beam of 2kV and 13pA.

To understand the physical characteristics of the synthesized Fibrous zinc anode SEM, energy dispersive electron spectroscopy (EDS), laser ablation mass spectroscopy (LA-MS), X-ray diffraction spectroscopy (XRD), and tensile failure testing were performed. Fibrous anode samples were prepared for SEM/EDS analysis of both the sample surface and cross section. Cross sections were prepared by cryo-fracturing (dipped in liquid nitrogen and cleaved with a razor and hammer) and both cross sectional and surface samples were mounted on carbon tape for analysis. SEM images were acquired with a working distance of 10 mm and electron beam of 2 kV, and 13 – 25 pA. EDS data was gathered with the Apreo SEM equipped with Oxford Instruments EDS – Dualbeam FIB-SEM with a working distance of 10 mm and electron beam of 10 kV and 100 nA. To qualitatively assess varying zinc concentration through the thickness of the anode LA-MS was conducted. The samples were prepared by soaking in an indium solution and mounting onto glass

a substrate. The samples were then laser ablated with a 3 Hz repetition rate, 1 J/cm^2 fluence, and 40 μm spot size under helium atmosphere (0.7 L/min) with a signal homogenization tube implemented. Data reduction was performed using Lolite version 4 software and zinc concentration were qualitatively estimated by the ratio of ^{64}Zn/^{115}In isotopes. To assess crystallographic changes of the anode samples were placed on a clean silicon wafer and XRD was performed on a 50 kV Bruker D8 Powder Diffractometer equipped with high-efficiency Cu (1.54056 Angstrom) anode, 1000 uA microfocus x-ray source, 100K Pilatus large-area 2D-detector. XRD measurements were collected from 10^o – 87^o (2θ) with 5.5^o increments and a scan rate of 30 s per increment. Lastly, anode mechanical properties were assessed by tensile strength testing according to a modified TAPPI Standard T-494 [88] (100 mm gauge length, 25 mm sample width) using a Thwing-Albert Vantage^{TM}-10 uniaxial tensile tester.

2.2.4 Zinc Anode Electrochemical Characterization

Electrochemical performance was assessed by galvanostatic charge/discharge (GCD), cyclic voltammetry (CV), and electrochemical impedance spectroscopy (EIS) conducted on assembled coin CR2032 cell batteries. Coin cell batteries were prepared by placing the prepared zinc anode into the negative casing followed by a Whatman grade GF/A glass fiber separator and drop casting 80 μL of 3 M zinc tirfluoromethanesulfonate ($Zn(CF_3SO_3)_2$) electrolyte onto the separator. A vanadium hydroxide cathode prepared by Jia et al. [62] was used for testing and was placed onto the separator followed by the coin cell spacer, wave spring, and positive cap. GCD testing was done on prepared coin cells using a Neware Battery Testing Systems (CT-4008) to assess both cycling lifespan and rate capabilities of the battery. Battery cycling was done with a constant charge/discharge current density of 4 A/g and a cutoff voltage of 0.2 V cycling 3000 times.

Rate testing was done at 0.5, 1, 2, 3, and 4 A/g for 5 cycles each to assess the rate capabilities of the anode.

2.3 Wick Design and Implementation of Electrochemical Leak Detector

2.3.1 Materials

Bleached Kraft softwood (SW, 50% Hemlock, 50% Douglas fir) pulp was kindly supplied in a dried mat form after chipping, screening, washing, digesting, and bleaching by WestRock and Boise Cascade companies, respectively. Ground Calcium Carbonate was donated by Washington Pulp and Paper Foundation member Solenis and was ground with a mortar and pestle and oven dried before use. Hydrochloric acid (1 N standard solution) was purchased from Fischer Scientific. Potassium hydroxide was purchased from Sigma Aldrich in the form of 90% pure flakes. Smart paper and fibrous zinc anodes were prepared as discussed in sections 2.1 and 2.2.

2.3.2 Wick Synthesis

To synthesize wicks, 80 g/m^2 handsheets were synthesized by first disintegrating West Rock Softwood market pulp by disintegration according to TAPPI Standard T-205 [90]. The fiber was used without further refining having an average Canadian Standard Freeness of ~750 mL and was diluted to produce a 0.3 wt% pulp slurry. A ground calcium carbonate slurry was prepared by diluting the $CaCO_3$ to form a 10 wt% slurry which was then ultrasonicated using a sonic probe for 2 min (Sonics & Materials inc., VCX750, 750 Watts, 20 kHz, equipped with the solid tip 630-0208-A probe). Next, 400 mL of pulp slurry was measured (1.2 g pulp fiber) and aliquots of $CaCO_3$ solution were added to the slurry at a charge of 0.12, 0.6, and 0.8 g $CaCO_3$/g fiber and mixed for ~10 minutes. The resulting slurry was then filtered , wet pressed, and dried in a humidity controlled atmosphere overnight according to TAPPI Standard T-205 [90] to prepare a $CaCO_3$ paper. The

paper was then cut into 1.5 x 6 cm^2 strips and placed into a petri dish containing deionized water. Subsequently, 1 N HCl was added dropwise onto the soaking paper strip causing the chemical reaction shown in equation 2.3-1 and was continued until CO_2 gas bubbling ceased. The $CaCO_3$ dissolved paper strip was then rinsed three times with deionized water and oven dried at 80 ^oC for ~1 hour and then allowed to acclimate in the laboratory for 24 hours. The samples were cut to a 5 cm length and doped with KOH electrolyte by preparing a 6 M KOH solution and drop casting three 100 μL droplets equally spaced on the wick followed by drying at 80 ^oC for ~ 1 hour. The final prepared wick was allowed to acclimate to the laboratory room temperature and humidity for 24 hours before used.

Equation 2.3-1 Wick Synthesis Chemical Reaction

$$CaCO_3 + 2HCl \rightarrow CaCl_2 + CO_2 + H_2O$$

2.3.3 Wick Characterization

Wicking speed was measured in undoped samples using an iPhone camera with a frame rate of 30 frames per second mounted on a phone holding stand and levelled using cardboard shims. The sample was held in a clamp with a ruler carefully placed next to it, so the wick and ruler were parallel and aligned on the same vertical plane which was also leveled. The sample plane was then oriented to ensure the camera plane and sample plane were parallel so the ruler could be used to calibrate image processing. The camera video recording was initiated and a petri dish filled with water was raised using a laboratory jack stand until the edge of the wick was in contact with the water. Wicking measurements were made by first extracting frames using VLC media player's scene filter function and then ~20 images were chosen for measurements to ensure adequate representation of the wicking curve. Next the wetted area of each image was measured using ImageJ software by calibrating a pixel scale ratio using the ruler and then using contrast

thresholding and masking to extract area measurements. Finally, the height was calculated by dividing the area by the wick thickness (1.5 cm) and in this way an average of the wicking height across the sample width was estimated.

The morphology of the wick was evaluated by SEM using a ThermoFisher Scientific Variable Pressure Apreo SEM operated at 2 kV, 13 pA, with a 10 mm working distance. To prepare the samples for analysis they were cryofractured by freezing in liquid nitrogen followed by fracturing with a razor and hammer. The cryofractured samples were then mounted onto an SEM stage and coated using a Leica EM ACE600 SEM sample coater equipped with sputter head and platinum target. The paper thickness was measured in accordance with the T-551 TAPPI standard procedure [87] using a digital micrometer. A Thwing-Albert Vantage™-10 uniaxial tensile tester was employed to assess the paper strength properties according to a modified TAPPI T-494 standard procedure [88]. Finally, the porosity of the wick was qualitatively assessed by SEM mask area fraction where the cross section was converted to a binary image by first blurring the picture to smooth the contrast using ImageJ software and then using a contrast threshold to convert the darkest areas, associated with voids in the paper, to a black mask (see figure 2.3.1) and the area fraction of the mask was calculated.

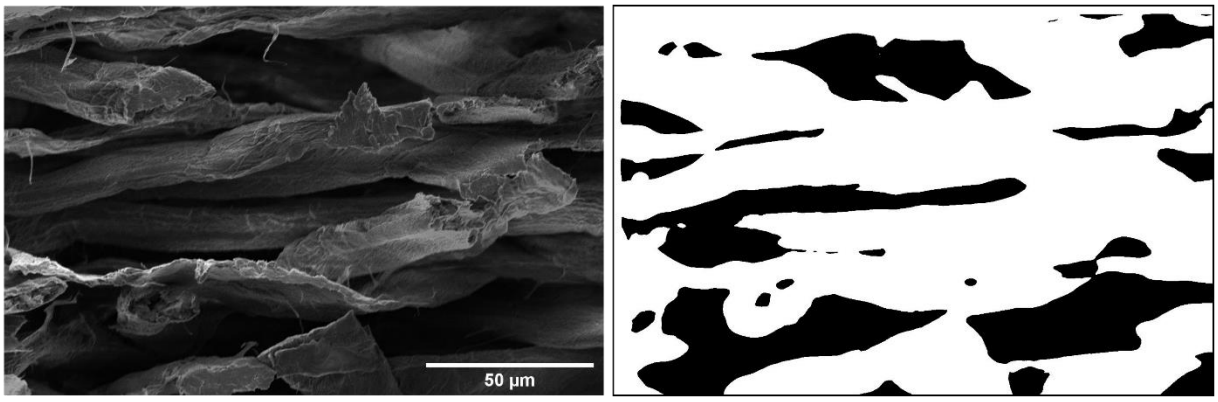

Figure 2.3.1 SEM image of sample cross section with approximate masked voids.

2.3.4 Zinc Battery Leak Detector Device Design and Characterization

To prepare the leak detection device first a coin cell battery holder purchased from LampVPath was soldered to a through hole printed circuit board (PCB) with wire connections made to the positive and negative terminals. As the cathode material, 15 wt% electrically conductive paper was synthesized as discussed in section 2.1.2 and prepared at 80 gsm and cut to 11 mm diameter circles using a hole punch. For the anode, the 10% cellulose fibrous anode calendared at 4000 psi was synthesized and prepared as discussed in section 2.2.2 and a 13 mm diameter circle was punched from the sheet. To provide a breathable layer to allow oxygen to quickly reach the cathode surface an 11 mm diameter circle of stainless-steel mesh was cut using a hole punch. For current collectors 16 mm steel plates were salvaged from spent ZIB coin cells and cleaned by bath sonication in DI water, methanol, and acetone for 5 minutes each. The device was then fabricated by combining the component as shown in figure 5.2.4 ensuring the anode and cathode were centered on the collectors and the top of the wick was aligned tangent to the collector. The assembly was then carefully slid into the coin cell holder which held the components in place

by spring force and the entire device was wrapped in a layer of duct tape to prevent the parts from moving out of alignment.

To measure the detector performance the device was clamped to a stand and a petri dish filled with water was raised to contact the wick using a jack stand. Voltage measurements were acquired using a Keithley DMM 6500 6.5 Digital Multimeter equipped with 2000-SCAN 10 channel scanner card set to acquire data at 1 second intervals. Constant current measurements were made using a Keithley 2450 source measurement unit in four wire configuration sourcing -100 μA and measuring voltage with a 2V limit.

2.3.5 Energy as Data Leak Detector Device Simulation and Design

To allow for higher energy devices to be powered by the TEPG or zinc battery leak detector an analog circuit was developed to activate a battery power source when the device was wetted. To aid in the design of this circuit LTSpice simulation software developed by Linear Technologies was used for SPICE (simulated program with integrated circuit emphasis) simulations. The goal of designing this circuit was to power an ESP8266 Arduino based Wi-Fi module which requires a minimum of 3.3V and 150 mA to send a Wi-Fi signal [84] which can be provided by four Duracell OP1500 AA alkaline manganese dioxide batteries connected in series [96]. The batteries were assumed to have a constant voltage of 6V and the load of the ESP8266 during Wi-Fi signaling was simulated using a constant load circuit element. To assess the devices' effectiveness to activate the circuit, data sets from TEPG results were imported into the circuit design using an independent voltage source with PWL file import. The simulation was computed using a transient DC analysis.

3 Electrochemically Enhanced Transpiration Driven Electrokinetic Power Generator

3.1 Background

With the continued acceleration of climate change, new solutions for renewable energy are becoming increasingly relevant [97], [98], [99], [100]. Modern advancements in nanomaterials and materials science have led to novel methods of clean energy generation ushering in a new era of sustainable energy transduction. Currently investigated solutions include triboelectric [101], [102], [103], piezoelectric [104], [105], thermoelectric [106], [107], [108], solar [109], [110], and moisture [40], [41], [111] transducers. These generators often employ cutting edge composite and nanostructured materials, applying cross disciplinary knowledge to attain novel methods of power generation.

Moisture transducers, more commonly referred to as moisture enabled generators (MEGs), harvest energy from water transport over a material surface. While the mode of energy generation is still not entirely understood several mechanisms have been proposed including streaming current, pseudo-streaming current, ion gradient diffusion, and several others [40], [41], [42], [43], [44], [45], [46], [47], [48], [49], [50], [51], [52], [53]. A subset of MEG's takes advantage of the wicking action of mesoporous structured materials to create a transpiration driven electrokinetic power generator (TEPG) [34], [43], [46], [47], [112], [113], [114]. These generators are of particular interest since they can harness energy from the Earth's hydrological cycle via transpiration forces by utilizing asymmetric wetting, wicking, and evaporative forces [40], [43], [46], [47]. For example, conductive textiles have been integrated into fully autonomous wearable electronics, harvesting moisture from the human body to power watches and smart textiles [57],

[112], [115]. Bae et al. produced a self-operating TEPG by coating a conductive cotton mat with $CaCl_2$, a deliquescent, which then lit a red light emitting diode (LED) in a humid environment via reuptake of water vapor for several days [47]. It is apparent that TEPGs have great potential, however their meager power generation of 10 - 100 μW maximum theoretical power (MTP) is ill suited for many application, even among wearable electronics [43], [47], [115], [116]. In an attempt to overcome this limitation Bae et al. developed a titanium carbide MXene ($Ti_3C_2T_x$) based TEPG with MTP of 4.4 mW, reaching unprecedented levels of TEPG power generation [46]. It is possible that further electrochemical enhancement may improve upon device design, demonstrated by Zhang et al. who developed a moisture-triggered galvanic cell using similar principles applied by TEPG studies showing a distinct power increase when copper electrodes compared to highly unreactive platinum [111].

Recently Goodman et al. developed a carbon nanotube cellulose composite using scalable paper making methods [34], [38]. In this study carbon nanotubes were well dispersed within a cellulose matrix creating a conductive material capable of liquid sensing via water uptake. Carbon nanotubes (CNTs) are of particular interest for TEPGs due to their unique capability to generate electricity from electron drag caused by phonon waves induced by fluid flow [44], [45], [117]. In this study the carbon nanotube embedded "smart paper" produced by Goodman et al. was investigated for its potential to be applied as a TEPG. This device was optimized and then further enhanced using electrochemical methods via reactive electrodes.

3.2 Results and discussion

3.2.1 Material fabrication and characterization

Paper with a grammage of 80 $g.m^{-2}$ was produced using a previously established continuous-flow web forming method (figure 3.2.1a) [35], where various quantities of hydroxyl-functionalized CNTs pre-adsorbed with cationic surfactants at a 2:1 CNT:surfactant mass ratio were introduced as the electroactive materials to impart conductivity to the cellulose network for efficient electricity harvesting. The process involved forming sheets of bleached cellulose fibers on a 12-inch Fourdrinier, followed by sequential dewatering through gravity drainage, vacuum dewatering, single-nip pressing, and drying using four heated rolls.

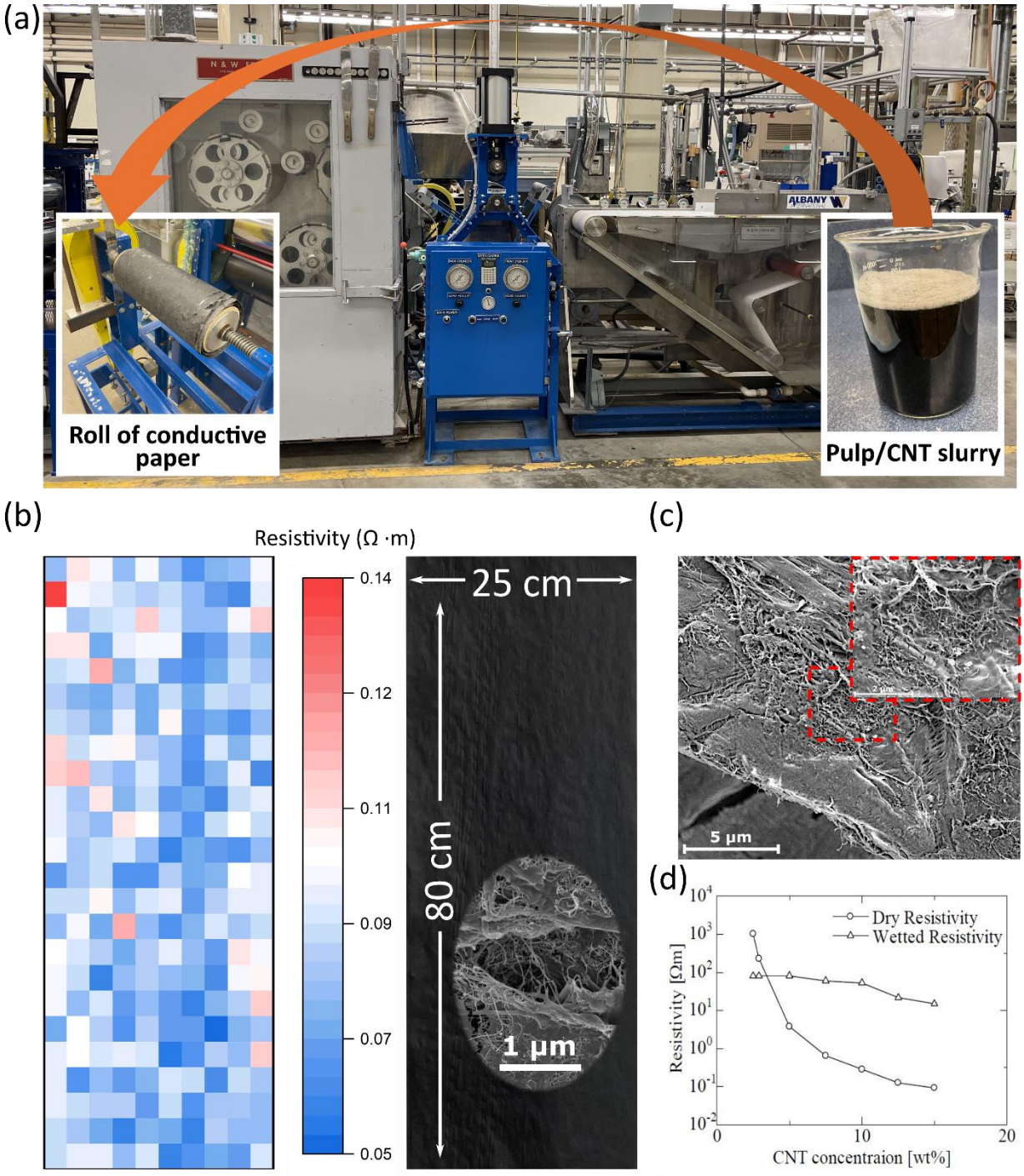

Figure 3.2.1 (a) Pilot scale paper machine used to make smart paper with starting pulp slurry (right) and final conductive paper roll (left). (b) A Piece of smart paper cut from the smart paper roll (25 cm x 80 cm) with heat map of resistivity measurements using four-point probe method. (c) SEM image of smart paper cross section at increasing zoom.

Paper with different sheet resistances were prepared by simply varying the amount of CNTs introduced to the pulp slurry prior to sheet formation and dewatering (Table 3.1). As-produced paper had a consistent thickness of 0.12±0.02 mm and exhibited a uniform CNT distribution across the sheet without obvious nanoparticle aggregation independently of their CNT content (Figure 3.2.1b). This is further demonstrated by the heat map in figure 1.3.1b**,** showing 240 four-point probe resistivity measurements collected across a representative 80-cm x 25-cm sheet. The spatial variability of resistivity calculated from the FWHM of the Gaussian distribution for a 0.25 m^2 sheet of paper prepared with the highest CNT content (*i.e.* 14 wt.%) is 35 %. The variation between the in-plane resistivities among sheets produced under similar conditions but across multiple batches was 7%. In addition, there was not a statistically significant difference in electrical conductivity between each side of the paper based on a one-way analysis of variance at a 95% confidence level. Top-view (Figure 3.2.1b) and cross-sectional (Figure 3.2.1c) electron micrographs of cryo-fractured samples where CNTs spanning between neighboring pulp fibers were observed across the paper further confirm the excellent distribution of CNTs within the cellulose network. The evolution of dry sheet resistivity as a function of CNT content reveals a typical percolative trend consistent with networked conductors, while the wet sheet resistivity remains relatively constant regardless of the CNT concentration (Figure 3.2.1d).

Besides sheet resistivity, the capillary flow through the paper was also influenced by the presence of hydrophobic CNTs. Figure 3.2.2-a reveals a gradual decrease in both the wicking rate and wet area when larger quantities of CNTs were incorporated in the paper. At 14 wt.% CNT level, the wicking rate and wet area were reduced by 87 % and 16 %, respectively, compared to paper prepared under similar conditions but without any CNTs. The mechanical properties of the conductive papers were evaluated using a Thwing Albert model 1760 uniaxial tensile tester

according to Tappi T494 standard procedure [88]. Figure 3.2.3 indicates that both the strength, stiffness, and toughness of conductive paper decreased with increasing CNT content. These results are consistent with previous works reporting similar reduction in the mechanical performance of paper at elevated CNT loadings and can be attributed to the presence of non-polar CNTs disrupting inter-fiber bonding, thereby weakening the polar networked structure. In summary, higher CNT contents yield weaker paper with greater electrical conductivity and lower wicking rates for aqueous solutions. The above-described flow-through manufacturing approach combined with the inherent porosity of electro-active paper for passive and efficient fluid transport has potential to enable scalable and low-cost energy harvesting.

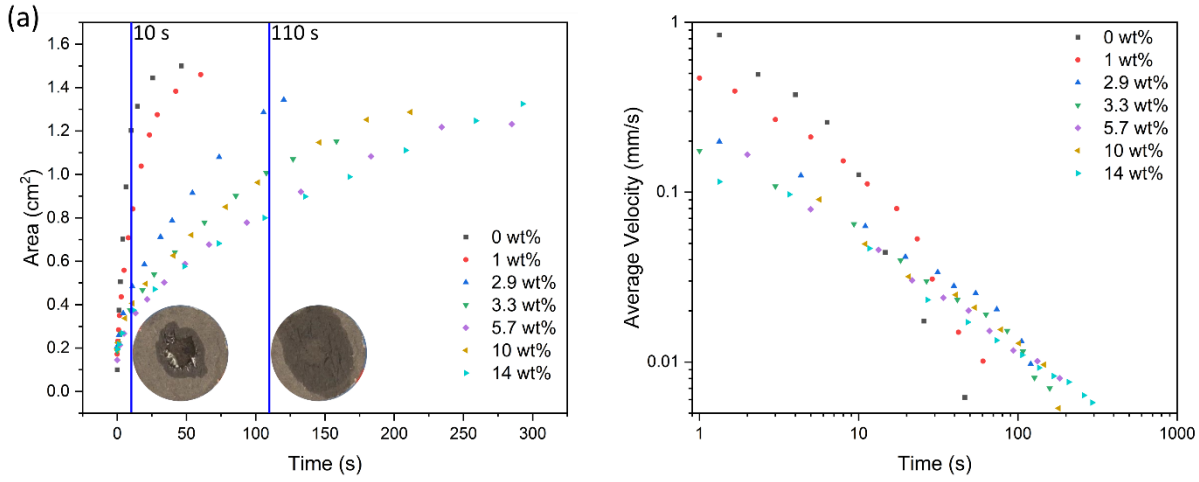

Figure 3.2.2 (a) Wet area and (b) wicking rate of papers with varying CNT contents upon wetting with 30 uL deionized water. Wet area and wicking rate data were extracted from 30-fps video recordings using ImageJ software, as examplified in the insets in (a).

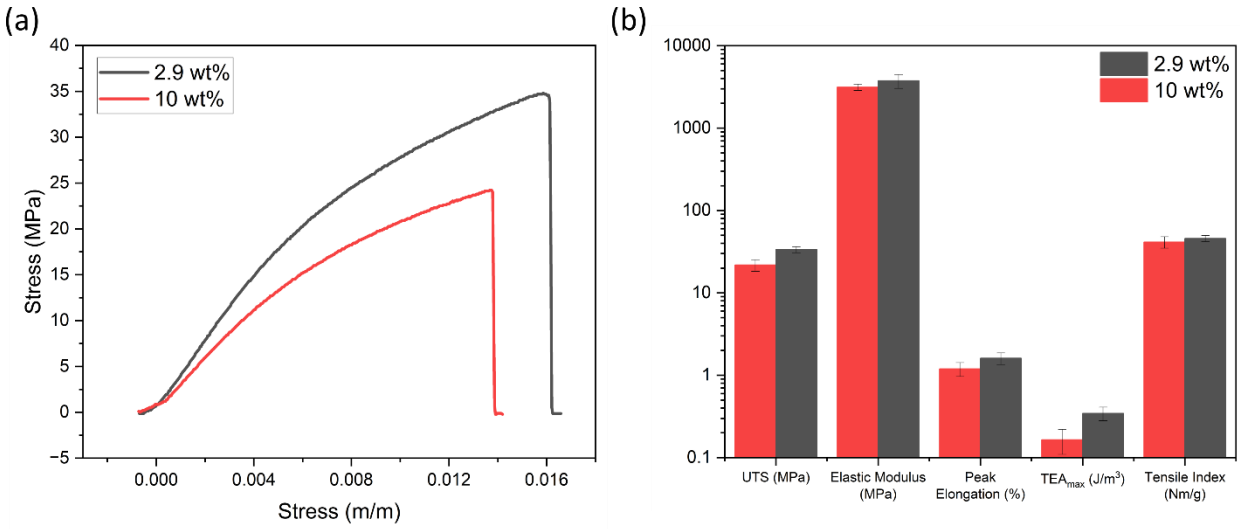

Figure 3.2.3 (a) Stress strain curve of 2.9 and 10 wt% CNT loading. (b) Calculated stress strain metrics extracted from replicate tensile tests (5 replicates) with confidence intervals as error bars

3.2.2 TEPG performance

Unlike traditional micro-hydro-generators that rely on mechanical energy, asymmetrically wet conductive paper leverages the abundant capillary channels within the fibrous network to facilitate a transpiration flow driven by natural evaporation. This flow, coupled with the presence of oxygen functions on the surface of CNTs and pulp fibers that can release charged species upon liquid infiltration, induce the formation of an electrical double layer at the solid-liquid interface for the continuous harvesting of electricity based on the pseudo-streaming potential mechanism [43], [46]. Transpiration-driven generators, referred to as TEPGs, were fabricated by pasting inert silver electrodes onto the different conductive paper and their energy generating performance was characterized by measuring the short circuit current (SCC), open circuit voltage (OCV) and linear sweep voltammetry (LSV) upon dropping either DI water, aqueous HCl or alum solutions. Two types of paper-based TEPG devices, reported henceforth as linear and circular TEPGs, were prepared using a 450-nm excitation radiation of a 10-W diode laser engraving system (Snapmaker

2.0, Shenzhen, China), as detailed in figure 2.1.1. The linear configuration consisted of a 15-mm wide by 64-mm long cutout strip of conductive paper with both ends connected to Ag electrodes, one of which was wetted by 30 μL of aqueous electrolyte solution **(**figure 3.2.4-a). For circular devices, a 30-μL droplet of electrolyte solution is deposited at the center of a 35-mm diameter paper disc whose back side is connected to two concentric Ag electrodes (Figure 3.2.5-a). For comparison purposes, these TEPG configurations were designed such that the areas of both Ag electrodes and conductive paper were the same in each case (*i.e.* linear and circular devices). Note that all tests were conducted at room temperature and ambient relative humidity to simulate real-world applications. When 30 μL of DI water was deposited onto the negative electrode, linear TEPG devices produced an OCV about 0.29 V and a SCC about 0.10 μA (figure 3.2.4-b-d), while circular TEPG systems exhibited OCV and SCC values of 0.10 V and 1.5 μA, respectively (figure 3.2.5-b-d). As a result, the maximum theoretical power output for the circular configuration was an order of magnitude higher than that of the linear TEPGs. In agreement with previous studies,[43], [46], [114], [115], [116] the OCV and SCC were improved with the utilization of aqueous electrolyte solutions. A 30 % increase in both OCV and SCC values was observed for the linear TEPGs when 1 M HCl was employed instead of DI water, while a nearly 3-fold enhancement in both OCV and SCC was achieved in the case of circular TEPGs. Electricity generation was further increased with the addition of a high valency charge carrier like Al^{3+} (*i.e.* 1 mM alum) in an HCl solution, reaching maximum OCV and SCC values of 0.23 V and 7.1 μA, respectively. The resulting energy density was greater than previously developed paper-based generators [118] and comparable to other cotton-derived systems [43], [119].

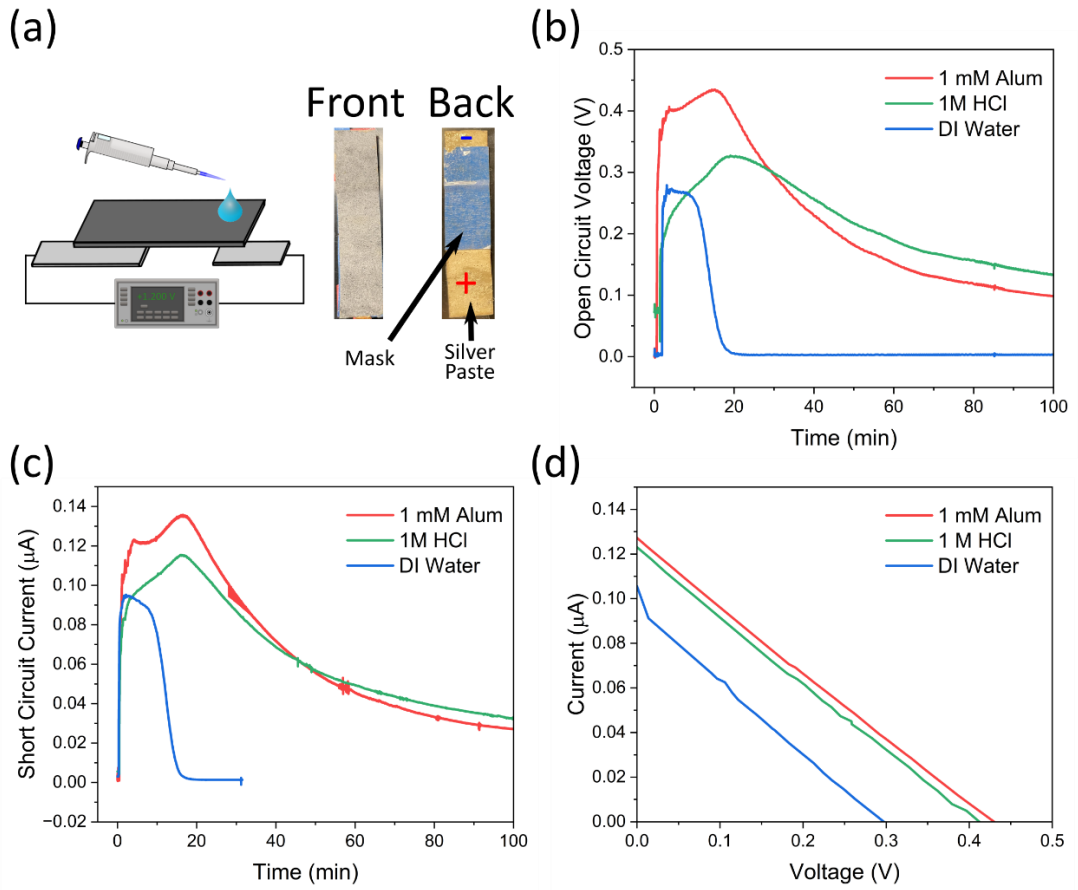

Figure 3.2.4 (a) Schematic showing linear TEPG configuration as well as images of the device. (a) Open circuit voltage vs time, (b) short circuit current vs time, and (c) linear voltammetry profiles of linear TEPG for 30 μL droplet of several electrolytes.

The power output was also significantly influenced by the paper's composition. Very little energy generation was observed at low CNT contents, while peak performance was achieved at 2.9 wt% (table 3.1). The porous and hydrophilic nature of the cellulose matrix coupled with the CNTs' electrical conductivity facilitated rapid wicking behavior [120], [121], [122], reducing the TEPG's internal resistance [35], and increasing electron drag and streaming potential mechanisms [43], [48], [49], [50], [117]. However, the paper became excessively hydrophobic at elevated CNT loadings, thereby drastically decreasing the wicking velocity (figure 3.2.2-b).

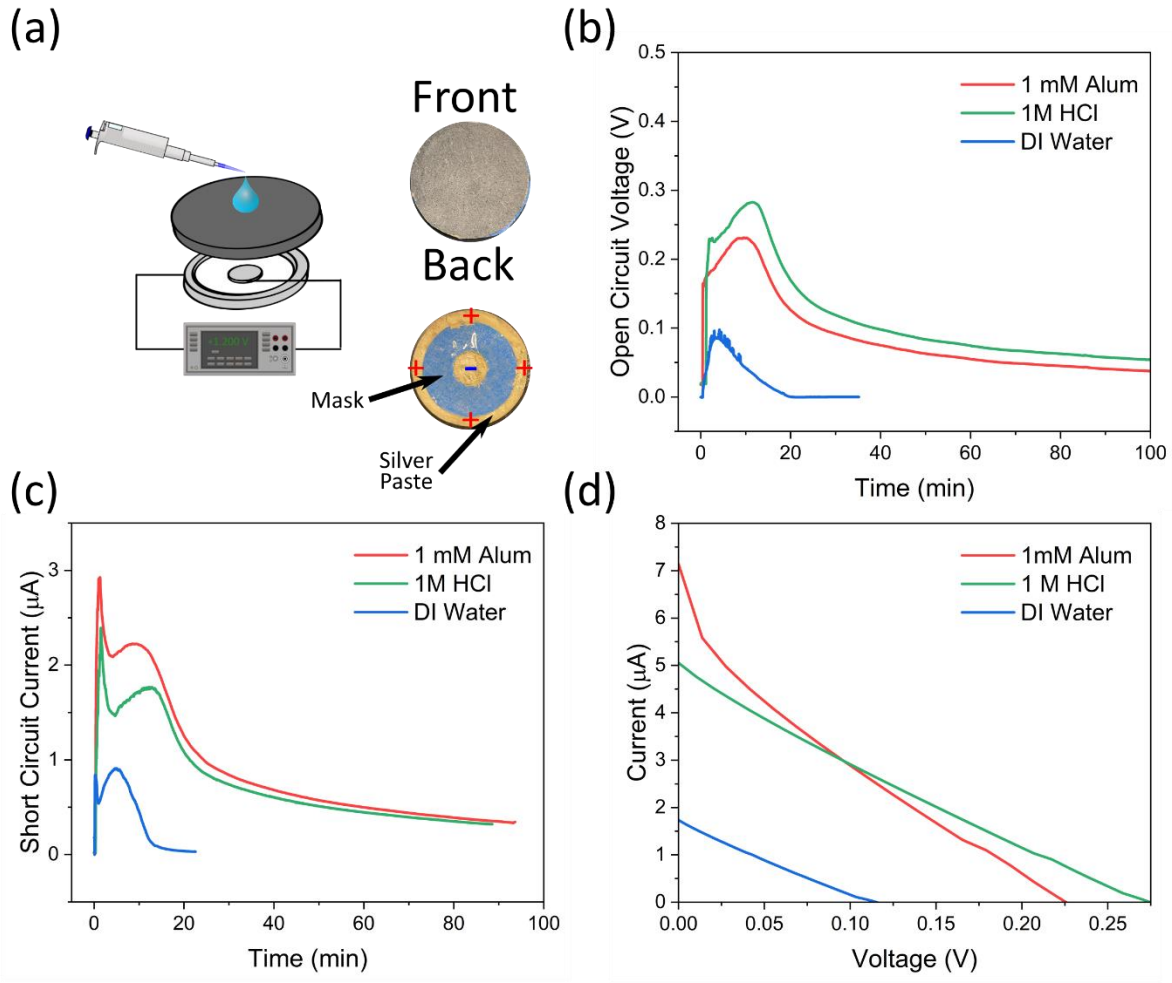

Figure 3.2.5 (a) Schematic showing circular TEPG configuration as well as images of the device. (a) Open circuit voltage vs time, (b) short circuit current vs time, and (c) linear voltammetry profiles of circular TEPG for 30 μL droplet of several electrolytes.

This can be explained by an increasing resistance to the liquid flow caused by increasing contact and reduced pore size, as described by Hertaeg et al [120]. The reduction in fluid velocity promoted the accumulation of charge at the electrode surface, while faster fluid velocity induced a higher current flow through ion transport. These results were related to Ohm's law, as reflected by the linear voltammograms shown in figures 3.2.4d and 3.2.5d.

Table 3.1 Effects of Resistivity on TEPG performance

CNT Loading (wt%)	Resistivity (Ω m)	V_{req}[1] (μL)	TEPG (DI water)		Electrochemically Enhanced TEPG (1 mM Alum)	
			V_{OC}[2] (mV)	I_{SC}[3] (μA)	V_{OC} (V)	I_{SC} (mA)
0[4]	N/A	10	18 ±[5] 6.4	0.31 ± 0.11	0.79 ± 0.03	4.0 E-5 ± 3.7E-6
1[4]	N/A	10	22 ± 11	0.57 ± 0.29	1.44 ± 0.07	3.1E-7 ± 8.5E-7
2.9	230	10	110 ± 5.2	1.45 ± 0.23	1.27 ± 0.04	6.1E-3 ± 0.05E-3
3.3	7	30	102 ± 3.9	0.73 ± 0.05	0.84 ± 0.26	0.32 ± 0.46
5.7	2	30	70 ± 7.1	0.70 ± 0.16	0.93 ± 0.08	1.24 ± 0.24
10	0.23	30	1.3 ± 0.35	0.17 ± 0.04	1.08 ± 0.05	2.23 ± 0.16
14	0.11	30	0.49 ± 0.01	0.16 ± 0.003	0.60 ± 0.05	1.45 ± 0.23

[1] V_{req} – Volume required to quickly wet negative electrode area without fully wetting TEPG due to varying hydrophobicity.

[2] V_{OC} – Open circuit voltage.

[3] I_{SC} – Short Circuit Current.

[4] The resistivity for 0 and 1 wt% samples were too large to measure with available equipment.

[5] ± represents 95% confidence interval.

3.2.3 Semiempirical TEPG Model

To provide a fundamental understanding of the TEPG mechanism, a quasi-one-dimensional numerical simulation was devised considering the variation of cross-sectional area along the flow. This model was developed by Professor Hidemasa Takana and his group at Tohoko University Institute of Fluid Sciences in Sendai, Japan in collaboration with the Dichiara Group at the University of Washington Bioresource Science and Engineering Department. In the proposed

model, the ions were assumed to be composed of H_3O^+ and OH^- from H_2O with concentrations of 0.1 mmol/m^3 for both ions. The ion continuity equations with drift-diffusion approximation were solved coupled with Poisson's equation for electric potential with inclusion of the space charge [123]. Figure 3.2.6-a shows the schematic illustrations of the circular TEPG configuration and its equivalent electric circuit. The computational domain was set between the inner and outer electrodes along the radius. The equivalent circuit consisted of the electromotive force, V_{op} (*i.e.* open-circuit voltage), internal resistance, R_{int}, and external load resistance, R_L. The internal resistances, which consisted of the resistances from the wet and dried regions of the conductive paper in series, were obtained from the measured electrical resistivities reported in figure 3.2.1-d. The liquid propagation velocity was taken from experimental observation (figure 3.2.2-a). The space charge density and electric potential distribution are shown in the insert of figure 3.2.6-b. At t = 5 s, the interface between dry and wet region is located at the peak electric potential (*i.e.* 8 mm), as indicated by the dashed dotted line in the insert of figure 3.2.6-b. The charge separation came from the difference in diffusion velocity between ions. The larger diffusion coefficient of hydronium ions yielded a locally higher positive space charge just behind the interface, while the left-behind negative ions created a locally larger negative space charge in the upstream. The electric potential peaked at the interface in the wet region due to the positive space charge near this location, generating an electromotive force. As the interface propagated (*i.e.* at t = 10 s and 15 s), the ions drifted to be electrically neutralized by the internal electric field, which decreased over time due to the reduction in local space charges. This induced an increase of the electromotive force with time, as reflected in figure 3.2.6-b.

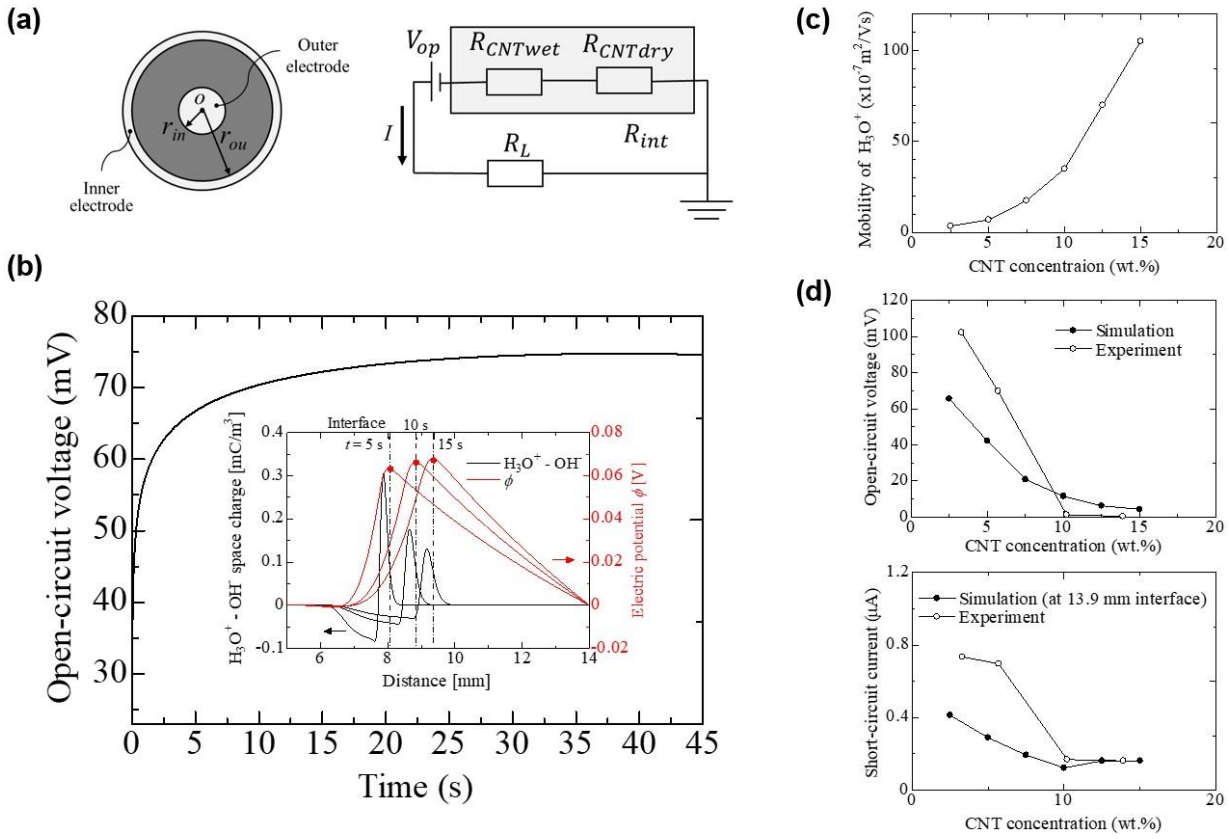

Figure 3.2.6 (a) Schematic showing the circular TEPG configuration, and its equivalent electric circuit used for the numerical modeling. (b) Decrease of the open voltage as a function of time with the distributions of space charge density and electric potential shown in the insert. (c) Effective mobility of H_3O^+, and (d) comparison between numerical simulation and experiment for OCV and SCC.

Since proton transport rate is known to be considerably enhanced in CNTs [124], the mobility of H_3O^+ was adjusted in the simulation based on the CNT content of the conductive paper, as described in figure 3.2.6c. An augmentation of the CNT concentration led to a decrease in OCV (*i.e.* electromotive force) and SCC (figure 3.2.6-d), which can be attributed to the above-described effect of self-neutralization through ion drift driven by internal electric field. The qualitatively good agreement between numerical simulation and experimental data (figure 3.2.6-d) demonstrates the validity of this model.

3.2.4 *Electrochemical Enhancement*

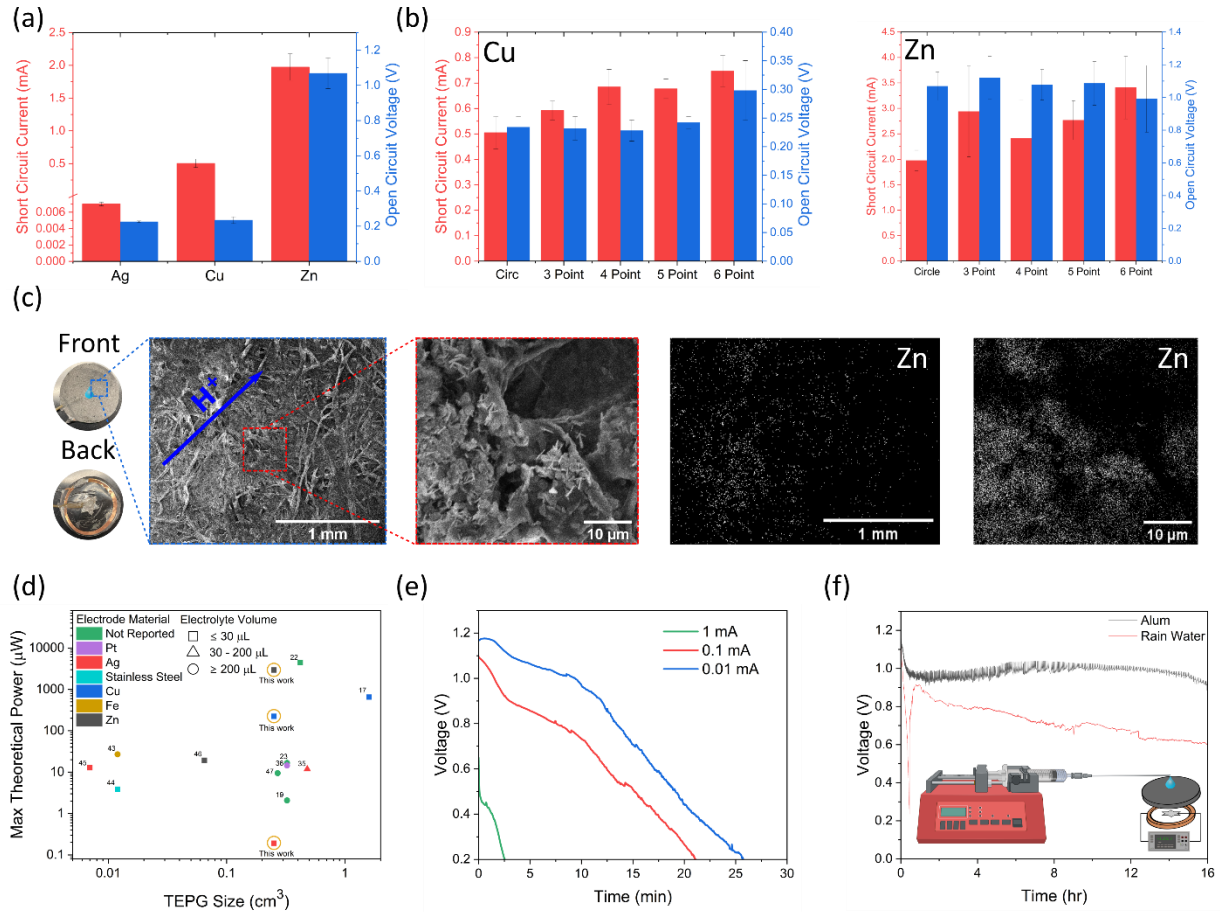

Figure 3.2.7 (a) Short circuit current and open circuit voltage of different anode materials. (b) Short circuit current and open circuit voltage of varying CNT concentration for zinc anode. (c) Short circuit current and open circuit voltage of tip enhanced anodes. (d) Ashbey plot comparing performance of this works electrochemically enhanced TEPG with other TEPG's presented in the literature [43], [46], [47], [59], [115], [116], [119]. (e) Galvanostatic discharge of 6-point zinc anode TEPG at varying constant currents. (d) Galvanostatic discharge of 6-point zinc anode while continuously dropping alum solution at a rate of 0.04 mL/hr under a constant current of 0.01 mA.

For enhancing device performance further, active electrodes can be employed to generate electrochemical energy through redox reaction in combination with the TEPG harvesting mechanism. Figure 3.2.7-a shows the device performance for increasingly active electrodes, displaying drastic increases in both SCC and OCV when Cu and Zn electrodes were used instead

of inert Ag electrodes, with Zn performing the best. Adopting Zn as the electrode material not only enhanced device performance over precious Ag, but also significantly lowered the manufacturing cost. The occurrence or redox reactions to increase performance was confirmed using EDS measurements as shown in figure 3.2.7-c. A TEPG device was carefully disassembled and cleaned before SEM/EDS imaging to assess if ZnO was deposited onto the conductive paper as a result of the redox reactions seen in acidic zinc air batteries [85]. The images show an obvious presence of Zn resembling a gradient in the direction of electrolyte wicking represented by a blue arrow with the label H^+ further confirming EC enhancement. At this point it became apparent that an increase in CNT content could aid in acidic zinc air battery redox mechanisms [125]. To aid in wetting and take advantage of higher active component concentrations, larger volumes of electrolyte were dropped onto varying CNT concentration of smart paper to assess the possible advantage of higher CNT content. Table 3.1 shows again a peak concentration occurring at 10 wt% loading of CNT. As CNT concentration increased, so did active material for zinc air redox reactions, however beyond this point wetting still became an issue even at very large volumes of electrolyte. The optimal device configuration was found to be 10 wt% CNT by dropping 30 μL of electrolyte onto the zinc anode.

Besides electrode composition, the electrode shape was also engineered to enhance device performance. Table 2.1 reports the design of four different electrode geometries with the same exact area but exhibiting an increasing number of high-curvature tips, including triangular- (*i.e.* 3 tips), isotoxal- (*i.e.* 4 tips), pentagram- (*i.e.* 5 tips), and hexagram-shaped (*i.e.* 6 tips) electrodes. It is well-known that sharp tips create intense electric field concentrations at the tips' apex, attracting and accumulating charges in the vicinity of the active sites which accelerates redox reactions, thereby inducing higher current outputs [126]. The beneficial effect of the tip-enhanced local

electric field in facilitating mass transfer is validated by the higher current generated in the case of devices comprised of negative electrodes designed with sharp edges compared to circular-shaped electrodes, with up to 48 % and 69 % increases in SCC for Cu and Zn electrodes, respectively (figure 3.2.7b). These augmentations in SCC were statistically sound with p-values < 0.05 based on analysis of variance conducted at a 95 % confidence level. Increasing the number of tips gradually improved the current generation without negatively affecting the open circuit voltage (OCV) for both Cu (figure 3.2.7b-left) and Zn (figure 3.2.7b-right) electrodes. Noteworthy, the specific maximum theoretical power (MTP), defined as the product of SCC and OCV normalized by the material's volume, reached an impressive 13.5 $mW \cdot cm^{-3}$ for the Zn device with the hexagram configuration, which ranked among the best performing hybrid TEPG/galvanic systems reported in the recent literature (figure 3.2.7-d and figure 3.2.8).

Galvanostatic discharge measurements were conducted at varying constant currents to further evaluate the performance of this device, as shown in figure 3.2.7-e. Results reveal that the energy generated from a single 30-µL droplet was sustained at room temperature and ambient relative humidity for more than 20 and 25 min under constant current draws of 0.1 and 0.01 mA, respectively. Prolonged power output over significantly extended discharge time was demonstrated here by continuously dropping the aqueous alum solution at a rate of 0.04 $mL.h^{-1}$, which produced a constant voltage around 1 V for 16 hours under a 0.01 mA current draw, as depicted in figure 3.2.7-f. Interestingly, the device continued generating about 0.4 V at the same current draw of 0.01 mA even after the alum solution feed had stopped, maintaining the same power output for nearly 3 days until the end of data recording (figure 3.2.8-a). This observation indicated that the device could harvest moisture from its surrounding environment to generate electricity continuously even after the evaporation of the electrolyte solution. Besides the obvious difference between moisture

and liquid-state harvesting, the reduced energy output may also be explained by the surface passivation of the electrode through the formation of ZnO or the degradation of the electrode. Furthermore, the continuous dropping system could sustain a voltage higher than 0.6 V over the same 16-hour period when the aqueous alum electrolyte solution was replaced by rainwater collected on the UW campus and after the generator had been primed with a single 30-µL alum droplet (figure 3.2.8-b).

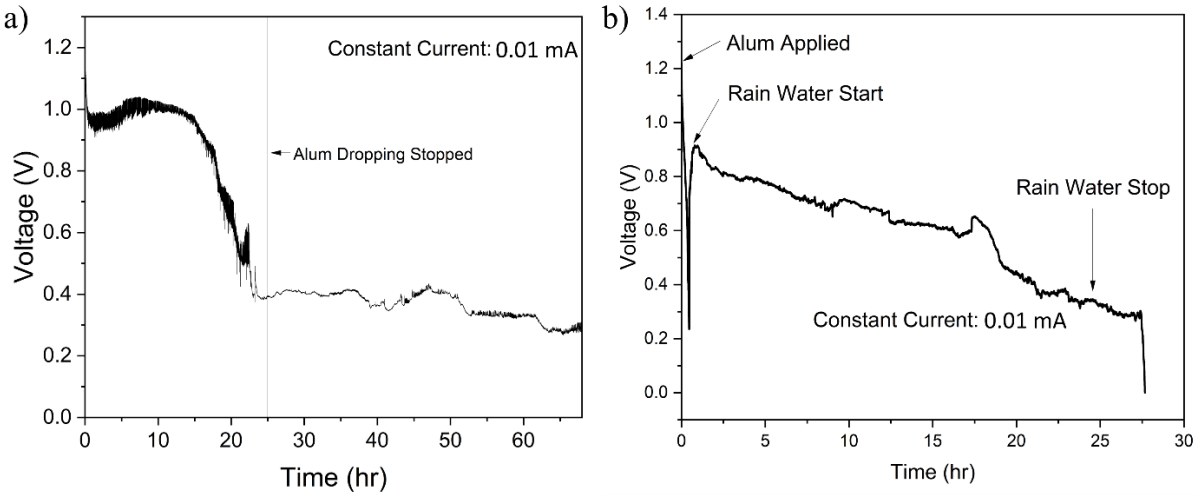

Figure 3.2.8 Galvanostatic discharge with constant current of 10 µA and 0.04 mL/hr alum dropping rate.

3.2.5 Practical Applications and End of Life Considerations

The energy harvested from the paper-based generator can be easily scaled by connecting multiple devices together. Figure 3.2.10-a illustrates the multiplicative behavior observed when connecting multiple power sources in series and parallel configurations, respectively yielding a proportional increase in voltage and current without any loss. To highlight the practical application of this energy generation system, a white LED was successfully lit for 30 min by applying 30 µL of aqueous alum solution onto each of the nine devices connected in a 3x3 circuit (figure 3.2.10-b).

Property.	This work.	Zhang et al.
V_{OC} (V)	1	0.5
I_{SC} (mA)	3.4	1.3
P_{MTP} (mW)	3.4	0.65
Volume (cm^3)	0.251	1.6
Spec. P_{MTP} (mW/cm^3)	13.5	0.41
P_{max} (μW)	690	216
Spec. P_{max}($\mu W/cm^3$)	2750	135

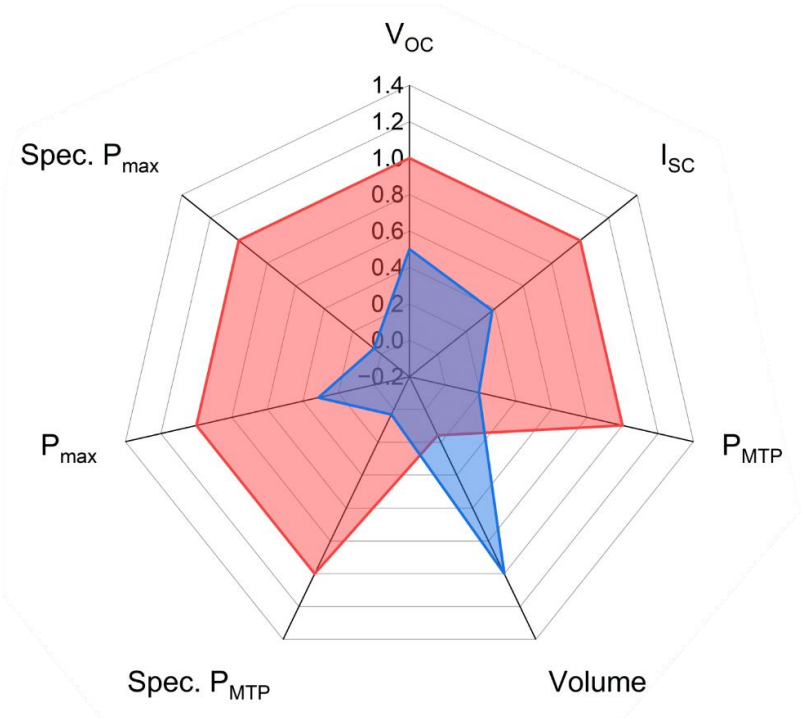

Figure 3.2.9 Spider plot comparing electrochemically enhanced TEPG to similar electrochemically enhanced device using copper electrodes developed by Zhang et al [111] with data tabulated above. Data shown in the radar plot is normalized between 0 and 1.

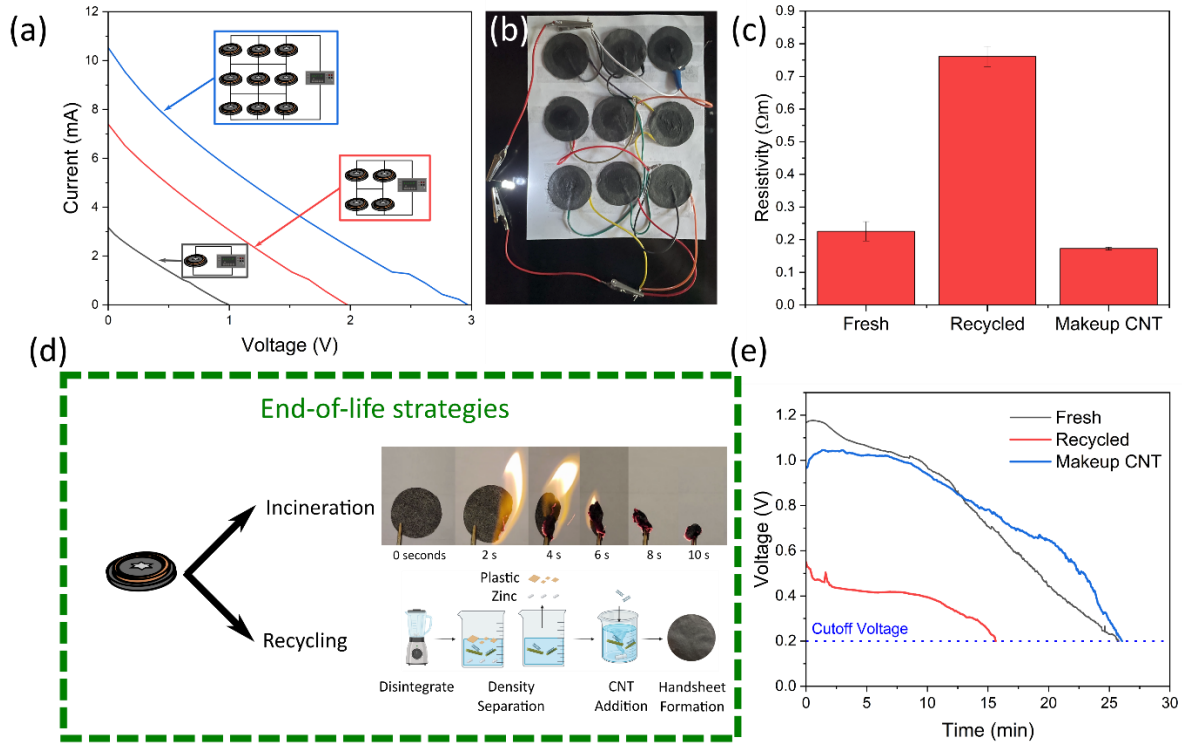

Figure 3.2.10 (a) Schematic of series and parallel TEPG connections (left) and linear voltammograms of multiple devices in series and parallel (right). Note: 3 x 3 means 3 set of 3-parallel-devices connected in series for a total of 9 devices. (b) Image of a blue 2.4 V LED being lit by a 3 x 3 matrix of TEPG devices (left) and the voltage of this matrix measured by a voltmeter (right). (c) Resistivity vs times TEPG devices were recycled (top) and the performance of a recycled sample with additional makeup CNT added vs. a fresh TEPG sample (bottom).

Paper recycling was successfully demonstrated in Figure 3.2.10-d as an end-of-life option to recover the paper (*i.e.* pulp fibers and additives) from the rest of the device. Here, spent generators were suspended in DI water and disintegrated using a conventional blender before separating the plastic and metal components from the pulp mixture by a simple sedimentation process. The recovered pulp slurry was then used to make recycled paper handsheets based on the TAPPI T205 standard procedure [90]. To make up for conductivity losses make-up CNTs were added to replenish those lost during the recycling process recuperating the lost conductivity as shown in figure 3.2.10-c. Additionally, by replenishing lost CNTs energy performance was regained as well

as displayed in figure 3.2.10-e. Another end-of-life option consists of incinerating the carbonaceous components of the generators after stripping them off their metal electrodes. This simple disposability approach is depicted in Figure 3.2.10-d, with time-lapse pictures showing a representative spent paper being turned into ash within 10 s after ignition. These methods offer a path to low-impact electronics that are sustainable alternatives to conventional energy harvesting devices.

3.3 Conclusions

In this study smart paper was investigated for application as a TEPG, finding competitive performance compared to many MEGs and TEPGs. With a MTP of 55 μW the TEPG in this study performed well showing both material and device design are integral to optimization of such devices. Additionally, through electrochemical enhancement, TEPG power output can be amplified and compete with the highest TEPG power output device currently produced in the literature (see figure 3.2.9) [46]. While the power produced by this device is competitive, passivation and corrosion of the electrolyte lead to poor application for long term sustainable power generation. Although this device may be ideal for applications needing a short-term power supply, further investigation into smart paper modification and device design may lead to a rechargeable electrochemically enhanced device that could produce overall net energy. Further study of this device may lead to a coupling of TEPG phenomena with well-defined electrochemical mechanisms to produce a new type of power storage, and perhaps even a new kind of sustainable generator. Despite these disadvantages the quick response to wetting and high-power output of the device proved exceptional when applied to light an LED further advancing towards a self-powered autonomous leak detection system, however power limitations still prevent the device from achieving wireless alerts. The following section will aim to advance zinc anode technology

towards zinc ion battery advancement and a sustainable approach to a novel form of leak detection as discussed in section 1.4.2.

4 Paper Based Zinc Anode for Zinc Ion Battery Advancement

4.1 Background

Lithium ion batteries have dominated the battery market since their advent in the 1990's because of their high energy density and cycling lifespan [127], [128], but there are concerns about their safety [129], [130], limited lithium supply, and environmental/socio-economic impact [127], [128], [129]. To improve upon these drawbacks researchers have been investigating alternative mobile ion batteries such as sodium, potassium, and zinc ion batteries [131], [132], [133]. These batteries solve many of the problems of lithium mining since they are inexpensive and abundant, however the activity of sodium and potassium pose safety concerns due to their explosive reactivity with water. Zinc ion batteries (ZIBs) have become a promising alternative because of the high valency of zinc, their high volumetric energy density (5855 mA h cm^3 compared to 2061 mA h cm^3 for Lithium ion batteries), safety, and low toxicity [70], [131], [134], [135], [136]. Additionally, ZIBs are ideal for the recent advances in fast charging electronics, since the high ionic conductivity of their aqueous electrolytes allow for rapid ion transport [134], [137]. These batteries are a type of mobile ion battery that operates in a similar manner to lithium-ion batteries. In short zinc ions are formed by oxidation at the anode (usually zinc foil) which then transport to the cathode and diffuse to its surface where they finally intercalate into the cathode and reduce to form a zinc-metal-oxide complex. During recharging the process flips and the positive terminal becomes the anode and zinc ions are liberated from the metal oxide cathode by oxidation reactions, facilitating ion transport back to the zinc foil where they are reduced to solid zinc [70], [131].

Although ZIBs show promise as a lithium-ion battery replacement they are known to suffer from anode and cathode side reactions leading to degradation of capacity by formation of unreactive oxide layers and poor coulombic efficiency [138], [139], [140]. Zinc ions coordinate with six water molecules and can act as a catalyst for hydrogen evolution reactions [75], [141]. These reactions can then produce hydroxide ions which react with zinc leading to the formation of a zinc oxide layer, passivating the surface. These reactions can also cause non-homogeneous nucleation sites to form resulting in sharp dendritic structure and short circuiting. To alleviate these effects the electrolyte is chosen carefully to help prevent disadvantageous side reactions, the most common being $ZnCl_2$, $ZnSO_4$, and trifluoromethanesulfonate $Zn(CF_3SO_3)_2$ [62], [75], [141].

In addition to designing better electrolytes, the cathode material has been heavily investigated to improve battery capacity and cycling stability of ZIBs. Manganese oxide (MnO_2) is a commonly used cathode as it has a large theoretical capacity, favorable economics, is highly abundant, non-toxic, and contains several stable valence states [73], [74], [142]. The cathodes reduce zinc via the reactions shown in equation 4.1-1 and allow for a specific capacity up to 308 mAh/g (2 e^- transfer) each and if combined can theoretically achieve 616 mA/h (4 e^- transfer) , showing good promise for high capacity batteries [131], [141].

Equation 4.1-1 Manganese oxide reduction of Zn ions.

$$Mn^{4+}O_2 + Zn^{2+} + 2e^- \rightarrow ZnMn_2{}^{3+}O_4$$

$$ZnMn_2{}^{3+}O_4 + Zn^{2+} + 2e^- \rightarrow 2ZnMn^{2+}O_2$$

Another cathode materials that has been investigate with much success is vanadium hydroxide (VOH) [61], [62], [63], [64], [65], [66], [67], [68], [69], [70]. VOH has many advantages due to its theoretical capacity of 589 mAh/g (2e^- transfer) in addition to its multiple valence states and

ease of change to its polyhedron V-O structure allowing for modification and optimization [62], [70]. For example, Jia et al. recently improved the cycling stability of ZIBs by pre-intercalation of VOH with trimethylphenylammonium cations, resulting in an increase in interstitial spacing, higher V^{4+} content and overall improved performance achieving a capacity of 451 mAh/g with great cycling stability and charge transfer kinetics.

While great advancements have been made to improve the cathode materials, dendrite formation at the zinc foil anode remains a primary problem for zinc ion batteries and leads to reduced capacity, coulombic efficiency, and can destroy the battery [141], [143]. Three strategies have been widely applied in attempts to alleviated dendrite formation and retain battery capacity for thousands of cycles including: modification of the electrolyte to reduce zinc-water coordination, incorporation of controlled nucleation sites to encourage uniform zinc deposition, and homogenizing of the electric field through 3-D structured anode materials [75], [131], [141]. By changing electrolyte composition it is possible to reduce H_2O coordination reducing hydrogen evolution side reactions which in turn lead to less OH^- and ZnO formation, reducing the passivation of the anode surface [141], [144], [145]. By causing controlled zinc deposition, uniform zinc nucleation is possible which prevents conical dendrites from forming [141], [146], [147], [148]. While these first two mitigation strategies are practical and effective, one of the most effective methods is the use of 3-D structures to create a uniform electric field. The kinetics of dendrite formation have been heavily studied and can be described by equation 4.1-2, where τ is the dendrite formation time, D the ion diffusivity, C_0 the initial concentration, e electron charge, μ_a/μ_c the anionic/cationic mobility, and J the current density [141], [144], [145].

Equation 4.1-2 Dendrite formation time..

$$\tau = \pi D \frac{eC_0(\mu_a+\mu_c)^2}{2J\mu_a}$$

From equation 4.1-2 it is evident that by decreasing the current density the dendrite formation time will be increased, reducing the rate of dendrite formation [141], [149], [150]. Using 3-D structures it is possible to achieve a large increase in specific surface area, homogenizing the electric field [134], [135], [141], [151]. For example Kang et al. were able to achieve a stable capacity of roughly 200 mAh/g with near 100% coulombic efficiency for 300 cycles by electrodeposition of zinc onto a porous copper scaffold [151]. Several studies have also investigated carbon nanotubes as a scaffold to provide mechanical reinforcement, flexibility, and fast charge transport to the active material [135], [152], [153]. For example, Wang et al. achieved dendrite free ZIBs with minimal loss of capacity after 1000 cycles via the retention of zinc microspheres in a nano-fibrillated cellulose/carbon nanotube composite using a vacuum filtration method [134]. Furthermore they were able to create a flexible multi-ply ZIB by wet pressing anode, separator, and cathode together, creating a completely integrated ZIB without the need of a coin cell configuration [134]. By combining these principles with the papermaking principles applied by Goodman et al. it was hypothesize to be able to produce a scalable papermaking based process for producing a new type of zinc anode [34], [35].

In this study bleached softwood cellulose fibers were used as a matrix of reinforcement to retain a zinc microsphere/CNT composite for an improved, dendrite-free zinc anode employing 3-D structured anode concepts. The following section presents these findings and assesses the fibrous zinc anodes' performance in a zinc ion battery using a vanadium hydroxide cathode provided by Dr. Xiaoxiao Jia and the Professor Guozhong Cao Research Group in the Materials Science and Engineering Department at the University of Washington [62].

4.2 Results and discussion

4.2.1 Zinc microspheres as MWCNT-OH dispersant

To create a fibrous zinc anode with ease of scalability a papermaking process was intended for anode synthesis. In pursuit of this idea, it was necessary to create an additive to be easily incorporated into current paper making technology when developing the synthetic method. The papermaking industry currently employs fillers such as calcium carbonate, titanium dioxide, and kaolin clay to achieve various properties [92], [154], [155], [156], [157]. The retention of these materials and their incorporation into a fibrous paper sheet is highly dependent on the fillers' colloidal properties and requires well dispersed solids. In this study the intended fillers were zinc particles and CNTs, and CNTs are known for being very difficult to disperse with many studies investigating mechanisms to improve their stability through oxidation [158], [159], surfactants [36], [160], and inorganic particles [161], [162]. In this section the zinc microspheres were employed as a dispersant for CNTs and evaluated by their changes in morphology by incorporation of the zinc microspheres and ultrasonication.

Figure 1a shows images of the different dispersions of carbon nanotubes, zinc microspheres, 8:1 mixture of Zinc/CNT, and the sonicated mixture from left to right respectively. Originally the carbon nanotubes formed large bundles not dispersing well, however the zinc particles formed a uniform gray solution under constant agitation. Figure 4.2.1 shows the particle size distributions of the zinc powder, and the powder dispersed in water showing a shift from a median particle diameter of ~2.5 μm to 4.7 μm with a much broader distribution, likely caused by aggregation in solution. The difference in size distribution was found to be significant by the two-tailed t-test assuming equal variances and a 95% confidence ($p\text{-value} << 0.05$). It should be noted by the reader that once agitation was stopped the particles would quickly settle out of solution due to their large density and particle size. After the addition of CNTs to the solution the dispersion would only partially settle, and a much more uniform and dispersed solution was achieved

indicating a degree of CNT de-bundling and stabilization simply by the incorporation of the zinc particles. After just 2 minutes of sonication the solution became uniform and vicious, stabilizing and remaining dispersed long enough to produce the fibrous anodes (figure 4.2.2-a).

Table 4.1 Quantitative statistics of Zn/CNT size distributions.

	CNT Control	Zn Control	Zn/CNT Dispersion	Zn/CNT Dispersion Sonicated
Mean diameter (μm)	18.3	4.4	7.6	7.6
Median (μm)	15.5	4.3	6.5	6.2
Sample Standard Deviation (μm)	14.1	2	6.9	7.3

Figure 4.4.2-b displays optical micrographs of each sample with measured size distribution histograms inset in the images. Relative frequency gaussian fitted distributions of the samples and their spatial variabilities are shown in figures 4.4.2-d and e respectively. Originally the CNT particles were very big with a large spatial variability and broad size distribution with a mean particle size of 18.3 um and standard deviation of 14.1 μm (table 4.1). On the other hand, zinc microspheres had a uniform distribution with much less spatial variation and a mean particle size of 4.3 μm. By combining the two at an 8:1 zinc to CNT ratio the particle size of the CNTs were reduced to 7.6 μm having even less spatial variability than the original zinc powders. By ultrasonicating the mixture for two minutes the particle size and distribution were not significantly changed within 95% confidence (two sample t-test, equal variances, $p = 0.78$) with a particle size of 7.6 μm, however based on experimental observations there was still a large impact on the dispersion quality which can be seen by darkening of the solution as shown in figure 4.2.2-a. To

investigate this mechanism, SEM and UV-vis spectroscopy were utilized further assess dispersion quality.

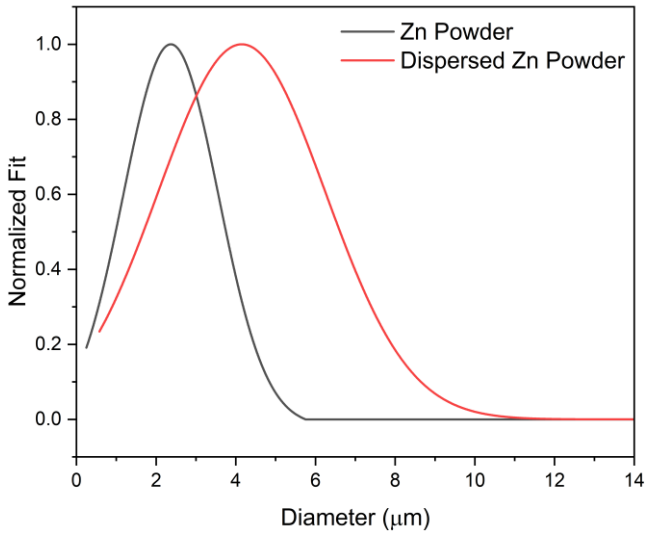

Figure 4.2.1 Particle size distribution of 100 mesh zinc powder and the zinc powder dispersed in water determined by optical microscopy and particle image analysis.

UV-vis measurements of the solutions at 350 nm are displayed in figure 4.2.2-f to qualitatively compare the quality of CNT dispersions. CNT's are known to have characteristic absorption bands in the 300 – 1200 nm region which disappear when aggregated due to quenching [36], [163], [164]. From UV-vis measurements it was apparent that the absorption drastically increased with both the Zn/CNT mixture and even more so with sonication. This indicated better individualization of CNTs which can be observed from SEM images shown in figure 4.2.2-c. Initially the CNT powders were heavily aggregated and by simply mixing the CNTs with Zn microspheres, the spherical zinc particles were well incorporated with the CNTs starting to break up these carbonaceous structures. Upon sonication the CNTs were de-bundled, creating a highly amorphous and webbed matrix in solution. These results suggested a unique interaction between

the zinc particles and MWCNT-OH at the hydrophobic/hydrophilic interface. CNTs are known to aggregate because of Van Der Waals forces and pi-pi interactions [36], [165] and ultrasonication is able to break down these interactions and allow for dispersants to prevent reaggregation and stabilize CNTs [36]. Xu et al and Kukobat showed that by having a material that can adsorb to the CNT surface and then create a hydrophilic ionic layer a stable CNT dispersion may be achieved in aqueous solutions [160], [161]. Zinc is known to tarnish in oxygen and water environments and form a protective oxide layer making it a great metal for applications in areas where rust is a concern. This oxide layer can create beneficial hydrophobic interaction with the CNTs and then stabilize through ionic layers capable of hydrophilic interaction, thus creating a stable MWCNT-OH/zinc microsphere dispersion. Evidence of this type of interaction has been displayed by Kukobat et al. where a Zn/Al based complex was developed to create a metallic structure capable of hydrophobic and hydrophilic interactions allowing for stable single walled CNT dispersions and the same mechanisms is likely responsible for the dispersibility of CNTs displayed in this study.

In this section it was shown that zinc microspheres can create monodisperse solutions ideal for fibrous zinc anode synthesis. By taking advantage of the self-passivating nature of zinc to create a hydrophobic protective layer a strong zinc-CNT interaction was possible creating a stable hydrophilic interface. Through the development of this suspension the Zinc/CNT slurry was easily applied as a paper additive for paper making processes.

4.2.2 Fibrous anode morphology

A simple paper handsheet preparation method was able to be applied due to the preparation of Zn/CNT solution, figure 4.2.3-a shows a schematic of this procedure. To prepare the handsheets a slurry was prepared, diluted, and dewatered through a fine mesh screen designed to allow fast

passage of water while retaining cellulose fibers (essential for manufacturing at scale). The primary difficulty in this process was the retention of the nano and micro particles which can easily pass through the screen during the paper making process. This is a well-known and handled disadvantage in the paper making industry often encountered in the retention of inorganic fillers such as calcium carbonate [93], [154]. A method that has shown to be particularly effective is pre-flocculation, where anionic particles are flocculated before being added to the cellulose pulp slurry [92], [93]. In this study cationic starch was used to neutralize negative charge on the surface of the particles and mechanically flocculate smaller particles into larger flocs that were then able to be retained in the fiber mat as if formed on the screen. Several concentrations of cationic starch were tested similar to the ranges reported by Chauhan et al. [91] however at too high of a concentration the anode was too sticky to be properly removed from the screen, thus the optimal retention of ~75-80 wt% was achieved with a mass loading of 0.1 wt% cationic starch. Using the optimal retention chemistry fibrous anodes were produced with good dispersion quality, retaining much of the zinc creating a favorable structure for homogenous zinc anodes.

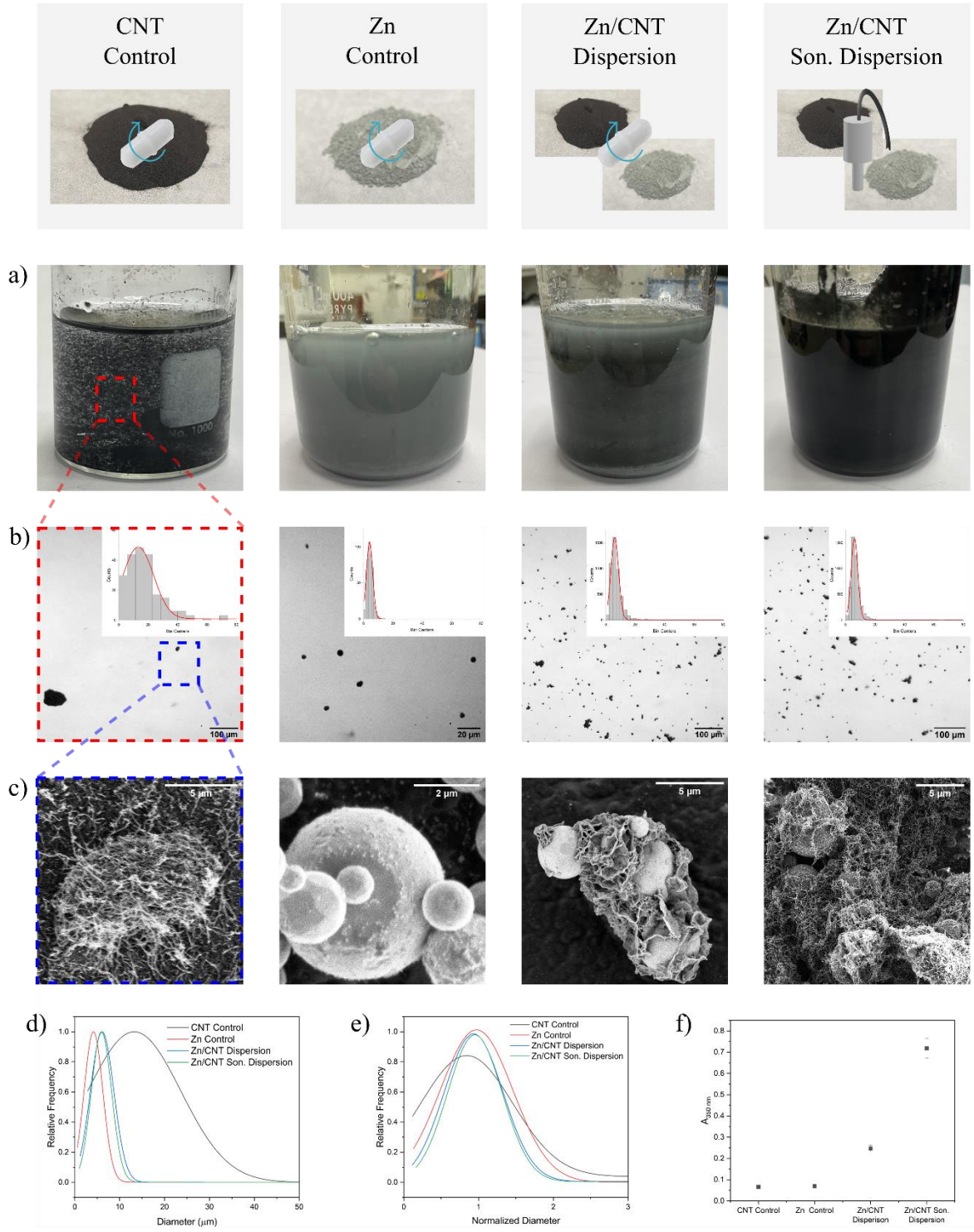

Figure 4.2.2. (a) Images of solutions prepared for characterization of zinc microsphere/MWCNT-OH dispersions. (b) Optical micrographs of solutions with fitted histogram of particle size measured by Image-J

software inset. (c) SEM micrographs, (d) fitted particle size distributions, (e) spatial variation of size distributions, and (f) UV vis absorption at 350 nm of prepared dispersions.

Table 4.2 Physical characteristics of fibrous anodes at varying experimental conditions.

Experiment	Retention (wt%)	Caliper (mm)	Density (g/cm^3)	Sheet Resistivity ($\Omega \cdot m$)
10% Cell.	81.8 ± 4.4*	0.21 ± 0.02	1.17 ± 0.07	6.1 ± 0.4
20% Cell.	80.6 ± 3.2	0.14 ± 0.01	0.86 ± 0.04	21.5 ± 0.9
30% Cell.	74.9 ± 2.7	0.10 ± 0.01	0.72 ± 0.01	78.2 ± 5.0
10% Calendared	81.8 ± 4.4	0.11 ± 0.01	2.26 ± 0.14	5.8 ± 0.3

* Averages shown with 95% Confidence interval

While the Zn/CNT ratio has already been investigated in similar materials by Wang et al. [134], cellulose concentration has not been thoroughly investigated for its contribution to electrochemical properties. In this study fibrous anodes were prepared by maintaining a constant mass of 0.6 g of cellulose (minimum required for handsheet formation determined experimentally) while adding varying masses of Zn/CNT slurry to achieve the desired cellulose loading. Although much less mass was added at 20 and 30 wt% cellulose loadings table 4.2 shows that retention was not significantly impacted, indicating fast formation of the fibrous mat to aid in retention of smaller particles. Caliper and density measurements shown in table 4.2 display significant densification of the fibrous anode with decreasing cellulose content reaching a density of 1.17 g/cm^3 at 10 wt% cellulose. Further densification was achieved by calendaring the paper in which the paper was pressed between two steel drums with a pressure of 4000 psi. With the 10% cellulose fibrous anode calendared a density of 2.26 g/cm^3 was achieved, still much lower than that of zinc metal (7.14 g/cm^3). Additionally, table 4.2 shows a decrease in resistivity with decreasing cellulose content.

Furthermore, calendaring significantly decreased caliper by 53 % under 4000 psi of pressure with no significant change to the sheet resistivity, however measuring the resistance through the thickness of the paper a decrease was observed from 0.78 ± 0.29 Ω to 0.31 ± 0.02 (t-test p-value 1.1E-8). These results indicate an increase in conductivity through densification of the paper without significant modification to the conductive nature of the surface. However, the surface became very smooth having a shiny finish characteristic of many filled and calendared paper grades. These characteristics may be further investigated by analyzing the morphology and structure of the materials

Figure 4.2.3-b shows SEM imaging of the surface of the 10 wt% samples showing well dispersed zinc particles interspersed with flocks of CNTs that create a well intertwined structure. Imaging from SEM show Zn particles only partially covered with CNTs likely due to their interactions as a dispersant. Zinc was able to create hydrophobic interactions with the carbon nanotubes and form a hydrophilic layer of ions allowing it to disperse the CNTs as previously discussed. This would explain its partially covered morphology as portions of the large spheres would need to be exposed to water and residual water in the matrix after the dewatering step would prevent CNTs from fully covering zinc during filtration and drying. Additionally, the much larger concentration of zinc compared to CNTs likely influenced this behavior as well since there was simply less CNT's available to form on the zinc surface. Figure 4.2.4 shows cryofractured cross sections of cellulose concentrations of 10% (a), 20% (b), 30% (c), and 10% calendared (d) samples. From these figures it is evident that in all cases zinc and carbon nanotubes are well retained through the thickness and with more cellulose more surface charging occurs as expected with decreasing conductivity. Additionally, with calendaring particles maintained their spherical structure through the thickness and minimal changes happened aside from densification of the fibrous structure.

Figure 4.2.5 shows the surface of the 10% cellulose sample before (a) and after (b) calendaring. The surface was originally quite rough, and fibers could be easily distinguished from Zn/CNT flocs. After pressing the surface become much smoother appearing to have flattened the zinc and filed gaps creating a very smooth surface. This was also observed from the inset images showing a dark dull surface before calendaring vs a smooth and high gloss finish after. These morphological changes can be interpreted in conjunction with spectroscopic data as well as strength properties to further understand changes to the materials with varying concentrations.

Figure 4.2.3-c shows the XRD spectra for the fibrous anode at varying cellulose concentrations, cellulose paper, CNT, zinc powder, and zinc database reference (#COD 9008524) [166]. The zinc powder spectrum matched well with the data base spectrum for purified zinc as expected. CNT's and cellulose had highly amorphous peaks with some crystalline peaks for the semicrystalline structure as expected of these materials. Furthermore, with the addition of cellulose at 10 wt% the spectrum remained consistent with that measured by the initial zinc powder. As the concentration of cellulose increased so did the amorphous peaks associated with cellulose, however in all cases zinc was the most abundant material and its crystalline peaks dominated the spectrum with only slight amorphous cellulose peaks appearing. These results are very important features of these anodes as a higher degree of crystallinity has been shown to improve cycling stability for anodes in studies of lithium-ion batteries [167]. Figure 4.2.3-d shows the cellulose concentration effects on the anode stress strain curves and Figure 4.2.6 shows quantitative data extracted from the curves. In general, as the cellulose content was increased all strength properties of the fibrous anode also increased. Again, this behavior was expected as cellulose creates strong OH bonds while the fillers were expected to bond primarily by weak Van Der Walls forces [34], [35], [168], [169].

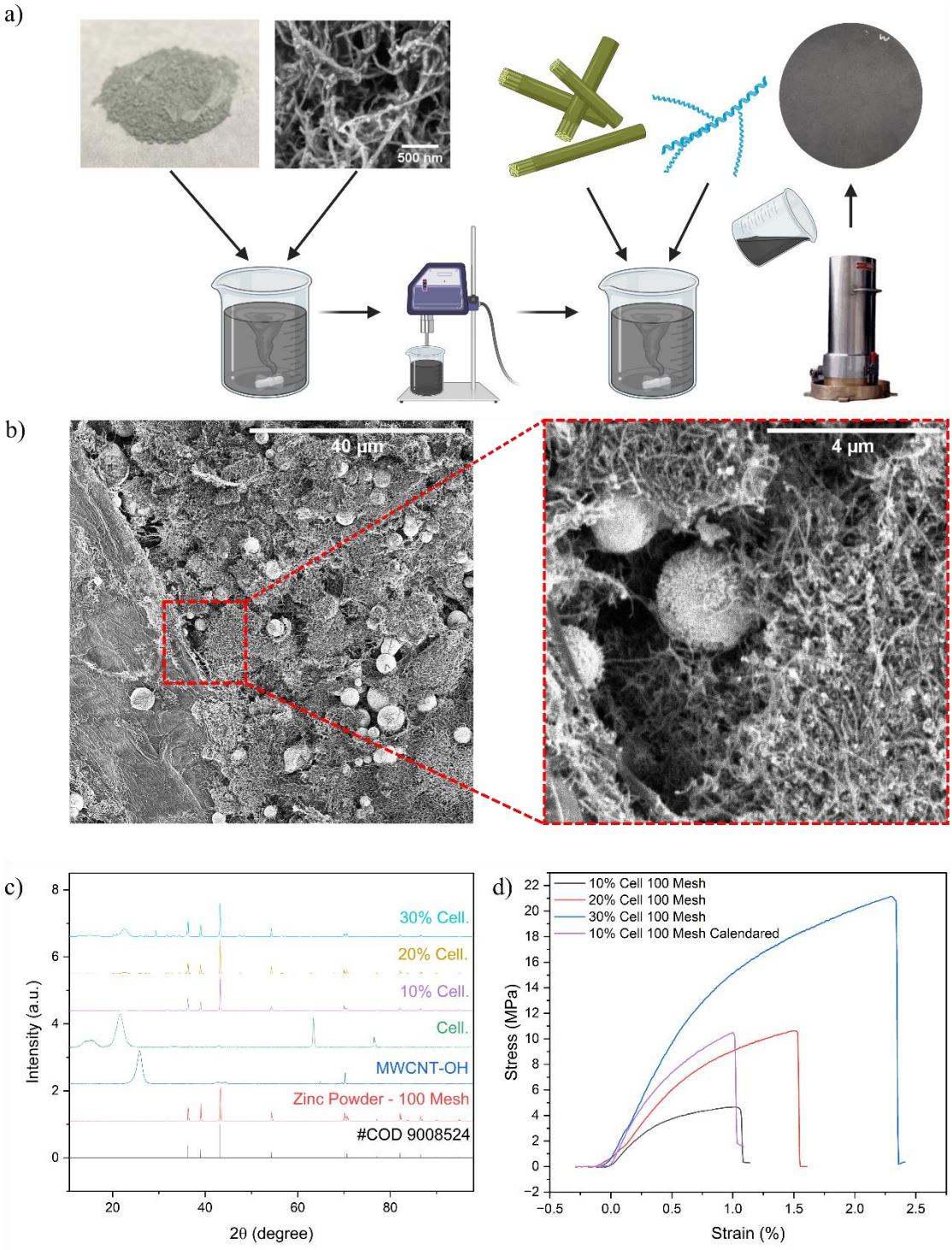

Figure 4.2.3. (a) Schematic of synthetic methods for production of fibrous zinc anode. (b) SEM images of 10% cellulose anode. (c) XRD spectra of varying concentrations of cellulose, MWCNT-OH, zinc powder, and zinc data from crystallography open database (#COD 9008524) [166]. (d) Stress Strain curve of varying cellulose concentrate and calendared sample at 10% cellulose.

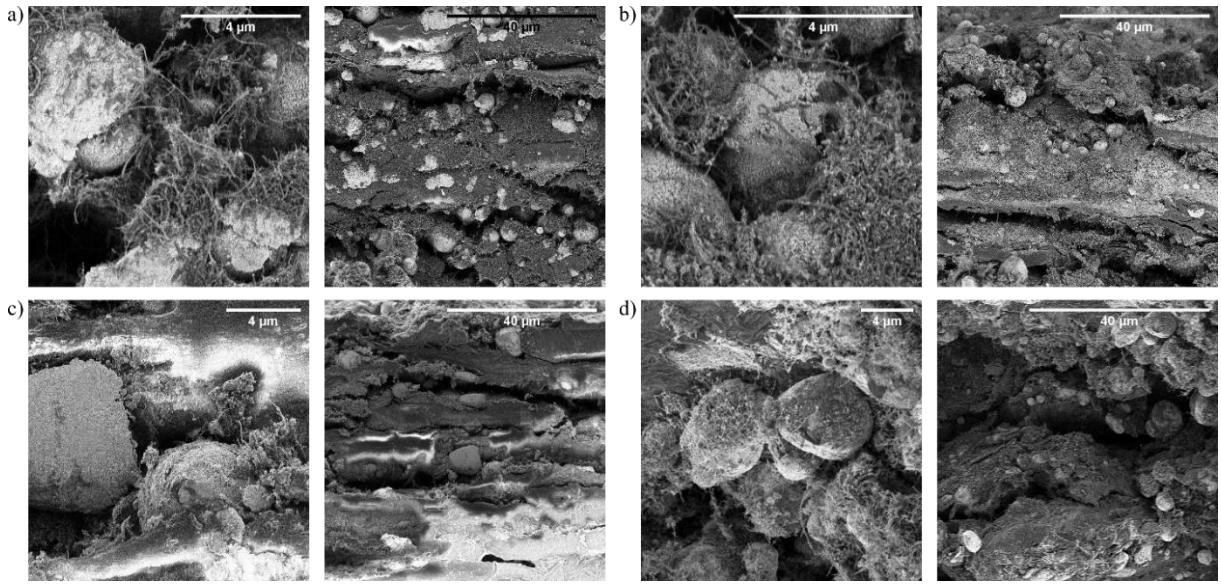

Figure 4.2.4 Sem imaging of the cross section of (a) 10%, (b) 20%, (c) 30%, and calendared 10% cellulose fibrous anodes.

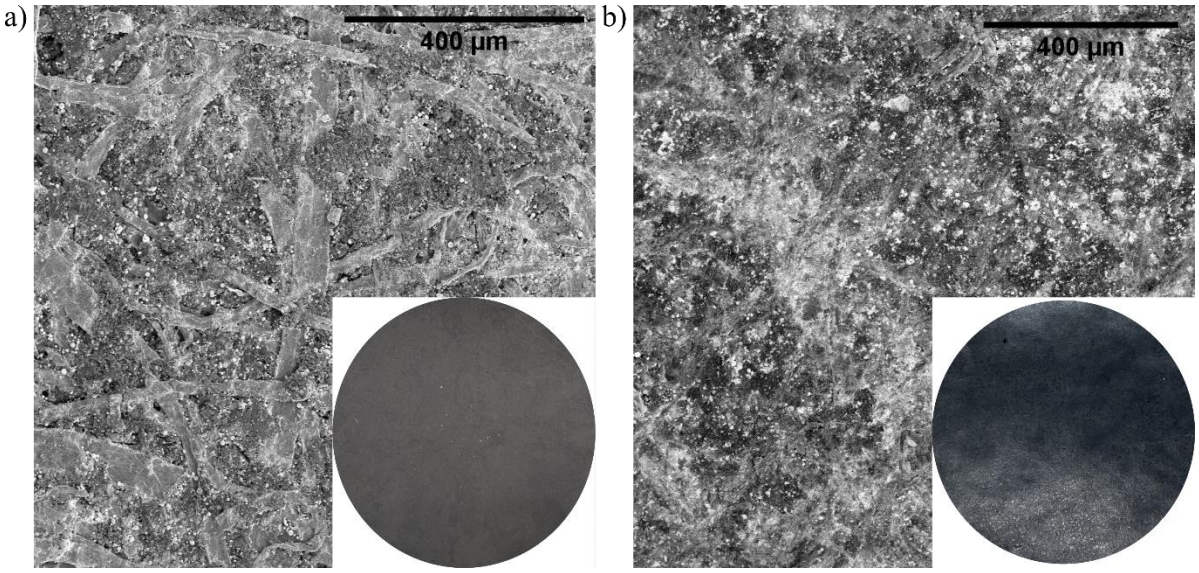

Figure 4.2.5 10% cellulose fibrous anode (a) before and (b) after calendaring

Additionally, by calendaring the 10 wt% cellulose anode the densification of the material led to the increase of tensile properties seeing an increase in elastic modulus and ultimate stress, however this was an artifact of normalization by cross section and the actual strength was not significantly

changed as shown by the tensile index. A typical response in calendaring of paper would be an increase in OH bonding [154], [156], [157], however the results presented here imply that calendaring did not increase OH bonding but only densified the material. This indicates that cellulose fibers were likely not well connected in the sample but are instead interspersed with Zn/CNT flocs. While these results indicate good dispersion and formation of the material preliminary testing indicating a two sidedness in the material which was further investigated.

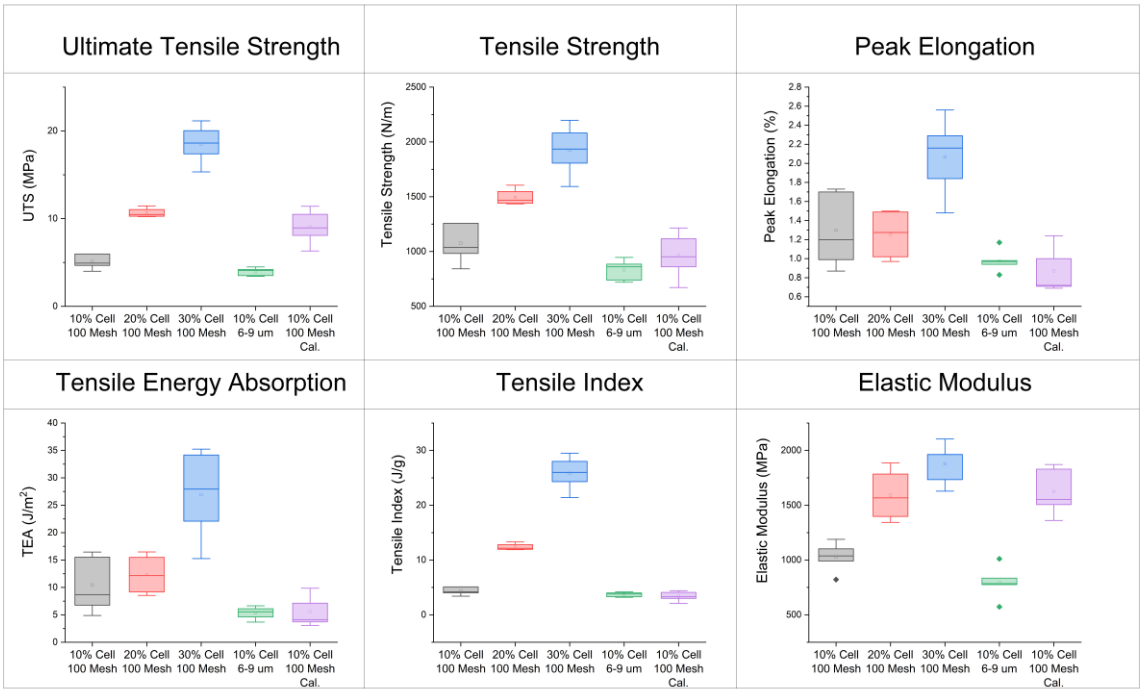

Figure 4.2.6 Quantitative analysis of stress strain curve results of fibrous zinc anodes.

Figure 4.2.7 elucidates the two-sidedness observed showing SEM micrographs of the surface in contact with the wire during synthesis (a), the opposite side (referred to as the blotter side) (b), and the cross section (c) of 10% cellulose anodes. The SEM images show a porous structure with a mix of light and dark spots with both samples imaged at a 9.6 m working distance

with electron beam operation at 2 kV and 13pA using an Evergart-Thornley detector (ETD) which senses secondary and backscatter electrons. This detector will show a brighter image for larger atomic number molecules such as zinc since there will be a greater number of scattered electrons caused by elastic collisions [170]. The blotter side (4.2.7-b) shows a much less porous surface, with more bright areas likely caused by a higher zinc content at the surface. Additionally, the cross section shown in figure 4.2.7-c shows a gradient of zinc through the material thickness with more zinc appearing at the blotter side. This was further confirmed by qualitative analysis by laser ablation mass spectroscopy (LA-MS) experiments shown in figure 4.2.7-d. By comparing an indium doped fibrous anode with an indium doped blank consisting of paper with an equivalent CNT content to the fibrous anodes, Zn isotope 64 present in gases (counts per second) of the ablated material could be detected. These results show a clear and significant (t-test assuming equal variances p-value = 5.5E-4) difference in intensity from zinc particles when measuring between the two surfaces with 95 % confidence. Additionally, the variation across the sample surface was much larger for the blotter side compared to the wire side indicating worse uniformity of zinc particles across the surface. This difference was further verified by fitting gaussian distributions of histograms of Zn/In counts detected for the blotter vs wire side (figure 4.2.8). In this figure the blotter side can be seen to have a much broader distribution (FWHM = 104) compared to the wire side (FWHM = 29) further displaying less homogenous surface.

During industrial paper formation a fibrous mat is formed on a mesh screen which helps to retain very small cellulose particles called fines and as the matt is formed retention of the fines is improved [154], [156]. Similarly, during synthesis of the fibrous anode cellulose fibers and Zn/CNT flocs formed a mat on the surface of the wire. However, before the mat was fully formed smaller particles and flocs were able to pass through the screen and as the mat continued to increase

in thickness, less material was lost. This mechanism would likely explain the two-sidedness observed in the fibrous anode and had important implications for the performance of the material for zinc ion batteries.

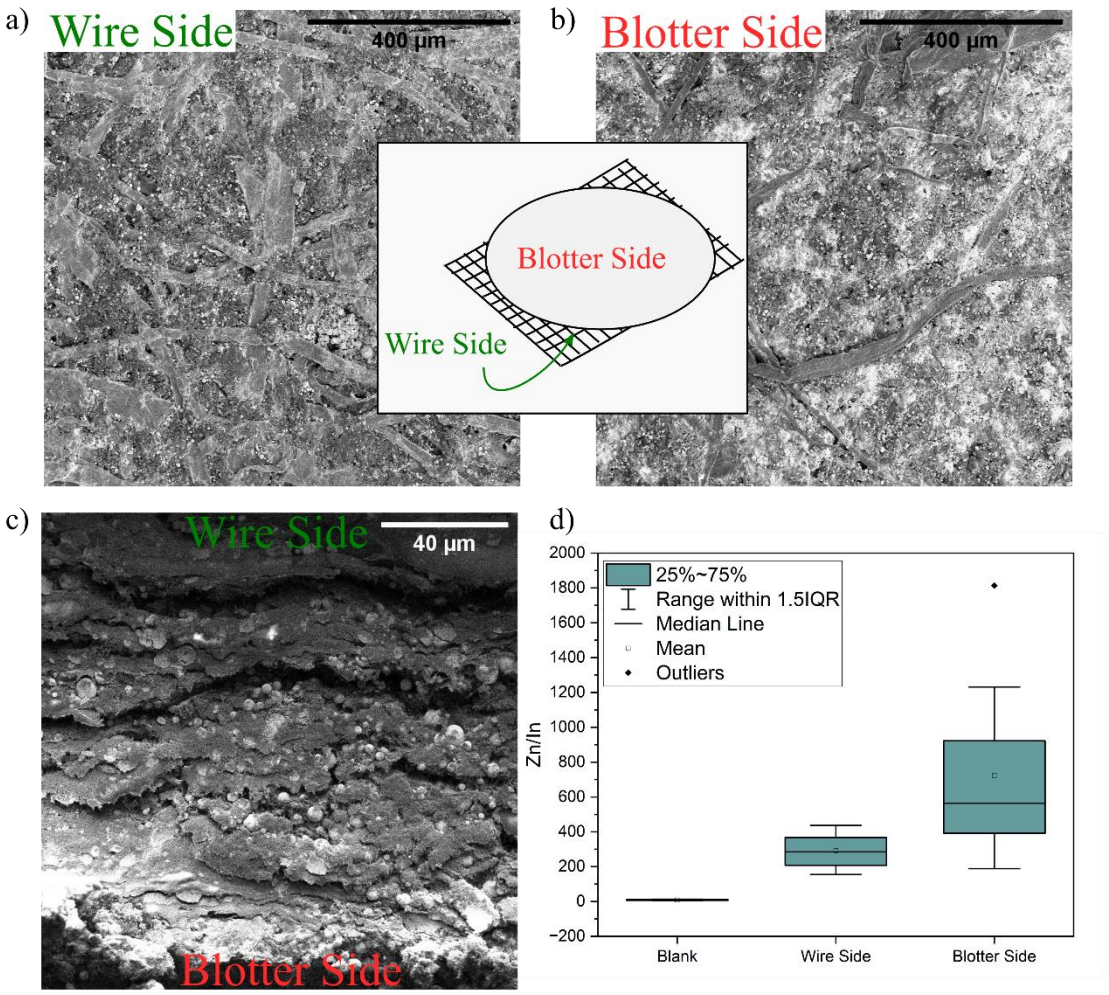

Figure 4.2.7. SEM micrograph of (a) wire side, (b) blotter side, and (c) cross-section of 10% cellulose anode. (d) Box and whisker plot of LA-MS results for carbon nanotube paper blank, blotter side, and wire side.

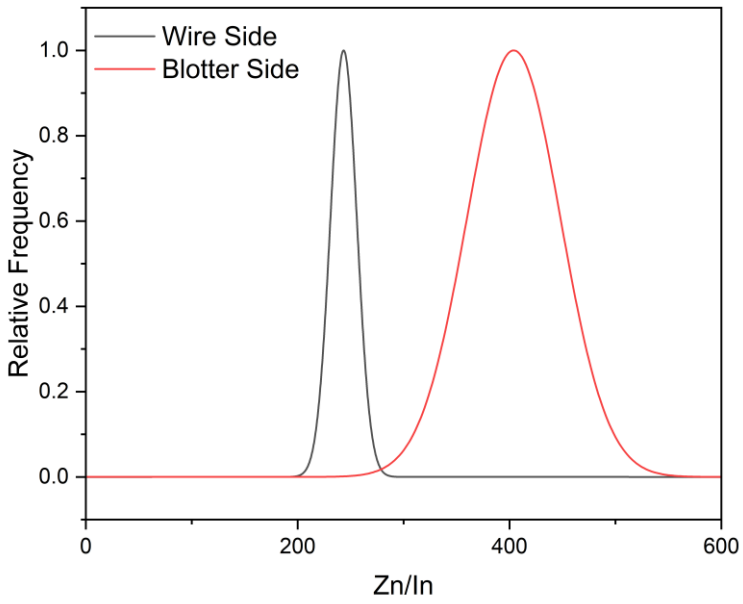

Figure 4.2.8 Normalize gaussian distribution showing the ratio of zinc/indium counts per second detected by the mass spectrometer for the wire and blotter sides of the fibrous anode.

The properties of the various fibrous anodes prepared in this study were shown to be highly dependent on the composition and method of manufacturing. These properties had major impacts on the performance of the fibrous anode for zinc ion battery systems. The following sections will investigate the performance of the anode in zinc ion batteries and investigate the mechanisms involved to better understand and improve ZIB lifespan.

4.2.3 Electrochemical Performance

Prepared fibrous zinc anodes were applied as a new anode material for zinc air batteries to improve their cycling stability through electric field homogenization to reduce dendrite formation. Currently ZIBs are evaluated by a zinc foil which was used as the control for comparison in this

study. In this section the advantages of the unique structure and morphology of the fibrous anode developed in this study will be explored for the enhancement of ZIB performance.

Fibrous anodes were evaluated by construction of CR2032 coin cell batteries and evaluated by galvanostatic charge/discharge cycling (GCD) analysis at different constant current densities. Figure 4.2.9-a shows the discharge specific capacity of the ZIBs with different anode compositions over 3000 cycles at a constant current of 4 A/g (specific capacity was normalized by the mass of cathode active material, VOH). The ZIB made with zinc foil initially had a lower capacity compared to the fibrous anode which increased over the first 200 cycles and then began to steadily decrease. This curve shape can be explained by activation of the zinc surface followed by surface passivation, dendrite formation, and inhomogeneity of plating/stripping reactions as cycling continues [70], [134], [150], [151]. The fibrous anode, on the other hand, showed varying degrees of performance that had a large dependency on the composition and coin cell configuration. Increasing concentration of cellulose drastically hindered battery performance which was expected due to the higher resistance and lower concentration of active material. However, what was surprising was the sudden drop to a capacity of zero experienced by 30% cellulose anode likely caused by a short circuit. Additionally, the configuration of fibrous anode was very important, as shown by the performance differences between samples having the wire side vs the blotter side facing the separator/cathode. When the wire side was facing the cathode a longer cycling lifespan was observed for all concentrations. As the blotter side had a lower porosity and much more zinc deposited at the surface more dendrites were able to form on the surface and there was no 3D structure to support electric field homogenization. With the wire side facing the separator less zinc was present on the surface and a higher degree of porosity was observed allowing ions to easily diffuse to the surface of zinc microspheres embedded throughout the structure of the anode.

According to equation 4.1-2 this can greatly reduce the dendrite formation time by both increasing the speed of diffusion as well as decreasing the electric field density. These results indicate the best performing sample to occur with 10 wt% cellulose with the wire side facing the separator (herein referred to as 10% cell. wire) with capacity retention after 3000 cycles increasing to 60% vs 55% for the zinc foil

Figure 4.2.9-b shows the average discharge voltage for each cycle displaying an overall higher voltage for the zinc foil compared to 10% cell wire likely caused by larger overpotentials in zinc. However, the average voltage stayed very consistent after 1000 cycles for the fibrous anode showing a stable material during cycling while the zinc foil continued to have a steady decrease. The effects of capacity retention and average voltage can be observed together in figure 4.2.9-c which shows the discharge specific energy in mWh/g and the specific energy normalized by that anode mass. At the end of 3000 cycles the two batteries had very similar discharge energy, however when normalized by the mass of the anode used the fibrous anode drastically outperformed, indicating less mass required for the same performance.

To further improve the anode by reducing internal resistance and IR drop, the fibrous anode was calendared. Figure 4.2.10-a shows the GCD curve of the first cycle and 4.2.10-b shows the capacity retention over 3000 cycles. From these results the IR drop was drastically decreased and the overpotential, evaluated by mid-point, was improved from 0.66 V to 0.49 V. The overpotential of the system can be estimated by comparing the voltage difference between the charge and discharge voltage at the midpoint of the curve [62]. However, during cycling the capacity retention was much worse than both the uncalendared sample and the zinc foil. By calendaring, the conductivity was increased reducing the overpotential, however the porosity was likely decreased and the hydrophobicity increased. These changes would cause the anode to behave more like a

zinc foil, losing the advantages of the 3D structure and decreasing the electrochemically active zinc surface area thus reducing performance.

Figure 4.2.9-d shows the first cycle of the anodes at 4 A/g showing a higher open circuit voltage 1.56 vs 1.50 V for the fibrous anode and zinc foil respectively. Additionally, a higher discharge capacity of 292 mAh/g vs 250 mAh/g for the fibrous anode compared to the zinc foil was observed. Both samples showed an initial voltage drop due to internal resistance followed by similar curves evident of voltage drops caused by overpotentials. The fibrous anode had a midpoint voltage difference of 0.66 V compared to 0.54 V for the zinc foil indicating a larger overpotential. This was expected due to the larger thickness of the anode (0.21 mm vs 0.1 mm for Fibrous anode and zinc foil respectively), 3D structure of the fibrous anode and lower conductivity (0.16 vs 1.7 x 10^7 for the fibrous anode and zinc respectively) [60], [171]. Figure 4.2.9-e shows the GCD curve of the 1st and 3000th cycle displaying an increase in activation overpotential observed by IR drop for the fibrous anode but no net change in overpotential evaluated by midpoint method. The zinc anode had a decrease in midpoint voltage difference from 0.54V to 0.48 V. However, the shape of the curve changed showing a sharp voltage drop off at the end of the cycle. On the other hand, the fibrous anode had a very similar shape to its initial curve indicating little to no change which may be explained by its porous structure allowing facile diffusion of zinc ions to the surface of the zinc microspheres imbedded in the structure. While the fibrous anode has been shown to have good characteristics for battery lifespan, many of its features are not advantageous for discharge kinetics which must be evaluated by rate performance.

Rate performance of the fibrous anode was evaluated by GCD conducted for 5 cycles at 5 different cycling rates (0.5, 1.0, 2.0, 4.0, and 8.0 A/g) shown in figure 4.2.9-f. A higher discharge specific capacity was observed for the different discharge rates for the zinc foil which had steady

horizontal slopes. For the fibrous anode a higher discharge capacity was initially observed at 0.5 A/g but steadily decreased with passing cycles until stabilizing at 10 cycles. Most likely the anode was initially very active due to its porosity, but as plating and stripping continued zinc began to intercalate into the CNT structure and deposited onto zinc surfaces closer to the more conductive blotter side leading to densification of the material and reducing accessibility of the electrolyte. Figures 4.2.9-g and -h show the first GCD curves at increasing discharge rates of the foil and fibrous anode respectively. A shifting of the bottom of the curve was observed for the fibrous anode compared to the foil which is indicative of greater concentration overpotentials. This can be explained by changes to the structures of the anodes over 3000 cycles which appear to happen very quickly for the fibrous anode. As the structure changes the mass transport properties at the solid electrolyte interface change creating higher mass transport limitations leading to the higher concentration overpotentials [146].

Overall, the favorable cycling performance and poor rate capabilities can be explained by fibrous structure and two sidedness of the anode. In the next section the morphological changes discussed will be investigated further to better understand the changes happening to the anode during cycling operations. Additionally, the anode will be characterized to assess the extent of dendrite formation and effectiveness of the 3-D structured anode material.

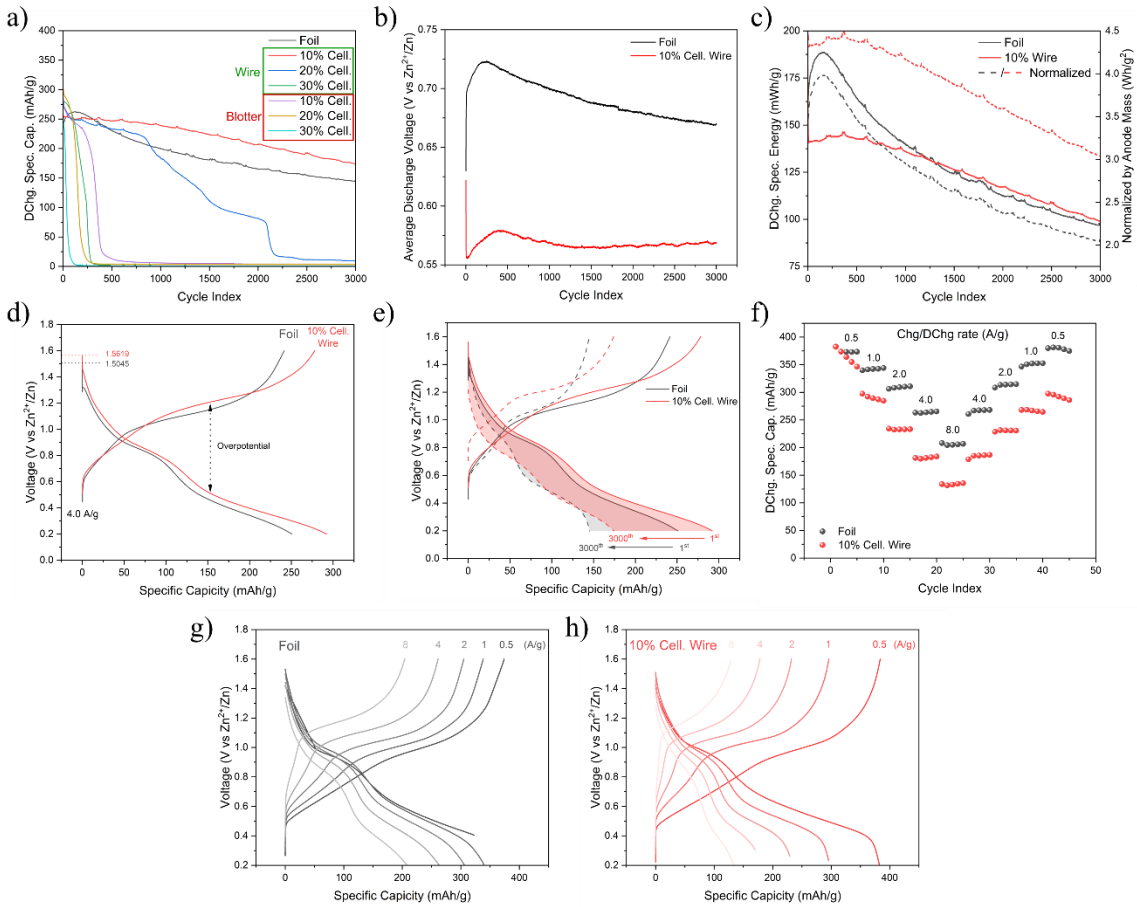

Figure 4.2.9 (a) Galvanostatic discharge of various cellulose concentrations with wire/blotter side facing cathode. (b) average voltage, (c) discharge specific energy (left axis) and discharge specific energy normalized by anode mass (right axis) (d) First GCD curve, (e) First and 3000th GCD curve, (f) GCD different discharge rates (A/g) of 10% cell wire and zinc foil. First discharge curve of each rate of (g) zinc foil and (h) 10% cell. Wire.

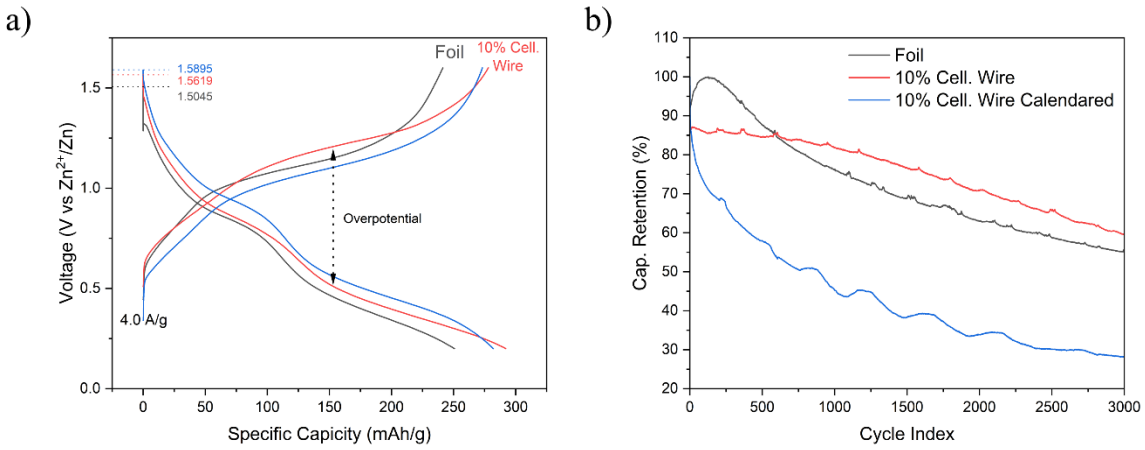

Figure 4.2.10 Capacity retention vs cycle index and GCD curve of first cycle of zinc foil, 10% cellulose, and calendared 10% cellulose fibrous anodes.

4.2.4 Dendrite Free Anode

In the previous section the fibrous anode was shown to improve cycling stability for ZIBs furthering advances towards longer battery life. To better understand electrochemical performance the anode was analyzed after 3000 cycles to investigate changes to the material structure. Figure 4.2.11-a shows SEM imaging of the zinc foil and 10% cellulose wire sample after 3000 discharge/charge cycles at 4 A/g. From this figure pitting was observed in the zinc foil with significant dendrite formation. On the other hand, the fibrous anode had a very smooth surface with insignificant dendrite formation. Interestingly, when looking at the side of the fibrous anode facing the collector (the blotter side), a surface rich with dendritic structures was observed with significant electron scattering. This is indicative of higher zinc content on this side of the anode after cycling compared to wire side (facing the separator separator) and is much more pronounced than differences observed between the blotter and wire side before cycling. Figure 4.2.11-b shows EDS measurements taken of the cross section of the fibrous anode with the side facing the separator

(wire side) on the bottom and figure 4.2.12 shows the corresponding collected spectrum. A zinc free layer was observed at the wire side after cycling creating a uniform sieving layer. This trend was further quantified by the line scan EDS shown in figure 4.2.11-c showing zero counts for the bottom quarter of the material thickness. During cycling plating and stripping reactions lead to migration of zinc through the thickness of the material creating a sieving layer zinc must migrate through to reach active sites for plating [141], [146].

Overall, the surface was much smoother, and the larger thickness of the material and two sidedness seemed to aid in limiting dendrite formation on the surface of the wire side which was in contact with the separator. With the formation of a sieving layer occurring the zinc ions must migrate through a porous layer before reaching reactive active sites helping to improve even deposition through electric field homogenization and randomized transport through a porous structure. These factors contributed to improving the battery lifespan and show the advantages of the inhomogeneous structure allowing for a highly conductive side (blotter) and porous side (wire).

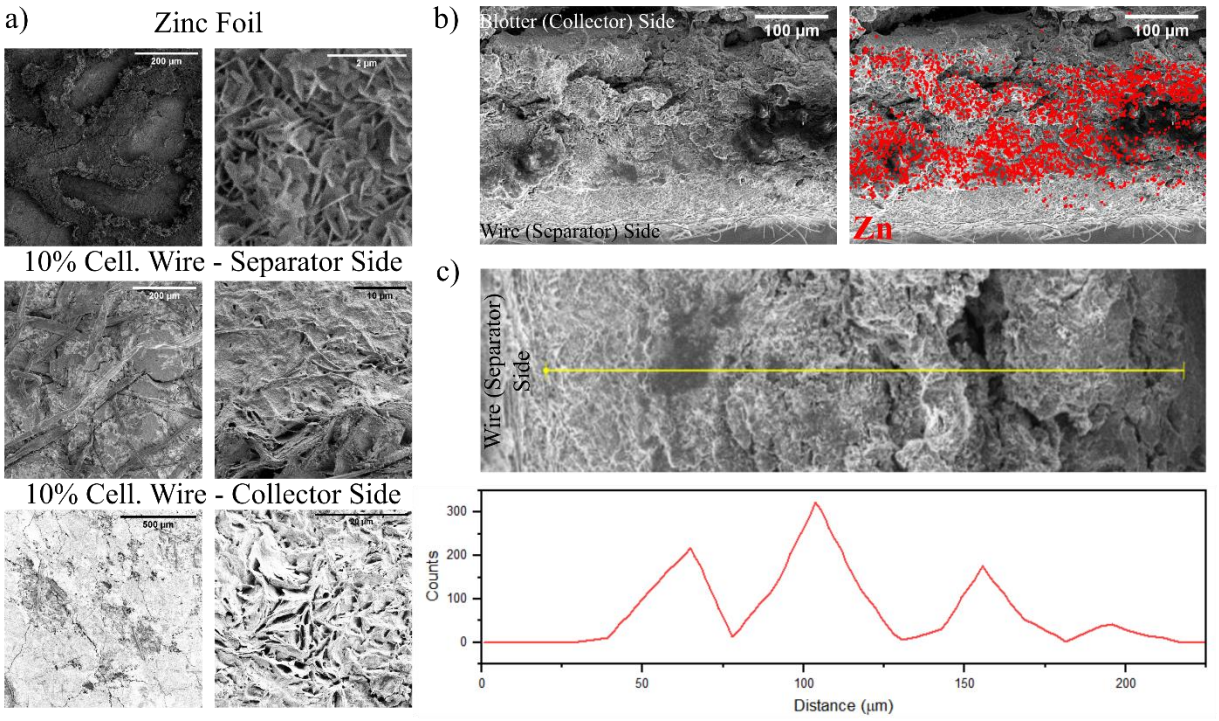

Figure 4.2.11. (a) SEM micrographs of the surface of zinc foil and both sides of best performing fibrous anode (10% cell. Wire) after 3000 cycles. (b) SEM and line scan EDS image of fibrous anode cross section. (c) SEM and EDS overlay of cross section

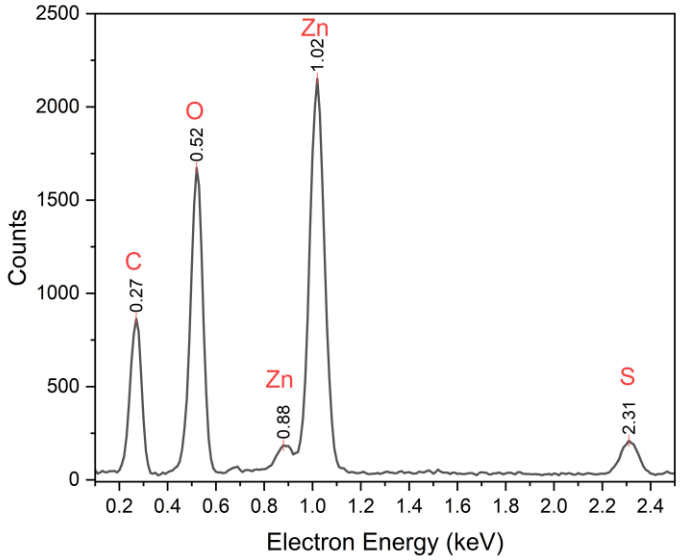

Figure 4.2.12 Energy Dispersive X-ray Spectroscopy spectrum for zinc foil cross section after cycling

4.3 Conclusions

In this section a zinc anode was developed creating an inhomogeneous structure that was shown to be advantageous for battery cycling. In this manner an increase in battery capacity retention was observed increasing from 55% for zinc foil to 60% for the developed fibrous anode after 3000 cycling. Although the anode capacity was improved the electrode kinetics were shown to be worse in comparison to the zinc foil. These changes show a scalable method of manufacturing a zinc anode that may improve battery cycling capabilities of aqueous zinc ion batteries leading to more sustainable methods of zinc anode production.

Additionally, this anode may be applied to various zinc battery applications leading to lower zinc metal requirements and easily recycled battery materials. The zinc anode developed

here was used for the electrochemical based leak detector that was discussed in section 1 and The development of the additional wick and device will be discussed in the following sections.

5 Wick Design and Implementation of Electrochemical Leak Detector

5.1 Background

As discussed in section 1 a new leak detection mechanism was envisioned for this research, being fully autonomous and not needing external power sources. While the power output of the TEPG was rather low and not capable of powering WI-FI devices it was shown that it could be used to power an LED and a latching circuit for leak detection. In section 4 a zinc anode was developed and shown to have great capabilities zinc based batteries and potentially for self-generating large amounts of power for IOT devices in a leak detection system. To complete the device, design an efficient wick must first be developed to act as a battery separator, hold electrolyte, and quickly wick water to the battery.

Wicking materials have been heavily investigated and modelled using liquid flow models developed by Richards for capillary conduction in porous media and modified for different porous materials [172]. Common materials used for developing wicks include jute [173], [174], [175] and cotton which are usually employed for solar stills [175], [176]. Additionally paper wicks are often used for sensing devices and biomedical devices [120], [121], [177], [178], [179], [180], [181] and textiles are commonly used in clothing and smart electronics [114], [122], [182]. Paper is of particular interest for the battery-based leak detector due to its scalability and capabilities as a wicking material. For example, Camplisson et al. were able to see improved wicking speed

essentially doubling the speed of the fluid traveling vertically in the wick by using a multiply channel consisting of paper and wax, using tonner to print hydrophobic channels for further advancements in lab on a chip applications [183]. Additionally fundamental modelling research done by Lucas led to the Lucas-Washburn equation which showed the capillary radius dependence on paper strip wicking [184]. Paper and different cellulose-based materials have been shown to be advantageous as separators in battery systems. For example, Lv et al. developed a cellulose nanofibril reinforced paper to be employed as a lithium ion battery separator showing improved capacity retention of 91% after 100 cycles compared to cellulose and propylene separators (52% and 84% respectively) [185]. Another study completed by Zhang et al. found that cellulose paper based separators outperformed commercial polyolefin separators in lithium ion batteries due to improved wettability of the electrolyte and improved ionic conductivity seeing increased rate and cycling performance [186]. These are just two examples in an entire field of research where several other studies have used cellulose based battery separators in rechargeable zinc air batteries [187], [188], [189], aluminum air batteries [190], [191], [192], and zinc ion batteries [193], [194], [195].

In this study a paper-based zinc anode has been developed based on previous research to produce CNT embedded smart paper and these materials can be used for zinc air batteries. Typical zinc air batteries consist of a zinc anode, potassium hydroxide electrolyte, and porous carbon cathode having the overall shown in equation 5.1-1 [82].

Equation 5.1-1

$$2Zn + O_2 \rightarrow 2ZnO$$

While there is currently a large influx of research into rechargeable zinc air batteries these require development of oxygen evolution cathodes to recharge the battery and still require great advancements [72], [77], [78], [79], [82], [86], [196]. Primary zinc air batteries on the other hand

have been around for a long time and the typical household AAA battery are zinc-air systems and are known to have greater capacity with a smaller size. For example the typical energizer AAA battery has a capacity of 3600 mAh, 1.3 V nominal voltage, 11.7 g weight, and 400 mWh/g specific energy density [197]. When compared to a Duracell zinc/manganese dioxide AA battery with a specific energy density of 195.7 mWh/g [198] it is obvious that these batteries are much better for light weight operations. However, due to the slow kinetic of the oxygen reduction reaction, especially with carbon catalysts, these devices are not ideal for high discharging applications but are perfectly adequate for powering IOT devices. Using the zinc-air architecture for the leak detector is advantageous because of these reasons as the battery does not need to be recharged and only needs to provide sufficient voltage and current to power an IOT device which is low compared to many other electronics. Smart paper has good properties for the proposed detector due to its porous nature which allows oxygen diffusion to solid electrolyte interface, has good hydrophobicity allowing better wicking in the separator, and is durable in wet environments.

The paper-based wick presented here was designed to be used as a battery separator, intended to quickly wick water to the electrode surface to allow redox reactions to begin, turning the circuit on without requiring external power or stimulus. As the cathode, CNT embedded paper was used to catalyze oxygen reduction at the surface and the calendared zinc anode developed in the previous section and calendared was used as. The calendared sample was used since it displayed a higher hydrophobicity to help improve wicking speed, as well as a higher capacity at faster discharge rates which is expected to improve device response time. The development and use of this novel leak detector is presented and evaluated for its advantages in this section.

5.2 Results and discussion

5.2.1 Wick Synthesis and Characterization

Ground calcium carbonate ($CaCO_3$) is a common material used in the paper industry as a filler to increase density, reduce porosity, improve printing quality, and reduce cost [155], [199], [200]. While $CaCO_3$ is used in many printer paper grades it is known to reduce paper strength by decreasing inter-fiber-OH bonding [154], [156], [157], [201]. In this study, this OH bonding decrease was used to reduced densification and increase paper porosity by incorporating GCC into the fiber matrix and then dissolving it using hydrochloric acid to create a simple double displacement reaction according to equation 5.2-1 [202]. This modification to the paper was intended to create a highly porous structure to help improve wicking speed.

Equation 5.2-1

$$CaCO_3 + 2HCl \rightarrow CO_2 + CaCl_2 + H_2O$$

Figure 5.2.1-a shows a schematic of the method of wick synthesis showing the preparation of a paper with $CaCO_3$ filler followed by HCl dissolution to produce a highly porous structure. Figure 5.2.1-b shows the results for the approximated $CaCO_3$ content and associated total retention of pulp slurry mass at different $CaCO_3$ charges. These values were determined gravimetrically by assuming no fiber was lost during the dissolution step and all $CaCO_3$ was completely dissolved. The results show a clear increase in both $CaCO_3$ content and retention, likely due to densification of the paper during formation leading to lower porosity of the mat formed on the screen during filtration allowing for more filler to be retained. Figure 5.2.1-c shows the density, thickness, and SEM mask area fraction of the different $CaCO_3$ loading. From the figure an increase in thickness and reduced density was observed but significant changes with different $CaCO_3$ loadings were not seen. However, with increasing $CaCO_3$ loading the SEM mask area increased indicating a higher degree of porosity.

Figure 5.2.1-c shows wicks produced with increasing $CaCO_3$ content and figure 5.2.2 shows images of the control before and after dissolution (-a and -b respectively) as well as imaging for sample 0.6 g $CaCO_3$/g (c and d). From these figures a dense structure with $CaCO_3$ granules was apparent filling the spacing between the fibers and likely inside the lumen, however after dissolution some exfoliation was observed in the control sample, but a much larger change was observed for the 0.6 g $CaCO_3$/g sample. Here the lumens were not compressed or filled and there was a large degree of fiber separation creating a highly porous structure. The lumen of these fibers appears to have diameters in the range of 2- 6 um in diameter which can act as efficient capillary channels having diameters much smaller than the typically laboratory glass capillary (75 – 100 μm). As shown by Zakaria et al deposition of fillers inside the lumen is common and can even be preferentially chosen using different chemical methods [203], [204].

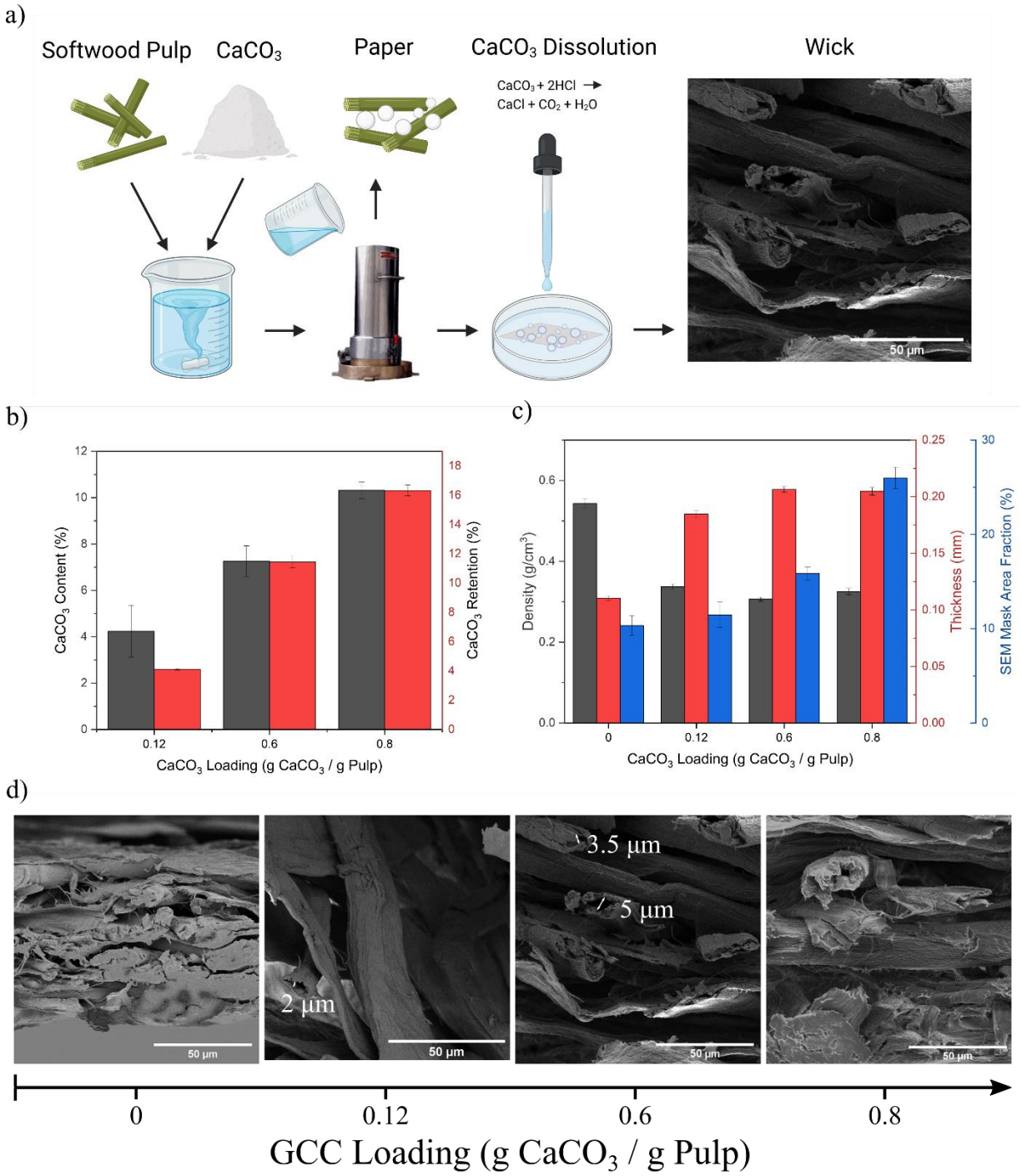

Figure 5.2.1 (a) Schematic of synthesis method for production of wick for leak detection device. (b) Approximated GCC content and mass retention in paper handsheet at different GCC loading on pulp fiber mass. (c) Density, Thickness and SEM Mask Area Fraction calculated using image J software to qualitatively compare material porosity. (d) SEM image of wicks formed with varying levels of GCC loadings after GCC is dissolved.

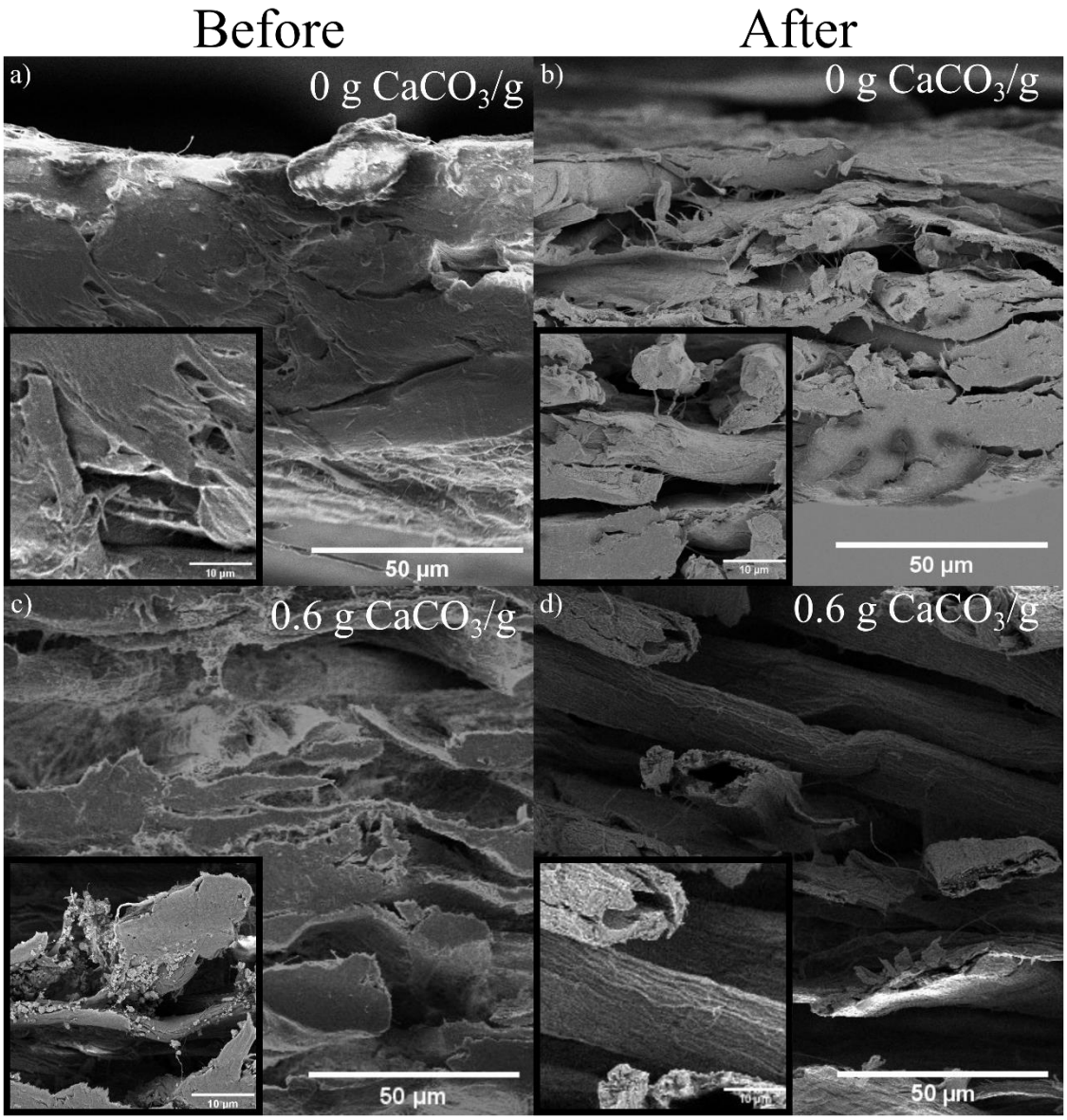

Figure 5.2.2 SEM imaging of wick cross section of control sample before (a) and after (b) HC treatment as well as 0.6 g GCC/g sample before (c) and after (d) with high magnification image inset. (e)

5.2.2 Wicking Performance

The produced wicks were evaluated by their wicking speed. Wicking measurements were conducted by dipping the end of the wick into a petri dish filled with DI water and videotaped using an iPhone camera with careful experimental setup to ensure accurate measurements. The schematic of the experiment is displayed in figure 5.2.3-a and figure 5.2.3-b shows the results

extracted from the videos. At 0.12 g $CaCO_3$/g a large increase in wicking speed was observed in followed by further improvement to performance at 0.6 g $CaCO_3$/g, however at 0.8 g $CaCO_3$/g an extreme drop in wicking performance was observed. From SEM imaging it is possible to see that at 0.8 g $CaCO_3$/g the fiber separation becomes too large and creates many large pores which can act as reservoirs holding onto the liquid in its macropores preventing water from wicking up through the lumen and smaller interstitial spacings. Furthermore modeling of the transport of fluid through porous media has been developed by several researchers [120], [172], [177], [178], [205] and can be realized in this study by the Lucas-Washburn equation shown in equation 5.2-1a where h is the height of the waterline in the wick in cm, D the transport coefficient in cm^2/s, and t the time in seconds [121], [179], [180], [206]. The transport coefficient can be further related to the capillary diameter (d_c) by equation 5.2-1b where μ is the dynamic viscosity of the water (8.9E-4 Pa·s), γ is the surface tension (0.072 N/m), and θ is the contact angle between the water and cellulose fiber. The contact angle was estimated to be 31° based on reports of single fiber contact angle of bleached kraft pulp by Koljonen et al and other similar works [207], [208], [209]. By this model the average capillary radius could be estimated and is shown in figure 5.2.3-c. Figure 5.2.3-d shows the SEM imaging for the 0.6 $CaCO_3$/g sample which has the fastest wicking speed and shows a lumen diameter similar the estimated average capillary diameter which is also reflected in figure 5.2.1-d for varying $CaCO_3$ loadings.

Equation 5.2-2

$$h = \sqrt{Dt}$$

$$d_c = \frac{4D\mu}{\gamma cos\theta}$$

The likely cause of this relation can be explained by filler incorporation into the lumen during synthesis which prevents compaction of the fibers during wet pressing. After the removal of the ground $CaCO_3$ the lumen is left open, and this effect is likely optimized at the 0.6 g $CaCO_3$/g charging.

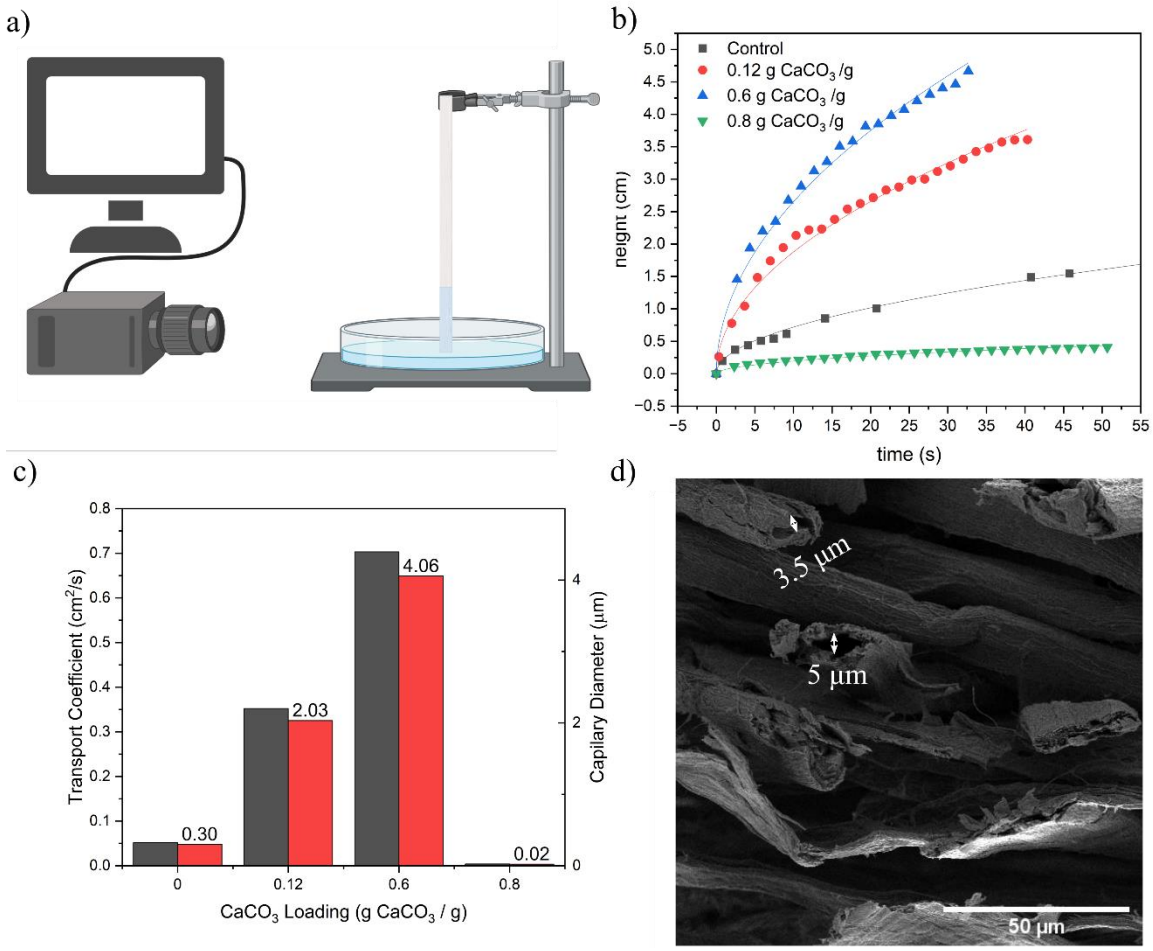

Figure 5.2.3 (a) schematic of wicking measurement setup. (b) Wicking height vs time with Lucas-Washburn fitted equations. (c) calculated transport coefficients and extracted capillary diameters. (d) SEM of the 0.6 g $CaCO_3$ / g fiber sample after dissolution step.

5.2.3 Zinc battery-based Leak Detection

In the previous sections a wick was developed and in section 3 a TEPG was developed and applied as a leak detector. In this section the wick was used as a wicking battery separator to dissolve electrolyte and activate a battery for leak detection. In the following section the Zinc

anode prepared in section 4 was used for a zinc air battery to show its effectiveness as a sensor for leak detection and self-powered notification. Figure 5.2.4-a shows a picture of the device with its included schematic showing the dimensions of the battery cell as discussed in section 2. To evaluate the effect of KOH doping and clamping pressures applied to the device the wicking speed of the device was also measured for 0.6g $CaCO_3$/g and is shown in figure 5.2.4-b which can be seen to be slightly slower having a transport coefficient of 0.48 cm^2/s most likely caused by pressures created by the clamping forces opposing wicking forces. Figure 5.2.4-c shows the voltage response of the different wicks discussed in previous section showing plots of the voltage vs time initially having a peak voltage and relatively stable output with voltage variations resulting in the early stages due to changes in battery composition as doped KOH is dissolved and activated in battery. The fastest response can be seen for 0.6 g $CaCO_3$ /g reflecting similar trends to wicking measurements.

Figure 5.2.4-d shows the voltage vs the modelled wick height of the device for the 0.6 g $CaCO_3$/g wick. With a wick height of 5 cm, a cathode being centered on a 16 mm plate, and having an 11 mm diameter the edge of the cathode was approximately 3.65 cm from the base of the wick. From figure 5.2.4-d the voltage was initially stable around 0.2 V, likely caused by moisture absorption from the air and the nature of the materials. At ~ 3 cm the device voltage spikes confirm activation by fluid contact with the cathode connecting the entire device. Additionally, figure 5.2.4-e shows a similar plot with the short circuit current response on the y axis and modeled wicking height on the x axis. In this figure a large spike in current appeared to begin at ~4.5 cm after the entire cathode would be covered creating the maximum current output. This shift in height between voltage and current peak may be explained by the surface coverage of the cathode which largely influences the current but does not the voltage as voltage is an intensive property [171].

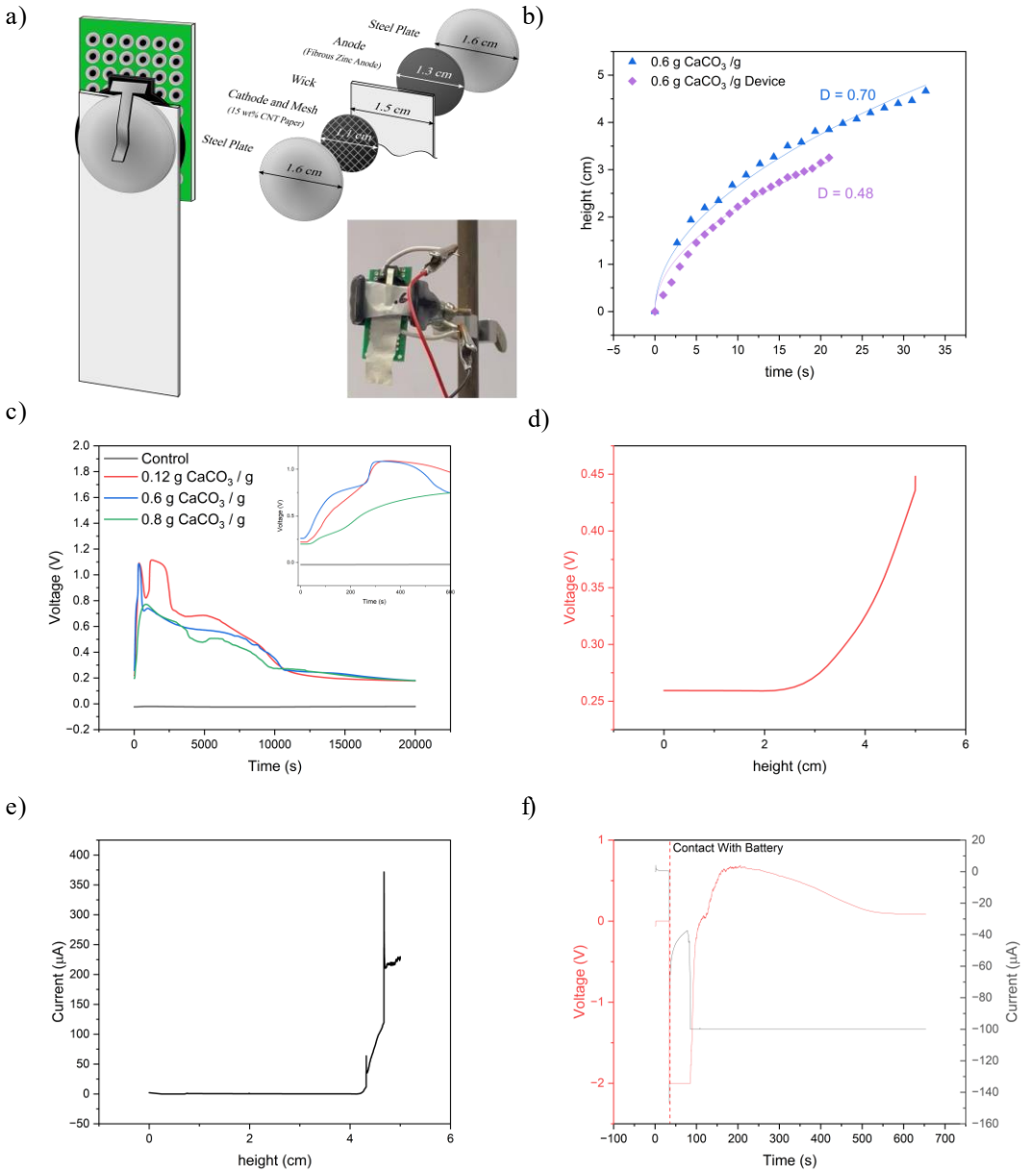

Figure 5.2.4 (a) Exploded schematic of leak detection device. (b) Wicking height vs time of 0.6 g $CaCO_3$ / g wick and leak detection device equipped with KOH doped wick. (c) Voltage vs time of leak detectors with different wicks. (d) Open circuit voltage and (e) short circuit current of best performing leak detector (0.6 g $CaCO_3$ / g wick) vs wicking height. (f) Voltage of best performing leak detector vs time under constant -100 μA load.

Finally, to show the effect of usable performance of this setup the device was discharged under a constant load of 100 uA of current. Here a usable voltage was not observed until ~ 100 s when the

wick was fully wet, the doped KOH has been dissolved, and the battery was able to output 100 uA of current. This current was sustained for ~700s and with a nominal voltage of 0.65 V. At this output six devices in the series could produce a nominal voltage of 3.9 V and charge a 1 mF capacitor to sustain the 150 mA of current required for the ESP8266 RF transmission to be able to be sustained for a 10 ms pulse.

5.2.4 TEPG based Leak Detection

Although the energy output of both battery and TEPG based devices were quite low compared to the power requirements for a typical Wi-Fi microcontroller, such as the ESP8266 (3.3V, 170 mA during Wi-Fi operation [84]), the power produced by only one device may still activate a circuit allowing a battery to power the microcontroller using an "energy as data" approach. A bipolar junction transistor (BJT) switching circuit was first considered for the task, however from figure 5.2.5-a it can be seen that the amount of current allowed through a transistor is dependent on the current supplied at its base. The BJT equations show that the maximum current allowed to travel through the collector (I_C) is proportional to the base current (I_B). This proportional constant (β), called the gain, is a characteristic of the BJT itself [210] and for a common 2N2222 NPN type transistor β has a value of 100 when operating in the range of ESP8266 power requirements [211]. Additionally, a BJT requires a sufficient voltage at its base (~0.8 V in this case) to turn the transistor on and allow current to flow between base and emitter. Thus, for the developed EC-enhanced TEPG or zinc battery-based detectors (herein referred to as energy-as-data device) operating under 100 μA of current draw the maximum collector current would be only 1 mA and after the voltage dropped below 0.8 V the load could no longer draw current. To deal with this problem a latching circuit was designed to allow the circuit to be activated by the energy-as-data device and then hold itself in the on state (figure 5.2.5-b). The circuit works by connecting a P-

type metal oxide semiconductor field effect transistor (MOSFET, component number IRF9640 [212]) to the positive node of the battery through a 1 MΩ resistor to pull its voltage to that of the battery and maintain the MOSFET in the off state. A 2N2222 NPN BJT is connected between the MOSFETs' gate and ground and when its base is activated by the energy-as-data devices' voltage the gate of the MOSFET is pulled to ground. Once this is pulled to ground current is allowed to flow through the load and power the device. To keep the gate of the MOSFET at 0 V a 470 kΩ resistor was connected between the low side of the transistor (high side of the load) and the transistors base to apply a high voltage to the gate even after the energy-as-data device had stopped producing energy. In this way the MOSFET was "latched" in the on state and the load was able to continuously operate even after the energy-as-data device voltage dropped below 0.8 V. A rectifying diode (1N4148 [213]) was connected between the energy-as-data device and transistor base to prevent current flow into the device and to prevent accidental triggering by creating a threshold voltage to overcome the diode voltage drop. Additionally, a 0.1 μF capacitor was connected between the transistor base and ground to further aid in accidental activation prevention. Figure 3.2.11-c shows the results for a SPICE simulation of this circuit using voltage data from a TEPG that was dopped with 30 μL of alum solution, allowed to dry, and then wetted with 30 μL of filtered rain water to simulate a water leak. After the onset of the droplet the TEPG voltage rose quickly, and the response of the circuit allowed for the load to draw 150 mA within 3 seconds of the droplets contact with the device. Additionally, the circuit remained in the on state even after the TEPG voltage dropped below 0.5 V as shown in figure 3.2.11-d. Additionally, the simulation showed only 17 μA of additional current consumption by the latching circuit in the on state and an insignificant 56 pA of current consumption in the off state. Additionally, only a very small voltage drop across the MOSFET was observed with a voltage of 5.93V compared to the 6V battery input

and this along with the slight addition in current consumption led to a power efficiency of 98.6%. By using this latching circuit and cleaver development of microcontroller firmware a Wi-Fi leak detection device can be achieved that does not require additional power or battery replacements for many years and supplemental video S1 shows the built device in operation, working better than expected sending a text message in ~ 17 seconds.

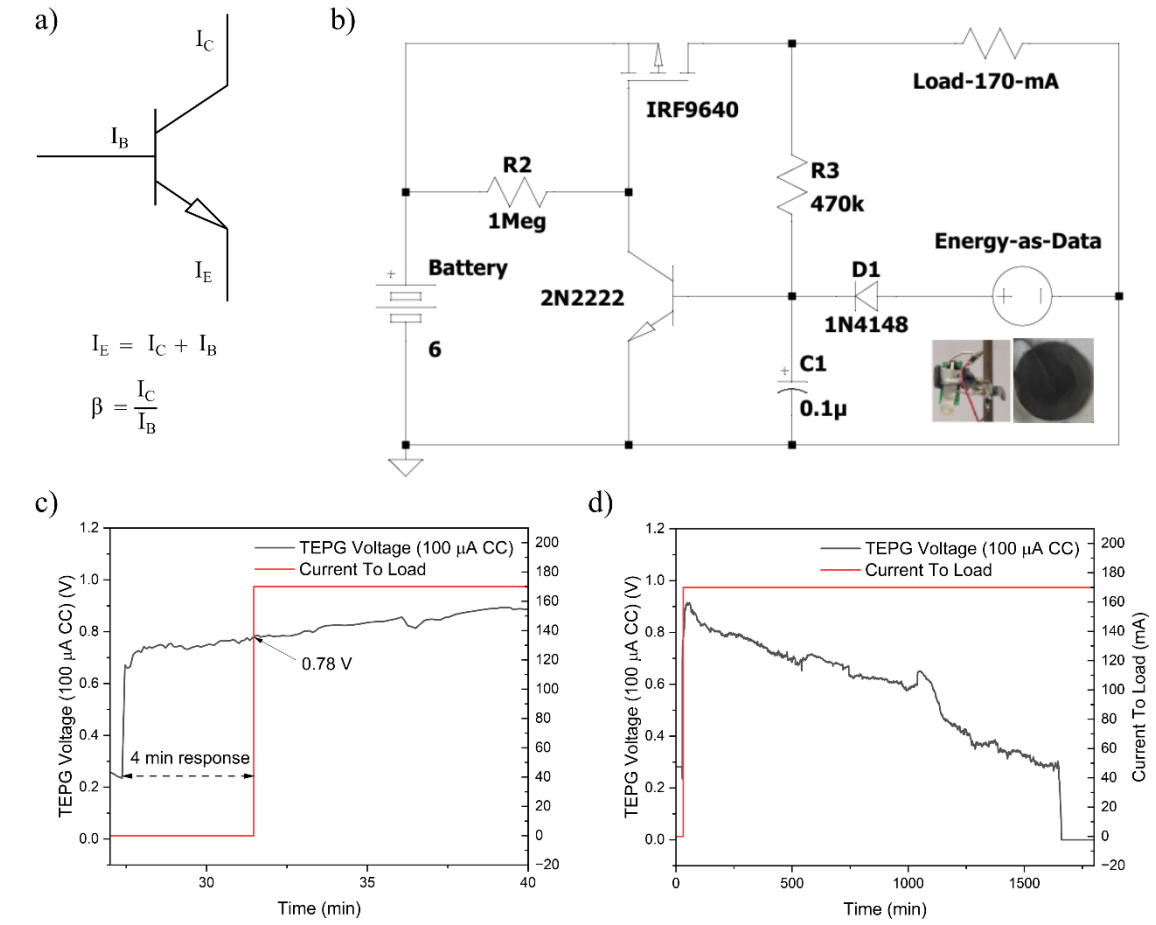

Figure 5.2.5 (a) Schematic showing a BJT and associated equations relating the collector, base, and emitter currents (I_C, I_B, and I_C respectively) to each other and the BJTs gain (β). (b) Schematic of latching circuit used in SPICE simulation for TEPG leak detector design. (c and d) Alum doped TEPG voltage response to a water droplet and the current across the load in the latching circuit vs time.

5.3 Conclusions

In this section a wick was developed, and a novel battery-based leak detection device was produced using the optimized wick. Using this device a leak detector was achieved capable of power an LED signaling detection system by connected ~2 to 3 devices in series. Unfortunately, the device presented here did not achieve the desired goal, however by using an energy-as-data approach a wireless leak detection system was achieved capable of being powered by a commercial battery and activated by both battery-based device and TEPG device using their energy as data to control a simple logic circuit. This concept was built and tested and performed better than the simulated expectations, sensing a leak and sending a text message alert ~17 seconds after the device was wetted.

6 Conclusion and future work

6.1 Conclusions

The goal of this manuscript was to further advance leak detection devices, improving performance by designing an autonomous leak detection system capable of self-triggering and powering. Two novel leak mechanisms were proposed and developed using advanced materials achieving two autonomous leak detectors both capable of LED signaling. The TEPG device designed in section 3 displayed quick and powerful leak detecting capabilities having a fast 3 s response time capable of producing an average voltage of 0.7 V with 0.01 mA current output. With this level of power output, the device was able to power an LED leak detector using 9 devices. By using an electrochemical enhancement approach a new TEPG device with incredibly competitive performance was achieved, and by focusing on the electrochemical aspects further novel leak detection mechanisms were hypothesized.

In pursuit of further advancements to the leak detector design, a battery based on a zinc-air battery architecture was developed in which conductive carbon nanotube paper used for the TEPG would serve as the cathode. In principle, the design called for a single use device, and to reduce waste and improve sustainable aspects of the project a zinc anode was first designed. The anode was developed based on paper materials and conductive paper development principles. This led to the production of a zinc anode that could be easily disposed of or recycled, reducing potential e-waste by the development of such a system. Additionally, the fibrous zinc anode was shown to improve battery cycling stability achieving capacity retention of 60% compared to 55% for zinc foil after 3000 cycles further advancing zinc anode technology. To complete the device a wick was developed using paper-based materials and by doing so a wick capable of transporting water 4 cm high in ~30 seconds was developed allowing for quick leak detection. While this device response was much slower compared to the response of a TEPG, the wicking mechanism can fulfill needs for different applications such as leak detection in water heaters as opposed to a pipe as shown in figure 6.1.1.

In this juncture of the project, it was realized that a completely self-powered detector was not possible with the developed devices, however by changing to an energy-as-data approach a fully autonomous device was achieved. With the incorporation of TEPG constant current discharge data, a SPICE simulation of the latching circuit was developed and predicted leak detection at 0.8 V output under 0.01 mA of current, requiring very little power for fast and efficient leak detection. By designing this latching circuit to connect a battery, a wireless detection system capable of sending a text alert in ~17 seconds after the energy-as-data device being wetted was achieved. In doing so the device off state power consumption was minimized to maintain a discharge lifespan ~16 x greater than a typical commercial battery shelf life suitable for most applications. Overall,

the work presented here spans across multiple disciplines including paper making, materials science, leak detection, sensing, and electrochemistry advancing topics and research in these areas.

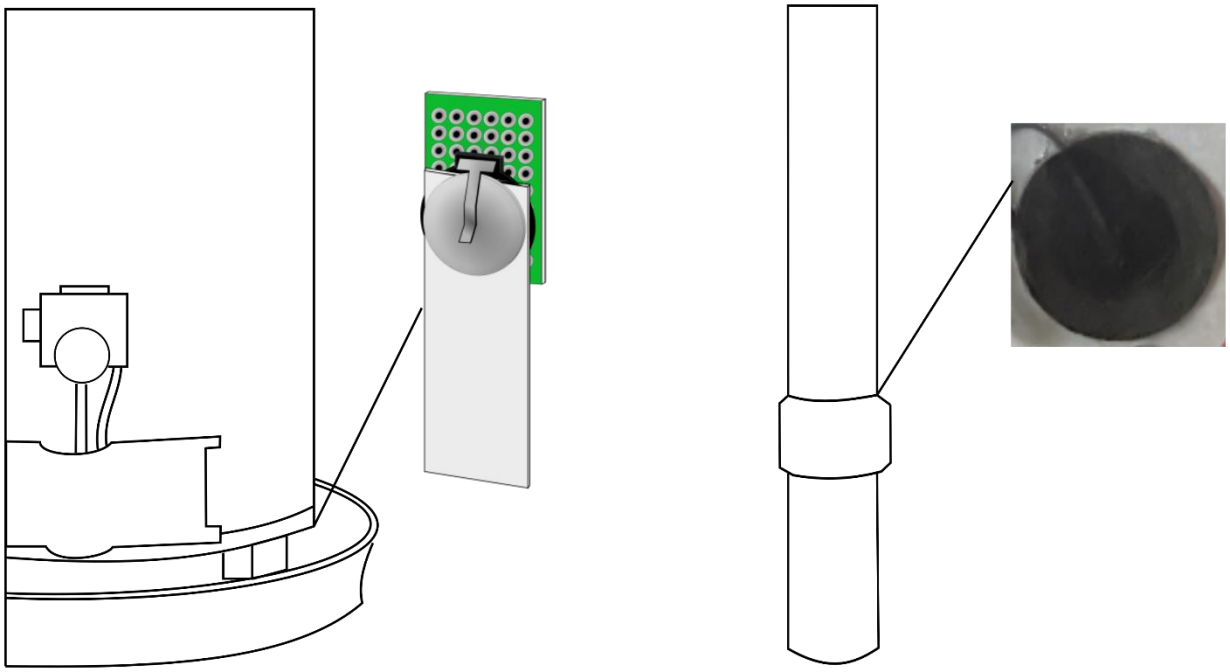

Figure 6.1.1 Depiction of different applications for the two designed energy-as-data leak detection devices.

6.2 Further work

With the conclusion of this research, many problems have been identified that can be improved upon and lead to further advancements in moisture enabled electricity, paper-based batteries, and leak detection systems. With the increased TEPG performance achieved by device configuration and electrochemical enhancement further optimization of the CNT paper composition could improve energy generation. Furthermore, the replacement of the CNT paper with the developed fibrous zinc anode could potentially reach even greater heights of performance. Additionally, investigation into rechargeable electrochemically enhanced TEPGs may be

advantageous, creating a rechargeable device that also produces electricity by TEPG mechanisms leading to greener power generation while allowing for higher energy outputs required for many electronics. Further investigation into the mechanisms of the TEPG may lead to advancements in smart paper manufacturing and field of MEGs allowing for a better understanding of the technology and possible enhancement for green energy.

Unfortunately zinc anode kinetics were neglected in this study as the focus was placed on the improvement of ZIB cycling lifespan. By further improvements to the anode synthesis method, creating thinner materials, using passive layers, and controlling sieving layer thickness it is believed that further improvements can be achieved. For example Kaolin clay has been used as a sieving layer for zinc anodes to improve cycling stability and is a common papermaking additive that may synergize with the fibrous zinc anode [146]. Additionally, development of paper-based battery cathode and separator materials may be investigated as fully integrated nanocellulose based batteries have been shown to improve performance in ZIBs especially for flexible batteries [134]. By pursuing these future research ideas, a new field of paper-based battery materials ideal for battery recycling may be achieved.

While proof of concept of a ZAB based leak detector was presented in this research, further improvements need to be made to increase power output, battery design, and leak sensing speed. This can be achieved without further material modification but simple changes to the device design. By using a cylindrical AA battery format and extending the anode and cathode down the entire length of the wick, wicking speed may be increased as well as active surface area for redox reactions improving battery performance and sensing response time. By pursuing these ideas this research may be further advanced achieving even greater improvements towards wireless, fully autonomous leak detection.

7 References

[1] O. US EPA, “Fix a Leak Week.” Accessed: May 18, 2023. [Online]. Available: https://www.epa.gov/watersense/fix-leak-week

[2] “Average monthly cost of water United States 2019,” Statista. Accessed: May 18, 2023. [Online]. Available: https://www.statista.com/statistics/720418/average-monthly-cost-of-water-in-the-us/

[3] “Water Damage Statistics [2023]: Claim Data & Facts,” iPropertyManagement.com. Accessed: May 28, 2023. [Online]. Available: https://ipropertymanagement.com/research/water-damage-statistics

[4] U. C. Bureau, “2019 U.S. Population Estimates Continue to Show the Nation’s Growth Is Slowing.” Accessed: Nov. 02, 2024. [Online]. Available: https://www.census.gov/newsroom/press-releases/2019/popest-nation.html

[5] “Average Water Usage in the United States | Aquasana.” Accessed: Nov. 02, 2024. [Online]. Available: https://www.aquasana.com/info/average-water-usage-in-the-united-states-pd.html?srsltid=AfmBOorvkHpYs0Zsskyjuc6Qw5NhN3929ve_6fiYwmt9BfkyebrrnKIb

[6] S. M. H. your say, “Water leak at Paris Global Switch data center causes fire, leads to outages at Google.” Accessed: Nov. 02, 2024. [Online]. Available: https://www.datacenterdynamics.com/en/news/water-leak-at-paris-global-switch-data-center-causes-fire-leads-to-outages-at-google/

[7] P. J. 1 Comment, “The OVHcloud fire still smolders.” Accessed: Nov. 02, 2024. [Online]. Available: https://www.datacenterdynamics.com/en/analysis/ovhcloud-fire-france-data-center/

[8] “How Many Data Centers Are There and Where Are They Being Built?” Accessed: Nov. 02, 2024. [Online]. Available: https://www.abiresearch.com/blogs/2024/07/16/data-centers-by-region-size-company/

[9] A. EurEau, “Europe’s water in figures. An overview of the European drinking water and waste water sectors.".” EurEau, 2021.

[10] OECD, *OECD Environmental Outlook to 2030*. Paris: Organisation for Economic Co-operation and Development, 2008. Accessed: Nov. 02, 2024. [Online]. Available: https://www.oecd-ilibrary.org/environment/oecd-environmental-outlook-to-2030_9789264040519-en

[11] C. S. Laspidou, “ICT and stakeholder participation for improved urban water management in the cities of the future,” *Water Util. J.*, vol. 8, pp. 79–85, 2014.

[12] C. He *et al.*, “Future global urban water scarcity and potential solutions,” *Nat. Commun.*, vol. 12, no. 1, p. 4667, Aug. 2021, doi: 10.1038/s41467-021-25026-3.

[13] “Global Data Center Water Leak Detector Market Research Report 2024,” Market Research QYRE-Auto-11F16539. Accessed: Nov. 02, 2024. [Online]. Available: https://reports.valuates.com/market-reports/QYRE-Auto-11F16539/global-data-center-water-leak-detector

[14] R. and Markets, “Global Water Leakage Detector Systems Strategic Industry Report 2024: Market to Reach $7.2 Billion by 2030 - Smart Cities Concept to Underpin Growth,” GlobeNewswire News Room. Accessed: Nov. 09, 2024. [Online]. Available: https://www.globenewswire.com/news-release/2024/02/22/2833841/28124/en/Global-Water-Leakage-Detector-Systems-Strategic-Industry-Report-2024-Market-to-Reach-7-2-Billion-by-2030-Smart-Cities-Concept-to-Underpin-Growth.html

[15] H. Fan, S. Tariq, and T. Zayed, “Acoustic leak detection approaches for water pipelines,” *Autom. Constr.*, vol. 138, p. 104226, Jun. 2022, doi: 10.1016/j.autcon.2022.104226.
[16] B. youngpyo Jo and J. Boon, “Combined CCTV and leak detection technology for in-service water transmission mains,” *Water Pract. Technol.*, vol. 7, no. 4, Dec. 2012, doi: 10.2166/wpt.2012.093.
[17] L. Hoegner and U. Stilla, “Thermal leakage detection on building facades using infrared textures generated by mobile mapping,” in *2009 Joint Urban Remote Sensing Event*, May 2009, pp. 1–6. doi: 10.1109/URS.2009.5137681.
[18] M. Yahia, R. Gawai, T. Ali, Md. M. Mortula, L. Albasha, and T. Landolsi, “Non-Destructive Water Leak Detection Using Multitemporal Infrared Thermography,” *IEEE Access*, vol. 9, pp. 72556–72567, 2021, doi: 10.1109/ACCESS.2021.3078415.
[19] M. H. Manekiya and P. Arulmozhivarman, “Leakage detection and estimation using IR thermography,” in *2016 International Conference on Communication and Signal Processing (ICCSP)*, Apr. 2016, pp. 1516–1519. doi: 10.1109/ICCSP.2016.7754411.
[20] J. D. Butterfield, R. P. Collins, and S. B. M. Beck, “Influence of Pipe Material on the Transmission of Vibroacoustic Leak Signals in Real Complex Water Distribution Systems: Case Study,” *J. Pipeline Syst. Eng. Pract.*, vol. 9, no. 3, p. 05018003, Aug. 2018, doi: 10.1061/(ASCE)PS.1949-1204.0000321.
[21] Y. A. Khulief, A. Khalifa, R. B. Mansour, and M. A. Habib, “Acoustic Detection of Leaks in Water Pipelines Using Measurements inside Pipe,” *J. Pipeline Syst. Eng. Pract.*, vol. 3, no. 2, pp. 47–54, May 2012, doi: 10.1061/(ASCE)PS.1949-1204.0000089.
[22] O. Hunaidi, W. Chu, A. Wang, and W. Guan, “Detecting leaks in plastic pipes,” *J. AWWA*, vol. 92, no. 2, pp. 82–94, 2000, doi: 10.1002/j.1551-8833.2000.tb08819.x.
[23] M. S. El-Abbasy, F. Mosleh, A. Senouci, T. Zayed, and H. Al-Derham, “Locating Leaks in Water Mains Using Noise Loggers,” *J. Infrastruct. Syst.*, vol. 22, no. 3, p. 04016012, Sep. 2016, doi: 10.1061/(ASCE)IS.1943-555X.0000305.
[24] S. Tariq, B. Bakhtawar, and T. Zayed, “Data-driven application of MEMS-based accelerometers for leak detection in water distribution networks,” *Sci. Total Environ.*, vol. 809, p. 151110, Feb. 2022, doi: 10.1016/j.scitotenv.2021.151110.
[25] K. Ibrahim, S. Tariq, B. Bakhtawar, and T. Zayed, “Application of fiber optics in water distribution networks for leak detection and localization: a mixed methodology-based review,” *H2Open J.*, vol. 4, no. 1, pp. 244–261, Sep. 2021, doi: 10.2166/h2oj.2021.102.
[26] M. S. Rocha, “Acoustic monitoring of pipeline leaks,” *ISA*, pp. 89–0333, 1989.
[27] J. Barkauskas, “Investigation of conductometric humidity sensors,” *Talanta*, vol. 44, no. 6, pp. 1107–1112, Jun. 1997, doi: 10.1016/S0039-9140(96)02203-5.
[28] J. A. Covington, J. W. Gardner, D. Briand, and N. F. de Rooij, “A polymer gate FET sensor array for detecting organic vapours,” *Sens. Actuators B Chem.*, vol. 77, no. 1, pp. 155–162, Jun. 2001, doi: 10.1016/S0925-4005(01)00687-6.
[29] N. A. Mohd Yussof and H. W. Ho, “Review of Water Leak Detection Methods in Smart Building Applications,” *Buildings*, vol. 12, no. 10, Art. no. 10, Oct. 2022, doi: 10.3390/buildings12101535.
[30] M. R. Islam, S. Azam, B. Shanmugam, and D. Mathur, “A Review on Current Technologies and Future Direction of Water Leakage Detection in Water Distribution Network,” *IEEE Access*, vol. 10, pp. 107177–107201, 2022, doi: 10.1109/ACCESS.2022.3212769.

[31] K. Parikh, K. Cattanach, R. Rao, D.-S. Suh, A. Wu, and S. K. Manohar, “Flexible vapour sensors using single walled carbon nanotubes,” *Sens. Actuators B Chem.*, vol. 113, no. 1, pp. 55–63, Jan. 2006, doi: 10.1016/j.snb.2005.02.021.
[32] T. Villmow, S. Pegel, A. John, R. Rentenberger, and P. Pötschke, “Liquid sensing: smart polymer/CNT composites,” *Mater. Today*, vol. 14, no. 7, pp. 340–345, Jul. 2011, doi: 10.1016/S1369-7021(11)70164-X.
[33] A. Bouvree, J.-F. Feller, M. Castro, Y. Grohens, and M. Rinaudo, “Conductive Polymer nano-bioComposites (CPC): Chitosan-carbon nanoparticle a good candidate to design polar vapour sensors,” *Sens. Actuators B Chem.*, vol. 138, no. 1, pp. 138–147, Apr. 2009, doi: 10.1016/j.snb.2009.02.022.
[34] S. Goodman, A. Song, R. Fitzpatrick, and A. Dichiara, “Development of carbon nanotube: cellulose composites using a simple papermaking process for multifunctional sensing applications,” *Proc. Spie*, vol. 10165, p. 101650N, 2017, doi: 10.1117/12.2257364.
[35] S. M. Goodman *et al.*, “Scalable manufacturing of fibrous nanocomposites for multifunctional liquid sensing,” *Nano Today*, vol. 40, p. 101270, Oct. 2021, doi: 10.1016/j.nantod.2021.101270.
[36] S. M. Goodman, N. Ferguson, and A. B. Dichiara, “Lignin-assisted double acoustic irradiation for concentrated aqueous dispersions of carbon nanotubes,” *RSC Adv.*, vol. 7, no. 9, pp. 5488–5496, Jan. 2017, doi: 10.1039/C6RA25986C.
[37] B. R. Priya and H. J. Byrne, “Investigation of Sodium Dodecyl Benzene Sulfonate Assisted Dispersion and Debundling of Single-Wall Carbon Nanotubes,” *J. Phys. Chem. C*, vol. 112, no. 2, pp. 332–337, Jan. 2008, doi: 10.1021/jp0743830.
[38] S. M. Goodman, “Sustainable Cellulose Composite Membranes for Multifunctional Sensing Applications,” Ph.D., University of Washington, United States -- Washington, 2021. Accessed: May 19, 2023. [Online]. Available: https://www.proquest.com/docview/2568279262/abstract/35804C90C6454850PQ/1
[39] “How Long Do Water Heaters Last? | A.O. Smith.” Accessed: Nov. 02, 2024. [Online]. Available: https://www.hotwater.com/info-center/how-long-do-water-heaters-last.html
[40] D. Shen *et al.*, “Moisture-Enabled Electricity Generation: From Physics and Materials to Self-Powered Applications,” *Adv. Mater.*, vol. 32, no. 52, p. 2003722, 2020, doi: 10.1002/adma.202003722.
[41] J. Bai, Y. Huang, H. Cheng, and L. Qu, “Moist-electric generation,” *Nanoscale*, vol. 11, no. 48, pp. 23083–23091, Dec. 2019, doi: 10.1039/C9NR06113D.
[42] G. Xue *et al.*, “Water-evaporation-induced electricity with nanostructured carbon materials,” *Nat. Nanotechnol.*, vol. 12, no. 4, Art. no. 4, Apr. 2017, doi: 10.1038/nnano.2016.300.
[43] T. G. Yun, J. Bae, A. Rothschild, and I.-D. Kim, “Transpiration Driven Electrokinetic Power Generator,” *ACS Nano*, vol. 13, no. 11, pp. 12703–12709, Nov. 2019, doi: 10.1021/acsnano.9b04375.
[44] Z. Zhang *et al.*, “Emerging hydrovoltaic technology,” *Nat. Nanotechnol.*, vol. 13, no. 12, Art. no. 12, Dec. 2018, doi: 10.1038/s41565-018-0228-6.
[45] Y. Huang, H. Cheng, and L. Qu, “Emerging Materials for Water-Enabled Electricity Generation,” *ACS Mater. Lett.*, vol. 3, no. 2, pp. 193–209, Feb. 2021, doi: 10.1021/acsmaterialslett.0c00474.

[46] J. Bae *et al.*, “Towards Watt-scale hydroelectric energy harvesting by Ti3C2Tx-based transpiration-driven electrokinetic power generators,” *Energy Environ. Sci.*, Oct. 2021, doi: 10.1039/D1EE00859E.
[47] J. Bae, T. G. Yun, B. L. Suh, J. Kim, and I.-D. Kim, “Self-operating transpiration-driven electrokinetic power generator with an artificial hydrological cycle,” *Energy Environ. Sci.*, vol. 13, no. 2, pp. 527–534, Feb. 2020, doi: 10.1039/C9EE02616A.
[48] W. Olthuis, B. Schippers, J. Eijkel, and A. van den Berg, “Energy from streaming current and potential,” *Sens. Actuators B Chem.*, vol. 111–112, pp. 385–389, Nov. 2005, doi: 10.1016/j.snb.2005.03.039.
[49] E. Donath and A. Voigt, “Streaming current and streaming potential on structured surfaces,” *J. Colloid Interface Sci.*, vol. 109, no. 1, pp. 122–139, Jan. 1986, doi: 10.1016/0021-9797(86)90288-2.
[50] F. H. J. van der Heyden, D. Stein, and C. Dekker, “Streaming Currents in a Single Nanofluidic Channel,” *Phys. Rev. Lett.*, vol. 95, no. 11, p. 116104, Sep. 2005, doi: 10.1103/PhysRevLett.95.116104.
[51] L. Joly, C. Ybert, E. Trizac, and L. Bocquet, “Hydrodynamics within the Electric Double Layer on Slipping Surfaces,” *Phys. Rev. Lett.*, vol. 93, no. 25, p. 257805, Dec. 2004, doi: 10.1103/PhysRevLett.93.257805.
[52] F. H. J. van der Heyden, D. Stein, K. Besteman, S. G. Lemay, and C. Dekker, “Charge Inversion at High Ionic Strength Studied by Streaming Currents,” *Phys. Rev. Lett.*, vol. 96, no. 22, p. 224502, Jun. 2006, doi: 10.1103/PhysRevLett.96.224502.
[53] J. Xu *et al.*, “Sustainable moisture energy,” *Nat. Rev. Mater.*, pp. 1–16, Feb. 2024, doi: 10.1038/s41578-023-00643-0.
[54] F. H. J. van der Heyden, D. J. Bonthuis, D. Stein, C. Meyer, and C. Dekker, “Electrokinetic Energy Conversion Efficiency in Nanofluidic Channels,” *Nano Lett.*, vol. 6, no. 10, pp. 2232–2237, Oct. 2006, doi: 10.1021/nl061524l.
[55] Y. Ren and D. Stein, “Slip-enhanced electrokinetic energy conversion in nanofluidic channels,” *Nanotechnology*, vol. 19, no. 19, p. 195707, Apr. 2008, doi: 10.1088/0957-4484/19/19/195707.
[56] J. A. Thomas and A. J. H. McGaughey, “Water Flow in Carbon Nanotubes: Transition to Subcontinuum Transport,” *Phys. Rev. Lett.*, vol. 102, no. 18, p. 184502, May 2009, doi: 10.1103/PhysRevLett.102.184502.
[57] N. Chen *et al.*, “MEG actualized by high-valent metal carrier transport,” *Nano Energy*, vol. 65, p. 104047, Nov. 2019, doi: 10.1016/j.nanoen.2019.104047.
[58] R. Zhu *et al.*, “Boosting moisture induced electricity generation from graphene oxide through engineering oxygen-based functional groups,” *Nano Energy*, vol. 94, p. 106942, Apr. 2022, doi: 10.1016/j.nanoen.2022.106942.
[59] H. Li *et al.*, “Utilizing sugarcane as green transpiration-driven generator for efficient electricity harvesting from seawater,” *Nano Energy*, vol. 99, p. 107378, Aug. 2022, doi: 10.1016/j.nanoen.2022.107378.
[60] K. W. Beard, Ed., *Linden’s Handbook of Batteries*, 5th Edition. McGraw-Hill Education, 2019. Accessed: Nov. 16, 2024. [Online]. Available: https://www.accessengineeringlibrary.com/content/book/9781260115925
[61] M. Iftikhar Khan, Z. Wang, X. Jia, and G. Cao, “Enhancing Aqueous Zinc-Ion Battery Performance through Structural Modification of Hydrated Vanadate with Lanthanum,” *ACS Appl. Energy Mater.*, vol. 7, no. 1, pp. 84–92, Jan. 2024, doi: 10.1021/acsaem.3c02140.

[62] X. Jia, C. Liu, Z. Wang, D. Huang, and G. Cao, “Weakly Polarized Organic Cation-Modified Hydrated Vanadium Oxides for High-Energy Efficiency Aqueous Zinc-Ion Batteries,” *Nano-Micro Lett.*, vol. 16, no. 1, p. 129, Feb. 2024, doi: 10.1007/s40820-024-01339-y.

[63] M. I. Khan, X. Jia, Z. Wang, and G. Cao, “Improving the Cycling Stability of Aqueous Zinc-Ion Batteries by Preintercalation of Polyaniline in Hydrated Vanadium Oxide,” *ACS Appl. Mater. Interfaces*, vol. 15, no. 21, pp. 25980–25989, May 2023, doi: 10.1021/acsami.3c03530.

[64] C. Liu *et al.*, “Expanded hydrated vanadate for high-performance aqueous zinc-ion batteries,” *Energy Environ. Sci.*, vol. 12, no. 7, pp. 2273–2285, Jul. 2019, doi: 10.1039/C9EE00956F.

[65] Z. Liu, X. Jia, and G. Cao, “Impacts of fluorine in NASICON-type materials as cathodes for aqueous zinc ion batteries,” *Energy Sci. Eng.*, vol. 9, no. 7, pp. 938–949, 2021, doi: 10.1002/ese3.925.

[66] S. Li, X. Jia, J. Liu, Z. Liu, and G. Cao, “Engineering hydrated vanadium oxide by K+ and Ni2+ incorporation for aqueous zinc ion batteries,” *Mater. Chem. Phys.*, vol. 287, p. 126358, Aug. 2022, doi: 10.1016/j.matchemphys.2022.126358.

[67] M. Tian *et al.*, “Structural engineering of hydrated vanadium oxide cathode by K+ incorporation for high-capacity and long-cycling aqueous zinc ion batteries,” *Energy Storage Mater.*, vol. 29, pp. 9–16, Aug. 2020, doi: 10.1016/j.ensm.2020.03.024.

[68] J. Zheng *et al.*, “Fast and reversible zinc ion intercalation in Al-ion modified hydrated vanadate,” *Nano Energy*, vol. 70, p. 104519, Apr. 2020, doi: 10.1016/j.nanoen.2020.104519.

[69] X. Jia, “Vanadyl Ethylene Glycolate for Aqueous Zinc-Ion Batteries with High Rate Capability and Ultralong Cycling Stability,” May 2019, Accessed: Nov. 16, 2024. [Online]. Available: http://hdl.handle.net/1773/43713

[70] X. Jia, C. Liu, Z. G. Neale, J. Yang, and G. Cao, “Active Materials for Aqueous Zinc Ion Batteries: Synthesis, Crystal Structure, Morphology, and Electrochemistry,” *Chem. Rev.*, vol. 120, no. 15, pp. 7795–7866, Aug. 2020, doi: 10.1021/acs.chemrev.9b00628.

[71] G. Nazir *et al.*, “A Review of Rechargeable Zinc–Air Batteries: Recent Progress and Future Perspectives,” *Nano-Micro Lett.*, vol. 16, no. 1, p. 138, Feb. 2024, doi: 10.1007/s40820-024-01328-1.

[72] Z. Li *et al.*, “Highly Nitrogen-Doped Carbon Nanotube Nanoarrays as Self-supported Bifunctional Electrocatalysts for Rechargeable and Flexible Zinc-Air Batteries,” *ACS Sustain. Chem. Eng.*, vol. 9, no. 12, pp. 4498–4508, Mar. 2021, doi: 10.1021/acssuschemeng.0c08727.

[73] G. Fang, J. Zhou, A. Pan, and S. Liang, “Recent Advances in Aqueous Zinc-Ion Batteries,” *ACS Energy Lett.*, vol. 3, no. 10, pp. 2480–2501, Oct. 2018, doi: 10.1021/acsenergylett.8b01426.

[74] Y. Huang *et al.*, “Novel Insights into Energy Storage Mechanism of Aqueous Rechargeable Zn/MnO2 Batteries with Participation of Mn2+,” *Nano-Micro Lett.*, vol. 11, p. 49, Jun. 2019, doi: 10.1007/s40820-019-0278-9.

[75] S. Huang, J. Zhu, J. Tian, and Z. Niu, “Recent Progress in the Electrolytes of Aqueous Zinc-Ion Batteries,” *Chem. – Eur. J.*, vol. 25, no. 64, pp. 14480–14494, Nov. 2019, doi: 10.1002/chem.201902660.

[76] N. Zhang *et al.*, “Cation-Deficient Spinel ZnMn2O4 Cathode in Zn(CF3SO3)2 Electrolyte for Rechargeable Aqueous Zn-Ion Battery,” *J. Am. Chem. Soc.*, vol. 138, no. 39, pp. 12894–12901, Oct. 2016, doi: 10.1021/jacs.6b05958.

[77] C. Guan *et al.*, “Decorating Co/CoNx nanoparticles in nitrogen-doped carbon nanoarrays for flexible and rechargeable zinc-air batteries,” *Energy Storage Mater.*, vol. 16, pp. 243–250, Jan. 2019, doi: 10.1016/j.ensm.2018.06.001.
[78] N. Hales, T. J. Schmidt, and E. Fabbri, “Reversible and irreversible transformations of Ni-based electrocatalysts during the oxygen evolution reaction,” *Curr. Opin. Electrochem.*, vol. 38, p. 101231, Apr. 2023, doi: 10.1016/j.coelec.2023.101231.
[79] J. E. Kim *et al.*, “Subnanometer Cobalt-Hydroxide-Anchored N-Doped Carbon Nanotube Forest for Bifunctional Oxygen Catalyst,” *ACS Appl. Mater. Interfaces*, vol. 8, no. 3, pp. 1571–1577, Jan. 2016, doi: 10.1021/acsami.5b10297.
[80] W. Niu, S. Pakhira, K. Marcus, Z. Li, J. L. Mendoza-Cortes, and Y. Yang, “Apically Dominant Mechanism for Improving Catalytic Activities of N-Doped Carbon Nanotube Arrays in Rechargeable Zinc–Air Battery,” *Adv. Energy Mater.*, vol. 8, no. 20, p. 1800480, 2018, doi: 10.1002/aenm.201800480.
[81] Y. Li and H. Dai, “Recent advances in zinc–air batteries,” *Chem. Soc. Rev.*, vol. 43, no. 15, pp. 5257–5275, Jul. 2014, doi: 10.1039/C4CS00015C.
[82] V. Caramia and B. Bozzini, “Materials science aspects of zinc–air batteries: a review,” *Mater. Renew. Sustain. Energy*, vol. 3, no. 2, p. 28, Apr. 2014, doi: 10.1007/s40243-014-0028-3.
[83] J. Fu, Z. P. Cano, M. G. Park, A. Yu, M. Fowler, and Z. Chen, “Electrically Rechargeable Zinc–Air Batteries: Progress, Challenges, and Perspectives,” *Adv. Mater.*, vol. 29, no. 7, p. 1604685, 2017, doi: 10.1002/adma.201604685.
[84] “ESP8266EX Datasheet.” Espressif Systems, 2023.
[85] Y. Chen *et al.*, “Enabling Acidic Oxygen Reduction Reaction in a Zinc-Air Battery with Bipolar Membrane,” *ACS Appl. Mater. Interfaces*, vol. 14, no. 10, pp. 12257–12263, Mar. 2022, doi: 10.1021/acsami.1c24328.
[86] J. Fang *et al.*, “A metal and nitrogen doped carbon composite with both oxygen reduction and evolution active sites for rechargeable zinc–air batteries,” *J. Mater. Chem. A*, vol. 8, no. 31, pp. 15752–15759, Aug. 2020, doi: 10.1039/D0TA02544E.
[87] *Thickness of Paper and Paperboard (Soft Platten Method)*, Standard T 551 om-98, 1998.
[88] *Tensile properties of paper and paperboard (using constant rate of elongation apparatus*, T 494 om-01.
[89] F. M. Smits, “Measurement of sheet resistivities with the four-point probe,” *Bell Syst. Tech. J.*, vol. 37, no. 3, pp. 711–718, May 1958, doi: 10.1002/j.1538-7305.1958.tb03883.x.
[90] *Forming handsheets for physical tests of pulp*, Procedure T 205 sp-02, Jul. 11, 2006.
[91] V. S. Chauhan and N. K. Bhardwaj, “Cationic Starch Preflocculated Filler for Improvement in Filler Bondability and Composite Tensile Index of Paper,” *Ind. Eng. Chem. Res.*, vol. 53, no. 29, pp. 11622–11628, Jul. 2014, doi: 10.1021/ie502008d.
[92] Y. Sang, M. McQuaid, and P. Englezos, “PRE-FLOCCULATION OF PRECIPITATED CALCIUM CARBONATE FILLER BY CATIONIC STARCH FOR HIGHLY FILLED MECHANICAL GRADE PAPER.,” *BioResources*, vol. 7, no. 1, pp. 354–373, Feb. 2012.
[93] V. S. Chauhan and N. K. Bhardwaj, “Efficacy of carbohydrate polymers in filler prefloccculation for use in papermaking,” *Arab. J. Chem.*, vol. 12, no. 8, pp. 3087–3095, Dec. 2019, doi: 10.1016/j.arabjc.2015.08.002.
[94] *Laboratory beating of pulp (PFI mill method)*, Standard T 248 sp-21.
[95] *Freeness of pulp (Canadian standard method)*, Standard T 227 om-17, Oct. 05, 2021.
[96] “OP1500.” Duracell.

[97] K. Li, F. Zheng, J. Zhu, and Q.-C. Zeng, “El Niño and the AMO Sparked the Astonishingly Large Margin of Warming in the Global Mean Surface Temperature in 2023,” *Adv. Atmospheric Sci.*, pp. s00376-023-3371–4, Jan. 2024, doi: 10.1007/s00376-023-3371-4.
[98] J. Houghton, “Global warming,” *Rep. Prog. Phys.*, vol. 68, no. 6, pp. 1343–1403, May 2005, doi: 10.1088/0034-4885/68/6/R02.
[99] S.-L. Yao, J.-J. Luo, G. Huang, and P. Wang, “Distinct global warming rates tied to multiple ocean surface temperature changes,” *Nat. Clim. Change*, vol. 7, no. 7, pp. 486–491, Jul. 2017, doi: 10.1038/nclimate3304.
[100] K. Zhang, B. C. Douglas, and S. P. Leatherman, “Global Warming and Coastal Erosion,” *Clim. Change*, vol. 64, no. 1, p. 41, May 2004, doi: 10.1023/B:CLIM.0000024690.32682.48.
[101] Y. Song, Z. Shi, G.-H. Hu, C. Xiong, A. Isogai, and Q. Yang, “Recent advances in cellulose-based piezoelectric and triboelectric nanogenerators for energy harvesting: a review,” *J. Mater. Chem. A*, vol. 9, no. 4, pp. 1910–1937, Feb. 2021, doi: 10.1039/D0TA08642H.
[102] J. Luo and Z. L. Wang, “Recent advances in triboelectric nanogenerator based self-charging power systems,” *Energy Storage Mater.*, vol. 23, pp. 617–628, Dec. 2019, doi: 10.1016/j.ensm.2019.03.009.
[103] D. Liu, L. Zhou, Z. L. Wang, and J. Wang, “Triboelectric nanogenerator: from alternating current to direct current,” *iScience*, vol. 24, no. 1, p. 102018, Jan. 2021, doi: 10.1016/j.isci.2020.102018.
[104] S. R. Anton and H. A. Sodano, “A review of power harvesting using piezoelectric materials (2003–2006),” *Smart Mater. Struct.*, vol. 16, no. 3, pp. R1–R21, May 2007, doi: 10.1088/0964-1726/16/3/R01.
[105] H. Askari *et al.*, “Intelligent systems using triboelectric, piezoelectric, and pyroelectric nanogenerators,” *Mater. Today*, vol. 52, pp. 188–206, Jan. 2022, doi: 10.1016/j.mattod.2021.11.027.
[106] A. Nozariasbmarz *et al.*, “Review of wearable thermoelectric energy harvesting: From body temperature to electronic systems,” *Appl. Energy*, vol. 258, p. 114069, Jan. 2020, doi: 10.1016/j.apenergy.2019.114069.
[107] V. Leonov, “Thermoelectric Energy Harvesting of Human Body Heat for Wearable Sensors,” *IEEE Sens. J.*, vol. 13, no. 6, pp. 2284–2291, Jun. 2013, doi: 10.1109/JSEN.2013.2252526.
[108] D. Enescu, *Thermoelectric Energy Harvesting: Basic Principles and Applications*. IntechOpen, 2019. doi: 10.5772/intechopen.83495.
[109] B. Parida, S. Iniyan, and R. Goic, “A review of solar photovoltaic technologies,” *Renew. Sustain. Energy Rev.*, vol. 15, no. 3, pp. 1625–1636, Apr. 2011, doi: 10.1016/j.rser.2010.11.032.
[110] M. A. Green, “Photovoltaic principles,” *Phys. E Low-Dimens. Syst. Nanostructures*, vol. 14, no. 1, pp. 11–17, Apr. 2002, doi: 10.1016/S1386-9477(02)00354-5.
[111] K. Zhang, L. Cai, A. Nilghaz, G. Chen, X. Wan, and J. Tian, “Enhancing output performance of surface-modified wood sponge-carbon black ink hygroelectric generator via moisture-triggered galvanic cell,” *Nano Energy*, vol. 98, p. 107288, Jul. 2022, doi: 10.1016/j.nanoen.2022.107288.
[112] J. Chen *et al.*, “Knittable Composite Fiber Allows Constant and Tremendous Self-Powering Based on the Transpiration-Driven Electrokinetic Effect,” *Adv. Funct. Mater.*, vol. n/a, no. n/a, p. 2203666, doi: 10.1002/adfm.202203666.

[113] M. Kaur, S. Ishii, R. Nozaki, and T. Nagao, “Hydropower generation by transpiration from microporous alumina,” *Sci. Rep.*, vol. 11, no. 1, Art. no. 1, May 2021, doi: 10.1038/s41598-021-90374-5.
[114] H. Peng, D. Wang, and S. Fu, “Artificial transpiration with asymmetric photothermal textile for continuous solar-driven evaporation, spatial salt harvesting and electrokinetic power generation,” *Chem. Eng. J.*, vol. 426, p. 131818, Dec. 2021, doi: 10.1016/j.cej.2021.131818.
[115] Y. Lv *et al.*, “A flexible electrokinetic power generator derived from paper and ink for wearable electronics,” *Appl. Energy*, vol. 279, p. 115764, Dec. 2020, doi: 10.1016/j.apenergy.2020.115764.
[116] T. G. Yun *et al.*, “Ion-permselective conducting polymer-based electrokinetic generators with maximized utility of green water,” *Nano Energy*, vol. 94, p. 106946, Apr. 2022, doi: 10.1016/j.nanoen.2022.106946.
[117] P. Král and M. Shapiro, “Nanotube Electron Drag in Flowing Liquids,” *Phys. Rev. Lett.*, vol. 86, no. 1, pp. 131–134, Jan. 2001, doi: 10.1103/PhysRevLett.86.131.
[118] X. Gao *et al.*, “Electric power generation using paper materials,” *J. Mater. Chem. A*, vol. 7, no. 36, pp. 20574–20578, Sep. 2019, doi: 10.1039/C9TA08264F.
[119] Y. Li *et al.*, “Spontaneous and sustainable multifunctional transpiration generator for simultaneous harvesting of electricity, freshwater and salt,” *Appl. Energy*, vol. 341, p. 121110, Jul. 2023, doi: 10.1016/j.apenergy.2023.121110.
[120] M. J. Hertaeg, R. F. Tabor, J. D. Berry, and G. Garnier, “Radial Wicking of Biological Fluids in Paper,” *Langmuir*, vol. 36, no. 28, pp. 8209–8217, Jul. 2020, doi: 10.1021/acs.langmuir.0c01318.
[121] S. Patari and P. S. Mahapatra, “Liquid Wicking in a Paper Strip: An Experimental and Numerical Study,” *ACS Omega*, vol. 5, no. 36, pp. 22931–22939, Sep. 2020, doi: 10.1021/acsomega.0c02407.
[122] X. Guan *et al.*, “Smart Textiles with Janus Wetting and Wicking Properties Fabricated by Graphene Oxide Coatings,” *Adv. Mater. Interfaces*, vol. 8, no. 2, p. 2001427, 2021, doi: 10.1002/admi.202001427.
[123] H. Takana and H. Nishiyama, “Numerical simulation of nanosecond pulsed DBD in lean methane–air mixture for typical conditions in internal engines,” *Plasma Sources Sci. Technol.*, vol. 23, no. 3, p. 034001, May 2014, doi: 10.1088/0963-0252/23/3/034001.
[124] R. H. Tunuguntla, F. I. Allen, K. Kim, A. Belliveau, and A. Noy, “Ultrafast proton transport in sub-1-nm diameter carbon nanotube porins,” *Nat. Nanotechnol.*, vol. 11, no. 7, pp. 639–644, Jul. 2016, doi: 10.1038/nnano.2016.43.
[125] L. Li and A. Manthiram, “Long-Life, High-Voltage Acidic Zn–Air Batteries,” *Adv. Energy Mater.*, vol. 6, no. 5, p. 1502054, 2016, doi: 10.1002/aenm.201502054.
[126] W. Zhang, B. S. Yeo, T. Schmid, and R. Zenobi, “Single Molecule Tip-Enhanced Raman Spectroscopy with Silver Tips,” *J. Phys. Chem. C*, vol. 111, no. 4, pp. 1733–1738, Feb. 2007, doi: 10.1021/jp064740r.
[127] A. Manthiram, “An Outlook on Lithium Ion Battery Technology,” *ACS Cent. Sci.*, vol. 3, no. 10, pp. 1063–1069, Oct. 2017, doi: 10.1021/acscentsci.7b00288.
[128] J. Chen, “Recent Progress in Advanced Materials for Lithium Ion Batteries,” *Materials*, vol. 6, no. 1, Art. no. 1, Jan. 2013, doi: 10.3390/ma6010156.
[129] Y. Chen *et al.*, “A review of lithium-ion battery safety concerns: The issues, strategies, and testing standards,” *J. Energy Chem.*, vol. 59, pp. 83–99, Aug. 2021, doi: 10.1016/j.jechem.2020.10.017.

[130] B. Liu *et al.*, “Safety issues caused by internal short circuits in lithium-ion batteries,” *J. Mater. Chem. A*, vol. 6, no. 43, pp. 21475–21484, Nov. 2018, doi: 10.1039/C8TA08997C.
[131] J. Ming, J. Guo, C. Xia, W. Wang, and H. N. Alshareef, “Zinc-ion batteries: Materials, mechanisms, and applications,” *Mater. Sci. Eng. R Rep.*, vol. 135, pp. 58–84, Jan. 2019, doi: 10.1016/j.mser.2018.10.002.
[132] R. Rajagopalan, Y. Tang, X. Ji, C. Jia, and H. Wang, “Advancements and Challenges in Potassium Ion Batteries: A Comprehensive Review,” *Adv. Funct. Mater.*, vol. 30, no. 12, p. 1909486, 2020, doi: 10.1002/adfm.201909486.
[133] N. Yabuuchi, K. Kubota, M. Dahbi, and S. Komaba, “Research Development on Sodium-Ion Batteries,” *Chem. Rev.*, vol. 114, no. 23, pp. 11636–11682, Dec. 2014, doi: 10.1021/cr500192f.
[134] A. Wang *et al.*, “Integrated design of aqueous zinc-ion batteries based on dendrite-free zinc microspheres/carbon nanotubes/nanocellulose composite film anode,” *J. Colloid Interface Sci.*, vol. 594, pp. 389–397, Jul. 2021, doi: 10.1016/j.jcis.2021.03.067.
[135] X. Gao, W. Yin, and X. Liu, “Carbon nanotubes-based electrode for Zn ion batteries,” *Mater. Res. Bull.*, vol. 138, p. 111246, Jun. 2021, doi: 10.1016/j.materresbull.2021.111246.
[136] H. Li *et al.*, “An extremely safe and wearable solid-state zinc ion battery based on a hierarchical structured polymer electrolyte,” *Energy Environ. Sci.*, Feb. 2018, doi: 10.1039/C7EE03232C.
[137] V. Mathew *et al.*, “Manganese and Vanadium Oxide Cathodes for Aqueous Rechargeable Zinc-Ion Batteries: A Focused View on Performance, Mechanism, and Developments,” *ACS Energy Lett.*, vol. 5, no. 7, pp. 2376–2400, Jul. 2020, doi: 10.1021/acsenergylett.0c00740.
[138] B. E. Conway, W. G. Pell, and T.-C. Liu, “Diagnostic analyses for mechanisms of self-discharge of electrochemical capacitors and batteries,” *J. Power Sources*, vol. 65, no. 1, pp. 53–59, Mar. 1997, doi: 10.1016/S0378-7753(97)02468-3.
[139] R. Holze, “Self-discharge of Batteries: Causes, Mechanisms and Remedies | Advanced Materials Science and Technology,” *Adv. Mater. Sci. Technol.*, vol. 4, no. 2, 2022, doi: https://doi.org/10.37155/2717-526X-0402-3.
[140] V. Knap, D.-I. Stroe, M. Swierczynski, R. Teodorescu, and E. Schaltz, “Investigation of the Self-Discharge Behavior of Lithium-Sulfur Batteries,” *J. Electrochem. Soc.*, vol. 163, no. 6, p. A911, Mar. 2016, doi: 10.1149/2.0641606jes.
[141] Z. Cao, P. Zhuang, X. Zhang, M. Ye, J. Shen, and P. M. Ajayan, “Strategies for Dendrite-Free Anode in Aqueous Rechargeable Zinc Ion Batteries,” *Adv. Energy Mater.*, vol. 10, no. 30, p. 2001599, 2020, doi: 10.1002/aenm.202001599.
[142] A. Dhiman and D. G. Ivey, “Electrodeposited Manganese Oxide on Carbon Paper for Zinc-Ion Battery Cathodes,” *Batter. Supercaps*, vol. 3, no. 3, pp. 293–305, Mar. 2020, doi: 10.1002/batt.201900150.
[143] C. Li, X. Xie, S. Liang, and J. Zhou, “Issues and Future Perspective on Zinc Metal Anode for Rechargeable Aqueous Zinc-ion Batteries,” *ENERGY Environ. Mater.*, vol. 3, no. 2, pp. 146–159, 2020, doi: 10.1002/eem2.12067.
[144] F. Wang *et al.*, “Highly reversible zinc metal anode for aqueous batteries,” *Nat. Mater.*, vol. 17, no. 6, Art. no. 6, Jun. 2018, doi: 10.1038/s41563-018-0063-z.
[145] C. Zhang *et al.*, “A ZnCl2 water-in-salt electrolyte for a reversible Zn metal anode,” *Chem. Commun.*, vol. 54, no. 100, pp. 14097–14099, Dec. 2018, doi: 10.1039/C8CC07730D.

[146] C. Deng *et al.*, “A Sieve-Functional and Uniform-Porous Kaolin Layer toward Stable Zinc Metal Anode,” *Adv. Funct. Mater.*, vol. 30, no. 21, p. 2000599, 2020, doi: 10.1002/adfm.202000599.
[147] A. Mitha, A. Z. Yazdi, M. Ahmed, and P. Chen, “Surface Adsorption of Polyethylene Glycol to Suppress Dendrite Formation on Zinc Anodes in Rechargeable Aqueous Batteries,” *ChemElectroChem*, vol. 5, no. 17, pp. 2409–2418, 2018, doi: 10.1002/celc.201800572.
[148] Z. Zhao *et al.*, “Long-life and deeply rechargeable aqueous Zn anodes enabled by a multifunctional brightener-inspired interphase,” *Energy Environ. Sci.*, vol. 12, no. 6, pp. 1938–1949, Jun. 2019, doi: 10.1039/C9EE00596J.
[149] A. Xia, X. Pu, Y. Tao, H. Liu, and Y. Wang, “Graphene oxide spontaneous reduction and self-assembly on the zinc metal surface enabling a dendrite-free anode for long-life zinc rechargeable aqueous batteries,” *Appl. Surf. Sci.*, vol. 481, pp. 852–859, Jul. 2019, doi: 10.1016/j.apsusc.2019.03.197.
[150] Z. Zhou *et al.*, “Graphene oxide-modified zinc anode for rechargeable aqueous batteries,” *Chem. Eng. Sci.*, vol. 194, pp. 142–147, Feb. 2019, doi: 10.1016/j.ces.2018.06.048.
[151] Z. Kang *et al.*, “3D Porous Copper Skeleton Supported Zinc Anode toward High Capacity and Long Cycle Life Zinc Ion Batteries,” *ACS Sustain. Chem. Eng.*, vol. 7, no. 3, pp. 3364–3371, Feb. 2019, doi: 10.1021/acssuschemeng.8b05568.
[152] Z. Pan *et al.*, “Stitching of Zn3(OH)2V2O7·2H2O 2D Nanosheets by 1D Carbon Nanotubes Boosts Ultrahigh Rate for Wearable Quasi-Solid-State Zinc-Ion Batteries,” *ACS Nano*, vol. 14, no. 1, pp. 842–853, Jan. 2020, doi: 10.1021/acsnano.9b07956.
[153] J. Wang, Z. Shen, and M. Yi, “Liquid-exfoliated graphene as highly efficient conductive additives for cathodes in lithium ion batteries,” *Carbon*, vol. 153, pp. 156–163, Nov. 2019, doi: 10.1016/j.carbon.2019.07.008.
[154] G. A. Smook, *Handbook for pulp and paper technologist*, 3rd ed. Questex, LLC, 2009.
[155] M. Laufmann and U. Gisella, “Fillers: Surface filling of wood-free paper with natural ground calcium carbonate,” *Appita Technol. Innov. Manuf. Environ.*, vol. 64, no. 5, Aug. 2020, doi: 10.3316/informit.472918738928260.
[156] C. Biermann, *Handbook of Pulping and Papermaking*, 2nd ed. Academic Press, 1996.
[157] H. Holik, *Handbook of Paper and Board*. Newark, GERMANY: John Wiley & Sons, Incorporated, 2013. Accessed: Nov. 11, 2024. [Online]. Available: http://ebookcentral.proquest.com/lib/washington/detail.action?docID=1161328
[158] E. Heister *et al.*, “Higher Dispersion Efficacy of Functionalized Carbon Nanotubes in Chemical and Biological Environments,” *ACS Nano*, vol. 4, no. 5, pp. 2615–2626, May 2010, doi: 10.1021/nn100069k.
[159] N. Sezer and M. Koç, “Oxidative acid treatment of carbon nanotubes,” *Surf. Interfaces*, vol. 14, pp. 1–8, Mar. 2019, doi: 10.1016/j.surfin.2018.11.001.
[160] Z. Xu, X. Yang, and Z. Yang, “A Molecular Simulation Probing of Structure and Interaction for Supramolecular Sodium Dodecyl Sulfate/Single-Wall Carbon Nanotube Assemblies,” *Nano Lett.*, vol. 10, no. 3, pp. 985–991, Mar. 2010, doi: 10.1021/nl9041005.
[161] R. Kukobat *et al.*, “Sol–gel chemistry mediated Zn/Al-based complex dispersant for SWCNT in water without foam formation,” *Carbon*, vol. 94, pp. 518–523, Nov. 2015, doi: 10.1016/j.carbon.2015.07.025.
[162] T. Matsuda *et al.*, “Aqueous Nanosilica Dispersants for Carbon Nanotube,” *Langmuir*, vol. 31, no. 10, pp. 3194–3202, Mar. 2015, doi: 10.1021/la504599b.

[163] H. Kataura *et al.*, “Optical properties of single-wall carbon nanotubes,” *Synth. Met.*, vol. 103, no. 1, pp. 2555–2558, Jun. 1999, doi: 10.1016/S0379-6779(98)00278-1.
[164] J.-S. Lauret *et al.*, “Ultrafast Carrier Dynamics in Single-Wall Carbon Nanotubes,” *Phys. Rev. Lett.*, vol. 90, no. 5, p. 057404, Feb. 2003, doi: 10.1103/PhysRevLett.90.057404.
[165] C. Gao *et al.*, “Surface modification methods and mechanisms in carbon nanotubes dispersion,” *Carbon*, vol. 212, p. 118133, Aug. 2023, doi: 10.1016/j.carbon.2023.118133.
[166] R. W. G. Wyckoff, “Crystal structures.” 1971 1963.
[167] L. Xiao, D. Mei, M. Cao, D. Qu, and B. Deng, “Effects of structural patterns and degree of crystallinity on the performance of nanostructured ZnO as anode material for lithium-ion batteries,” *J. Alloys Compd.*, vol. 627, pp. 455–462, Apr. 2015, doi: 10.1016/j.jallcom.2014.11.195.
[168] X.-Y. Wang, Y. Wang, N.-D. Zhao, M. Zheng, Y.-R. Guo, and Q.-J. Pan, “Van der Waals enhanced interfacial interaction in cellulose/zinc oxide nanocomposite coupled by graphitic carbon nitride,” *Carbohydr. Polym.*, vol. 268, p. 118235, Sep. 2021, doi: 10.1016/j.carbpol.2021.118235.
[169] A. Charbaji, W. Smith, C. Anagnostopoulos, and M. Faghri, “Zinculose: A new fibrous material with embedded zinc particles,” *Eng. Sci. Technol. Int. J.*, vol. 24, no. 2, pp. 571–578, Apr. 2021, doi: 10.1016/j.jestch.2020.09.005.
[170] A. Nanakoudis, “SEM: Types of Electrons and the Information They Provide,” Advancing Materials. Accessed: Nov. 20, 2024. [Online]. Available: https://www.thermofisher.com/blog/materials/sem-signal-types-electrons-and-the-information-they-provide/
[171] A. J. Bard and L. R. Faulkner, *Electrochemical methods: fundamentals and applications*. New York, NY: Wiley, 1980.
[172] L. A. Richards, “CAPILLARY CONDUCTION OF LIQUIDS THROUGH POROUS MEDIUMS,” *Physics*, vol. 1, no. 5, pp. 318–333, Nov. 1931, doi: 10.1063/1.1745010.
[173] S. H. Sengar, A. G. Mohod, Khandetod Y. P., S. P. Modak, and D. K. Gupta, “Design and development of wick type solar distillation system,” *J. Soil Sci. Environ. Manag.*, vol. 2, no. 7, pp. 125–133.
[174] H.-M. Yeh and L.-C. Chen, “The effects of climatic, design and operational parameters on the performance of wick-type solar distillers,” *Energy Convers. Manag.*, vol. 26, no. 2, pp. 175–180, Jan. 1986, doi: 10.1016/0196-8904(86)90052-X.
[175] W. H. Alawee *et al.*, “Improving the performance of pyramid solar distiller using dangled cords of various wick materials: Novel working mechanism of wick,” *Case Stud. Therm. Eng.*, vol. 28, p. 101550, Dec. 2021, doi: 10.1016/j.csite.2021.101550.
[176] F. A. Essa, W. H. Alawee, S. A. Mohammed, H. A. Dhahad, A. S. Abdullah, and Z. M. Omara, “Experimental investigation of convex tubular solar still performance using wick and nanocomposites,” *Case Stud. Therm. Eng.*, vol. 27, p. 101368, Oct. 2021, doi: 10.1016/j.csite.2021.101368.
[177] A. Ashari, T. M. Bucher, H. V. Tafreshi, M. A. Tahir, and M. S. A. Rahman, “Modeling fluid spread in thin fibrous sheets: Effects of fiber orientation,” *Int. J. Heat Mass Transf.*, vol. 53, no. 9, pp. 1750–1758, Apr. 2010, doi: 10.1016/j.ijheatmasstransfer.2010.01.015.
[178] M. J. Hertaeg, R. F. Tabor, J. D. Berry, and G. Garnier, “Dynamics of stain growth from sessile droplets on paper,” *J. Colloid Interface Sci.*, vol. 541, pp. 312–321, Apr. 2019, doi: 10.1016/j.jcis.2019.01.032.

[179] S. Jaganathan, H. V. Tafreshi, and B. Pourdeyhimi, “A realistic modeling of fluid infiltration in thin fibrous sheets,” *J. Appl. Phys.*, vol. 105, no. 11, p. 113522, Jun. 2009, doi: 10.1063/1.3141737.
[180] angel perez-cruz, ion stiharu, and aurelio dominguez-gonzalez, “Two-dimensional model of imbibition into paper-based networks using Richards’ equation - ProQuest,” *Microfluid. Nanofluidics*, vol. 21, no. 5, pp. 1–12, May 2017, doi: 10.1007/s10404-017-1937-0.
[181] M. M. Gong and D. Sinton, “Turning the Page: Advancing Paper-Based Microfluidics for Broad Diagnostic Application,” *Chem. Rev.*, vol. 117, no. 12, pp. 8447–8480, Jun. 2017, doi: 10.1021/acs.chemrev.7b00024.
[182] M. Parada, P. Vontobel, R. M. Rossi, D. Derome, and J. Carmeliet, “Dynamic Wicking Process in Textiles,” *Transp. Porous Media*, vol. 119, no. 3, pp. 611–632, Sep. 2017, doi: 10.1007/s11242-017-0901-5.
[183] C. K. Camplisson, K. M. Schilling, W. L. Pedrotti, H. A. Stone, and A. W. Martinez, “Two-ply channels for faster wicking in paper-based microfluidic devices,” *Lab. Chip*, vol. 15, no. 23, pp. 4461–4466, Nov. 2015, doi: 10.1039/C5LC01115A.
[184] R. Lucas, “Ueber das Zeitgesetz des kapillaren Aufstiegs von Flüssigkeiten,” *Kolloid-Z.*, vol. 23, no. 1, pp. 15–22, Jul. 1918, doi: 10.1007/BF01461107.
[185] M. Kostag, S. Köhler, T. Liebert, and T. Heinze, “Pure Cellulose Nanoparticles from Trimethylsilyl Cellulose,” *Macromol. Symp.*, vol. 294, no. 2, pp. 96–106, 2010, doi: 10.1002/masy.200900095.
[186] S. Zhang, J. Luo, M. Du, H. Hui, and Z. Sun, “Safety and cycling stability enhancement of cellulose paper-based lithium-ion battery separator by aramid nanofibers,” *Eur. Polym. J.*, vol. 171, p. 111222, May 2022, doi: 10.1016/j.eurpolymj.2022.111222.
[187] T. Nagy *et al.*, “Environmentally friendly high performance Zn-air rechargeable battery using cellulose derivatives: A 3D-printed prototype,” *J. Energy Storage*, vol. 49, p. 104173, May 2022, doi: 10.1016/j.est.2022.104173.
[188] Z. Wang, X. Meng, Z. Wu, and S. Mitra, “Development of flexible zinc–air battery with nanocomposite electrodes and a novel separator,” *J. Energy Chem.*, vol. 26, no. 1, pp. 129–138, Jan. 2017, doi: 10.1016/j.jechem.2016.08.007.
[189] Y. Wang, J. Long, J. Hu, Z. Sun, and L. Meng, “Polyvinyl alcohol /Lyocell dual-layer paper-based separator for primary zinc-air batteries,” *J. Power Sources*, vol. 453, p. 227853, Mar. 2020, doi: 10.1016/j.jpowsour.2020.227853.
[190] L. J. Yan, “INVESTIGATION OF CELLULOSE SEPARATOR IN ALUMINIUM-AIR BATTERY”.
[191] L.-L. Shen, G.-R. Zhang, M. Biesalski, and B. J. M. Etzold, “Paper-based microfluidic aluminum–air batteries: toward next-generation miniaturized power supply,” *Lab. Chip*, vol. 19, no. 20, pp. 3438–3447, 2019, doi: 10.1039/C9LC00574A.
[192] A. A. Selan, L. H. Saw, H. S. Thiam, D. Sun, and W. C. Tan, “Preliminary analysis of the cellulose-based battery separator,” *Mater. Today Proc.*, Feb. 2023, doi: 10.1016/j.matpr.2023.01.294.
[193] Z. Yang *et al.*, “A piece of common cellulose paper but with outstanding functions for advanced aqueous zinc-ion batteries,” *Mater. Today Energy*, vol. 28, p. 101076, Aug. 2022, doi: 10.1016/j.mtener.2022.101076.
[194] L. Li *et al.*, “PBC@cellulose-filter paper separator design with efficient ion transport properties toward stabilized zinc-ion battery,” *Electrochimica Acta*, vol. 430, p. 141129, Oct. 2022, doi: 10.1016/j.electacta.2022.141129.

[195] L. Li *et al.*, “Dilemma of Low-Cost Filter Paper as Separator: Toughen Its Wet Strength for Robust Aqueous Zinc-Ion Batteries,” *J. Phys. Chem. Lett.*, vol. 15, no. 2, pp. 380–390, Jan. 2024, doi: 10.1021/acs.jpclett.3c03113.
[196] B. Guo *et al.*, “Hierarchical N-Doped Porous Carbons for Zn–Air Batteries and Supercapacitors,” *Nano-Micro Lett.*, vol. 12, no. 1, p. 20, Jan. 2020, doi: 10.1007/s40820-019-0364-z.
[197] “Energizer Zinc Air Prismatic Handbook.” Energyizer Battery Manufacturing.
[198] “Energizer E91 Product Datasheet.” Energizer.
[199] R. A. Gill, “The behavior of on-site synthesized precipitated calcium carbonates and other calcium carbonate fillers on paper properties,” *Nord. Pulp Pap. Res. J.*, vol. 4, no. 2, pp. 120–127, May 1989, doi: 10.3183/npprj-1989-04-02-p120-127.
[200] N. Santos and J. Velho, “Coating structure with calcium carbonate pigments and its influence on paper and print gloss,” *Pulp Pap. Can. -Ont.-*, vol. 105, Sep. 2004.
[201] K. Mohamadzadeh-Saghavaz, H. Resalati, and A. Ghasemian, “Cellulose-precipitated calcium carbonate composites and their effect on paper properties,” *Chem. Pap.*, vol. 68, no. 6, pp. 774–781, Jun. 2014, doi: 10.2478/s11696-013-0513-7.
[202] B. B. Williams, J. L. Gidley, J. A. Guin, and R. S. Schechter, “Characterization of Liquid-Solid Reactions. Hydrochloric Acid-Calcium Carbonate Reaction,” *Ind. Eng. Chem. Fundam.*, vol. 9, no. 4, pp. 589–596, Nov. 1970, doi: 10.1021/i160036a011.
[203] S. Zakaria, B. H. Ong, S. H. Ahmad, M. Abdullah, and T. Yamauchi, “Preparation of lumen-loaded kenaf pulp with magnetite (Fe3O4),” *Mater. Chem. Phys.*, vol. 89, no. 2, pp. 216–220, Feb. 2005, doi: 10.1016/j.matchemphys.2003.12.026.
[204] S. Zakaria, B. H. Ong, and T. G. M. van de Ven, “Lumen loading magnetic paper II: mechanism and kinetics,” *Colloids Surf. Physicochem. Eng. Asp.*, vol. 251, no. 1, pp. 31–36, Dec. 2004, doi: 10.1016/j.colsurfa.2004.06.029.
[205] A. Marmur, “The radial capillary,” *J. Colloid Interface Sci.*, vol. 124, no. 1, pp. 301–308, Jul. 1988, doi: 10.1016/0021-9797(88)90351-7.
[206] E. W. Washburn, “The Dynamics of Capillary Flow,” *Phys. Rev.*, vol. 17, no. 3, pp. 273–283, Mar. 1921, doi: 10.1103/PhysRev.17.273.
[207] W. Shen, I. H. Parker, and Y. J. Sheng, “The effects of surface extractives and lignin on the surface energy of eucalypt kraft pulp fibres,” *J. Adhes. Sci. Technol.*, vol. 12, no. 2, pp. 161–174, Jan. 1998, doi: 10.1163/156856198X00038.
[208] K. T. Hodgson and J. C. Berg, “Dynamic Wettability Properties of Single Wood Pulp Fibers and Their Relationship to Absorbency,” *Wood Fiber Sci.*, pp. 3–17, 1988.
[209] K. Koljonen and P. Stenius, “Surface characterisation of single fibres from mechanical pulps by contact angle measurements,” *Nord. Pulp Pap. Res. J.*, vol. 20, no. 1, pp. 107–114, Jan. 2005, doi: 10.3183/npprj-2005-20-01-p107-114.
[210] “P2N2222A.” Semiconductor Components Industries, LLC, 2013.
[211] B. Razavi, *Design of Analog CMOS Integrated Circuits*, 2nd ed. New York, NY: McGraw-Hill Education, 2017.
[212] “IRF 9640 Power MOSFET.” Vishay Siliconix, Aug. 16, 2021.
[213] “1N4148 Fast Switching Diode.” Diodes Inc., Nov. 2023.